UNIVERSIDAD NACIONAL AUTÓNOMA DE MÉXICO

PROGRAMA DE MAESTRÍA Y DOCTORADO EN INGENIERÍA

CENTRO DE INVESTIGACIÓN EN ENERGÍA

DINÁMICA DE VÓRTICES GENERADOS POR FUERZAS ELECTROMAGNÉTICAS

(DYNAMICS OF ELECTROMAGNETICALLY DRIVEN VORTICES)

TESIS

QUE PARA OPTAR POR EL GRADO DE:

DOCTOR EN INGENIERÍA

ENERGÍA - PROCESOS Y USO EFICIENTE DE ENERGÍA

P R E S E N T A:

ALDO FIGUEROA LARA

TUTOR:

DR. SERGIO CUEVAS GARCÍA

2010

To my wife and family, without whose love and understanding this project would not have been possible.

Acknowledgements

Many persons have been involved directly or indirectly in the realization of this project. The top headed are Drs. Sergio Cuevas and Eduardo Ramos, both of them are terrific researchers, teachers and persons who invited me living in the fluid dynamics world. The half part of the project is based on experimental results for which the technical support of Guillermo Hernández during the experimental procedures is acknowledged. It is also thanked the facilities and the community support from CIE-UNAM. This work would have not been possible without the economic support from CONACYT. I thank a mobility grant from the SCAT project and the ALFA Programme of EuropeAid during the stay at IRPHE, where valuable meetings with Drs. Patrice Meunier and Emmanuel Villermaux made possible a deeper understanding about mixing. Suggestions, criticisms, typo corrections, and the like on the manuscript from the reviewers are really appreciated. Finally, I thank the old and new friends at CIE and IRPHE, thanks to you the phD journey became fun and pleasant.

Contents

Abstract v

Acknowledgements ix

Preface xi

1 Steady dipolar vortex flow 1
- 1.1 Introduction . . . 2
- 1.2 Experimental procedure and observations . . . 4
  - 1.2.1 Flow measurements in horizontal planes . . . 5
  - 1.2.2 Flow measurements in vertical planes . . . 9
- 1.3 Theoretical model . . . 11
  - 1.3.1 Quasi-two-dimensional numerical model . . . 12
- 1.4 Comparison of numerical model with experimental observations . 16
  - 1.4.1 The friction model . . . 16
  - 1.4.2 General features of the flow structure . . . 17
  - 1.4.3 Flow features as functions of the applied current . . . 18
- 1.5 Discussion . . . 20

2 Stokes layer in oscillatory dipolar vortex flow 23
- 2.1 Introduction . . . 24
- 2.2 Experimental procedure and observations . . . 26
- 2.3 Theoretical model . . . 28
  - 2.3.1 Unidimensional analytic solution . . . 29
  - 2.3.2 Three-dimensional numerical solution . . . 31
- 2.4 Results . . . 33
- 2.5 Discussion . . . 42

3 Dynamics of oscillatory vortex flows in multipolar magnetic fields 47
3.1 Introduction 48
3.2 Experimental procedure 49
3.3 Theoretical model 50
3.4 Results 52
3.4.1 Flow analysis 52
3.4.2 Three-dimensionality of the flows in terms of kinetic energy 64
3.5 Discussion 66

4 Mixing in oscillatory vortex flows in multipolar magnetic fields 69
4.1 Introduction 70
4.2 Experimental procedure 72
4.3 Theoretical model 73
4.3.1 Quasi-two-dimensional numerical model 73
4.3.2 Diffusive Strip Method (DSM) 74
4.4 Results 76
4.4.1 Lagrangian trajectories and spatial symmetry breaking . . 76
4.4.2 Convection-diffusion of a scalar: DSM results 81
4.5 Discussion 87

Concluding remarks 91

Bibliography 95

Abstract

In this thesis, an experimental an theoretical study of laminar vortical flows continuously driven by electromagnetic forcing in a shallow layer of an electrolyte, is presented. The driving Lorentz force is generated by the interaction of electric currents injected in the thin fluid layer and the magnetic field distribution produced by one or several dipolar permanent magnets. Velocity profiles are obtained through Particle Image Velocimetry. In addition, flow visualization and Lagrangian particle tracking are performed. First, the steady dipolar flow produced by the interaction of a uniform dc current and a single permanent magnet is studied. The flow is explored in planes parallel and perpendicular to the bottom wall. A quasi-two-dimensional (Q2D) numerical model that introduces the non-uniformity of the magnetic field is used to reproduce the experimental observations. Also, by injecting an alternate electric current, an oscillating dipolar vortex is explored. The attention is initially focused on the motion of the oscillatory layer that, incidentally, is analogous to the Stokes's oscillating plate problem but with a body (Lorentz) force driving the motion. Experimental results are compared with a simple analytical solution and a full three-dimensional (3D) numerical simulation. Further, the flow in horizontal planes is analyzed and a resonant behavior for the oscillating vortex flow is found. The study is then extended to oscillating vortex flows produced by an alternate current and different arrays of permanent magnets. In particular, three-dimensional characteristics of these flows are explored. By comparing experimental results with both Q2D and 3D numerical models, the Q2D assumption is corroborated under the explored conditions. The mixing properties of flows in multipolar magnetic fields are also analyzed. Numerical Lagrangian particle tracking is compared with experimental visualization. In ordered arrays of magnets, flow patterns exhibit symmetry lines that inhibit the mixing which is enhanced when symmetries are destroyed by the use of a disordered array of magnets or by injecting two electric currents in orthogonal directions. The convection-diffusion transport of a passive scalar is also addressed through the Diffusive Strip Method. A good qualitative agreement

between numerical and experimental observations is found. In addition, mixing efficiency is quantified by calculating the probability density function.

Preface

Fluid mixing is a very important subject for multiple applications in geophysics, chemestry and biology, as well as in many relevant industrial devices. Of particular interest are non-intrusive methods that rely on the use of electromagnetic forces (Lorentz forces) to produce stirring and eventually mixing in electrically conducting fluids. Electromagnetic forcing has been widely used experimentally to stir shallow layers of liquid metals or electrolytes. The idea is to generate a rotational Lorentz force by the injection of electric currents in a thin fluid layer exposed to a steady external magnetic field. In this way, it is possible to create vortical structures which, under certain conditions, may show a quasi-two-dimensional behavior (Q2D). Incidentally, these flow structures present similarities with those found in atmospheric and oceanic flows (Mc Williams 2006), such as tidal jets in bays and estuaries (Fujiwara *et al.* 1992), where nutrients (Wolansky *et al.* 1988) and particle transport (Brown *et al.* 2000) are of great importance.

Electromagnetic stirring in shallow layers of electrolyte is a versatile experimental method that allows the exploration of many vortical flows. Incidentally, by varying the number and size of permanent magnets and controlling the injected electric current (either dc or ac), different flow structures and regimes have been explored. For instance, steady (Figueroa et al. 2009) or time-dependent (Akkermans *et al.* 2008, Figueroa *et al.* 2010) vortex dipoles can be produced using a single magnet, while the use of severeal magnets of different sizes can lead to the the generation of fully controlable multi-scale vortical flows in laboratory (Rossi *et al.* 2006a; 2006b). In fact, electromagnetically driven shallow flows generated with an array of magnets have also been used to promote Q2D turbulent flows (Paret & Tabeling 1997; Tabeling 2002) and, particularly, to explore its decaying properties (Cardodo *et al.* 1994; Clercx *et al.* 2002). In turn, fundamental studies of mixing and chaotic advection have relied on a continu-

ous stirring process produced by steady or time-periodic electromagnetic forcing (Williams *et al.* 1997; Rothstein *et al.* 1999; Voth *et al.* 2002; Voth *et al.* 2003). A deep understanding of all these phenomena requires to complement the experimental studies with a theoretical modeling that can grasp the basic features of electromagnetically forced flows. In particular, given the non-uniform magnetic field distribution and the possibility of considering time-dependent currents, special care should be taken to model electromagnetic forces properly in these flows. Evidently, a numerical simulation that aims at modeling electromagnetically driven flows realistically must be calibrated against experimental results. Although some advances have been reported in the past years on the modeling of some particular flow configurations, there are still many important aspects to be explored. The main purpose of the present work is to contribute, through experimental studies and numerical simulations, to the understanding of the dynamics of laminar flows continuously driven by electromagnetic forces in shallow electrolytic layers. We explore different configurations of localized Lorentz forces that lead to steady and time-dependent flows. Of particular relevance are those flows generated by time-periodic forces that help to enhance the fluid mixing. The three-dimensionality of the shallow flows under the explored conditions is also addressed. In fact, the influence of some factors that may promote the departure of the flow from a quasi-two-dimensional (Q2D) behavior and the formation of three-dimensional (3D) flow patterns, such as the time-dependent nature of the forcing, its strength, and the inhomogeneities in the magnetic field, is evaluated. Taking advantage of the transparency of the electrolyte, Particle Image Velocimetry (PIV) measurements are used to explore basic flow structures such as a vortex dipole, as well as more complex vortical flows generated with different arrays of magnets, either with steady or time-dependent forces, in a thin (4 mm) fluid layer. The mixing properties of some flow configurations produced by time-periodic forces are also analyzed by flow visualization and Lagrangian particle tracking, as well as by solving the scalar transport by convection-diffusion. Numerical simulations based on a Q2D approximation and a full 3D approach are carried out and compared against the experimental results. Whenever possible, analytical solutions are also provided.

In Chapter 1, the steady dipolar flow produced by the interaction of a uniform dc current and a single permanent magnet, is studied. The flow is explored experimentally in planes parallel and perpendicular to the bottom wall. It is important to remark that velocity profiles in the layer thickness have not been reported in previous studies. These profiles clearly show the effect of the non-uniform Lorentz force due to the field decay. A Q2D numerical model that

introduces the non-uniformity of the magnetic field in the normal direction is used to reproduce the experimental observations.

In Chapter 2, an oscillatory dipolar vortex created by the injection of an alternate electric current and the field produced by a single magnet, is explored. The attention is focused on the motion of the oscillatory thin layer driven by the periodic Lorentz force. PIV measurements of velocity fields in different vertical planes of motion (normal to both the bottom wall and the injected current) in the neighborhood of the region exposed to the magnetic field, are analyzed. The flow in the layer is analogous to the Stokes's oscillating plate problem but with a body (Lorentz) force driving the motion. Experimental results for several forcing frequencies are compared with a simple analytical solution and a full 3D numerical simulation that considers the 3D distribution of the magnetic field.

Oscillating vortex flows produced by an alternate current and several (from one to five) permanent magnets, are explored in Chapter 3. Velocity fields in a horizontal plane (parallel to the bottom wall) are obtained through PIV within a range of forcing frequencies of 1 to 500 mHz. Identification and tracking of elliptical and hyperbolic critical points, that appear and disappear as a result of the flow dynamics, are used to characterize the system. Experimental results are compared with both Q2D and 3D numerical models. Also, kinetic energies associated to the velocity components in the horizontal and vertical planes of motion are numerically calculated and compared in order to assess the importance of 3D effects.

In Chapter 4, the mixing properties of flows in multipolar magnetic field distributions are analyzed. Through flow visualization and numerical Lagrangian tracking, symmetries in multipolar flows are identified when ordered configurations of permanent magnets are used. Symmetries in the flow patterns are associated to inhibition of fluid mixing. Spatial symmetry breaking is promoted by the use of a disordered array of magnets or by injecting two electric currents in orthogonal directions. The transport of a passive scalar by convection-diffusion is considered through the Diffusive Strip Method which is applied to flows in different multipolar magnetic field distributions. Qualitative comparison with experimental observations and quantification of mixing efficiency with the probability density function are carried out.

Finally, the main conclusions of the thesis are summarized.

Chapter 1

Steady dipolar vortex flow

In this Chapter[1], steady dipolar vortices continuously driven by electromagnetic forcing in a shallow layer of an electrolytic fluid are studied experimentally and theoretically. The driving Lorentz force is generated by the interaction of a D.C. uniform electric current injected in the thin layer and the non-uniform magnetic field produced by a small dipolar permanent magnet (0.3 T). Laminar velocity profiles in the neighbourhood of the zone affected by the magnetic field were obtained with Particle Image Velocimetry in planes parallel and normal to the bottom wall. Flow planes at different depths of the layer were explored for injected currents ranging from 10 to 100 mA. Measurements of the boundary layer attached to the bottom wall reveal that, due to the variation of the field in the normal direction, a slightly flattened developing profile with no shear stresses at the free surface is formed. A quasi-two-dimensional magnetohydrodynamic numerical model that introduces the non-uniformity of the magnetic field, particularly its decay in the normal direction, was developed. Vertical diffusion produced by the bottom friction was modeled through a linear friction term. The model reproduces the main characteristic behaviour of the electromagnetically forced flow.

[1]This Chapter is mainly based on the paper: Figueroa, A., Demiaux, F., Cuevas, S. & Ramos, E., 2009, "Electrically driven vortices in a weak dipolar magnetic field in a shallow electrolytic layer". *J. Fluid Mech.*, **641**, 245–261.

1.1 Introduction

Electromagnetic forcing is a common experimental method to produce stirring in shallow layers of electrically conducting fluids. The idea is to produce a rotational Lorentz force by the injection of electric currents in a thin fluid layer exposed to a steady external magnetic field. This method has been widely used with the purpose of exploring the behaviour of quasi-two-dimensional flows which, incidentally, present similarities with those found in oceanic and atmospheric flows.

Past investigations on electromagnetically driven flows in shallow layers can be divided in two groups. In the first group the flow is enforced by injecting a steady electric current through a liquid metal layer under a strong uniform magnetic field normal to the layer (Sommeria 1986; 1988a; 1988b; Messadek & Moreau 2002). Due to the high electrical conductivity of liquid metals and the strong magnetic field intensities, reached through electromagnets or superconducting magnets, the Hartmann number, that estimates the ratio of magnetic to viscous forces, can be very high. Under these conditions three-dimensional perturbations in the normal direction are suppressed by the action of the magnetic field (Sommeria 1986; Messadek & Moreau 2002). Sommeria & Moreau (1982) showed that flows between parallel insulating walls under a strong uniform magnetic field can be described in terms of a two-dimensional core flow with a linear friction (the Hartmann friction) that accounts for the effects of the boundary layers. This approach has been successfully applied to electromagnetically driven flows in shallow layers where the two-dimensional Navier-Stokes equation includes both a steady forcing and a linear Hartmann friction term (Sommeria 1986; 1988a) and even inertial effects in Hartmann layers can be considered (Potherát, Sommeria & Moreau 2000). The second group of electromagnetically driven shallow flows corresponds to those generated by the injection of electric currents in a thin layer of an electrolyte under a non-uniform magnetic field produced by an array of permanent magnets (Cardoso, Marteau & Tabeling 1994). The low electrical conductivity of electrolytes compared with that of liquid metals, and the small magnetic field intensities produced by permanent magnets result in low-Hartmann-number flows. The geometrical confinement imposed by the shallow layer restricts three-dimensional perturbations in the normal direction. The use of two thin stably stratified fluid layers enhances the tendency of the flows towards two-dimensionality since the density difference of the interface acts to prevent vertical velocities (Marteau, Cardoso & Tabeling 1995; Paret & Tabeling 1997). In shallow flows, the role of bottom friction is of fundamental

importance since it promotes a vertical diffusion, associated with the exponential damping of the flow. In purely hydrodynamic flows vertical diffusion is usually parametrized by adding a linear friction term (the Rayleigh friction) to the two-dimensional Navier-Stokes equation (Hansen, Marteau & Tabeling 1998; Clercx & van Heijst 2002; Clercx, van Heijst & Zoeteweij 2003). This approach can be applied for describing decaying vortex flows initially promoted by electromagnetic forces. Experimentally, relaxation regimes can be studied following the application of a short current impulse in the fluid layer (Cardoso *et al.* 1994; Marteau *et al.* 1995; Paret & Tabeling 1997; Paret *et al.* 1997; Hansen *et al.* 1998; Clercx *et al.* 2003). In this case, a purely hydrodynamic description is sufficient since once the electric current is turned off, magnetohydrodynamic (MHD) effects can be disregarded because induced electric currents are usually negligible. However, for continuously electromagnetically forced shallow flows, MHD interactions cannot be disregarded since Lorentz force is always present. The understanding and modelling of these flows is important since fundamental applications rely on a continuous stirring process. That is the case of mixing of a passive scalar with steady or periodic electromagnetic forcing (Williams, Marteau & Gollub 1997; Rothstein, Henry & Gollub 1999; Voth, Haller & Gollub 2002; Voth, Saint, Dobler & Gollub 2003), the promotion of quasi-two-dimensional turbulence (Paret & Tabeling 1997; Tabeling 2002) or the generation of fully controlable multi-scale flows in laboratory (Rossi, Vassilicos and Hardalupas 2006a; 2006b). However, to the best of our knowledge, a full magnetohydrodynamic description of these phenomena has not been provided. The objective of the present contribution is two fold. In the first place, the work is aimed at the experimental analysis of a dipolar vortex created in a thin layer of an electrolyte by the interaction of a steady, uniform electric current with the field produced by a single dipolar permanent magnet. This basic flow structure, usually present in a variety of scales in natural and laboratory flows, is also the building block of more complex flow patterns (*e.g.* Rossi *et al.* 2006a; 2006b). By controlling the intensity of the injected current in the shallow layer, we take advantage of the transparency of the electrolyte to explore the inner flow structure through PIV measurements in both planes parallel and normal to the bottom wall. Secondly, this paper also provides a simplified quasi-two-dimensional model that contains the main physical ingredients of continuously electromagnetically forced laminar flows in shallow layers under localized magnetic fields. By taking only the dominant (normal) component of the non-uniform magnetic field within the shallow layer, which incidentally is fairly well reproduced analytically from the experimental distribution, the governing equations of motion are averaged in the normal direction.

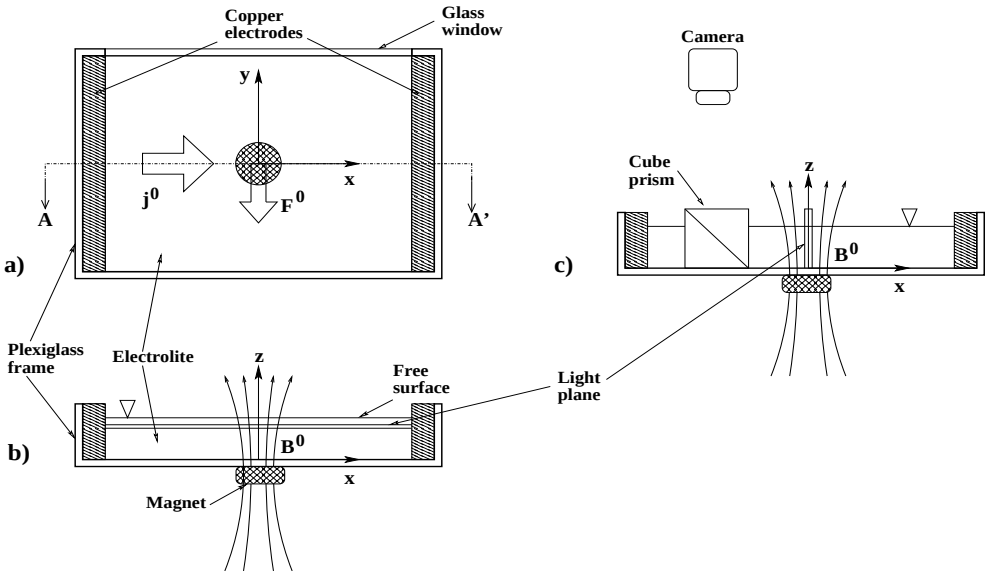

Figure 1.1: Sketch of the experimental device, not drawn to scale. a) Plan view. b) AA' plane, set up for recording velocities in the horizontal plane. c) AA' plane, experimental set up for recording velocities in the vertical plane. $\mathbf{j}^0$ is the imposed electrical current, $\mathbf{F}^0$ denotes the main direction of the Lorentz force. Within the layer, the magnetic field $\mathbf{B}^0$ points mainly in the positive z-direction.

Since this average considers the decay of the field in the vertical direction, the model allows to calculate the velocity field in planes at different depths in the layer. The comparison of the numerical and experimental velocity profiles shows a good quantitative agreement. The model appears to be particularly suited for the analysis of electromagnetically driven flows in shallow electrolytic layers.

1.2 Experimental procedure and observations

The experimental setup consists of a rectangular frame of 28 cm $\times$ 38 cm $\times$ 1.6 cm; one of the long sides and the two short sides are made of plexiglass. The fourth side is made of glass. The frame is water-tight glued to a thin floated glass plate 0.2 cm thick to form a cell with large horizontal area and small depth. Copper electrodes with rectangular cross section are placed along the shorter sides of the cell and connected to an adjustable d.c. voltage power supply. A

permanent cylindrical neodynium-iron-boron dipole magnet with a diameter of $d = 1.9$ cm and 0.5 cm height is placed under the glass plate with its upper flat face touching the lower side of the plate. The magnet is vertically magnetized with a maximum strength of 0.33 T at its surface. The cell is partially filled with a weak electrolytic solution of sodium bicarbonate ($NaHCO_3$) at 8.6% by weight. The height, width and depth of the electrolite layer are 0.4 cm, 36 cm and 28 cm respectively, with a total volume of 400 cm^3. The mass density, kinematic viscosity and electrical conductivity of the electrolyte are $\rho = 1.09 \times 10^3$ Kg/m^3, $\nu = 10^{-6}$ m^2/s, and $\sigma = 6.36$ S/m, respectively. The cell was mounted on a three point support and leveled to get a horizontal layer of water solution with uniform thickness. The direct current injected through the pair of electrodes interacts with the non-uniform magnetic field distribution generating a rotational Lorentz force that sets the fluid in motion. In the experiments electric currents varied within the range 10 to 100 mA. Due to the distance from the electrodes to the observation region and the small magnitude of electric currents, the electrochemical reactions occuring at the electrodes are negligible, as are the temperature changes due to Joule dissipation. Quantitative measurements of the velocity field were obtained with a Particle Image Velocimetry system (Dantec FlowMap PIV1100). We made two sets of flow measurements that required slightly different arrangements of the optical components of the system. In the first set, we observed the horizontal flow at different depths, while in the second, we observed the velocity field in a vertical plane perpendicular to the horizontal bottom wall (see figure 1.1).

1.2.1 Flow measurements in horizontal planes

In this observation, a laser sheet parallel to the bottom wall entered the cell through the vertical glass wall and illuminated an area of 4.6 $\times$ 28 cm. The x- and y-coordinates lay on the horizontal plane while z-coordinate points in the normal direction. The origin was placed in the bottom wall at the point of maximum magnetic field strength. Flow images were captured with a Kodak model Megaplus ES1.0/Type 16 (30Hz) camera, with a trigger sincronized with the illumination. The camera sits on a holder 20 cm above the fluid layer. The camera has a 1008 $\times$ 1016 pixels CCD and the actual area of the captured image is approximately 4.4 cm $\times$ 4.4 cm. The spatial deformation due to the proximity of the camera to the liquid layer was less than 1mm in the x- and y-directions and was compensated before making the analysis. Care was taken to ensure that the laser sheet and the bottom of the plate were parallel. To measure the thickness

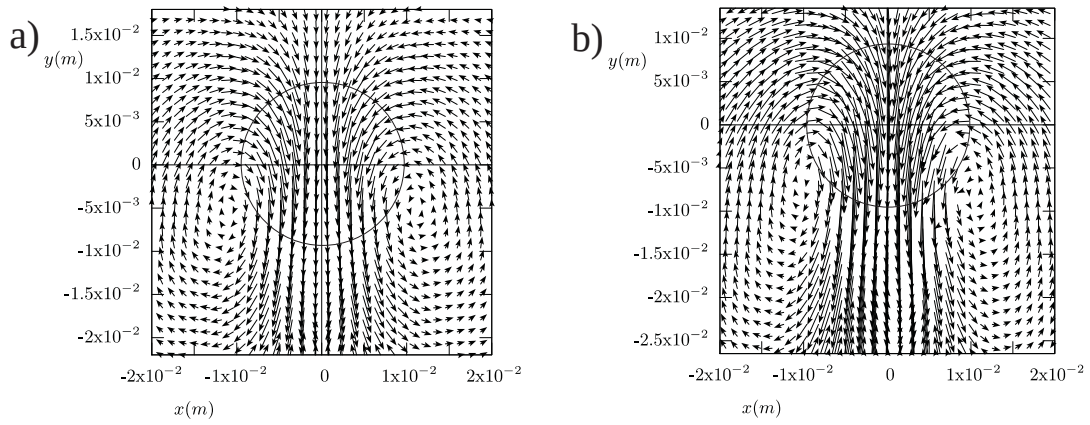

Figure 1.2: Velocity field for a) $I = 25$ mA, and b) I=50 mA. For the velocity scale, see figures 1.7 and 1.8). The circle corresponds to the position of the magnet. $z = 3.5$ mm, $B_{max} = 0.14$ T ($Ha = 0.20$).

of the illuminating light, the laser sheet light was intercepted at the position of interest by a cubic $45\,\mathrm{deg}$ prism which deflected the beam in the vertical direction. The light is then captured at zero degrees of incidence by a camera and the image digitalized. Correcting for beam dispersion, a thickness of 0.07 $\pm$ 0.01 cm was determined. In the analysis, we used interrrogation areas of 64 $\times$ 64 pixels with 50% overlap in x and y and an adaptive correlation. These conditions gave us a spatial resolution of 0.13 cm $\times$ 0.13 cm. Preliminary experiments were used to find that maximum velocities were approximately 0.6 cm/s and 1.5 cm/s for electric currents of 25 mA and 100 mA, respectively. The time interval between two subsequent images for the majority of experiments was 50 ms. For the lowest measured velocities (corresponding to 10 mA), the time between images was 100 ms. Measurements of the flow in horizontal planes at different depths were obtained by lowering the stand of the laser the required distance using fine pitch screws. The uncertainty in the vertical position of the recording plane was precisely the width of the laser sheet. Sample PIV measurements at selected points at different depths of the fluid layer were double-checked using Laser Doppler anemometry (LDA) whose resolution in the vertical direction is approximately 1 mm. The readings with the two techniques agree to within the error of the LDA. Based on the maximum velocity near the free surface ($z = 3.5$ mm) and the diameter of the magnet, the Reynolds numbers of the flow varied from 50, for injected currents of 10 mA, to 290 for 100 mA. In turn, the Hartmann number, $Ha = B_{max} h \sqrt{\sigma/\rho\nu}$, was based on the maximum

magnetic field strength, B_{max}, at a height h from the bottom wall. Hence, Ha varied from 0.32 at the bottom to 0.19 at the free surface.

Due to the experimental configuration, a quasi-two-dimensional flow structure was promoted where horizontal velocity components were much bigger than the vertical component (see § 1.2.2). Since the injected current and the dominant magnetic field component point in the positive x- and z-direction, respectively, the force points mainly in the negative y-direction. The flow develops a transient regime after which a well-defined steady flow pattern composed of two symmetric counterrotating lobes (a vortex dipole) is reached. For small electric currents ($I \approx 10$ mA) convective effects are negligible and the flow is mainly governed by diffusion so that the vortex dipole displays symmetric patterns with respect to both x and y axes. Due to the non-slip condition at the bottom wall, the highest velocities are located at the free surface of the electrolyte layer in a neighbourhood above the magnet along the y-axis. In this region, the motion is similar to a plane jet with a broad base, with fluid moving in the negative y-direction. The velocity field for a plane at a distance of $z = 3.5$ mm from the bottom and an electric current of $I = 25$ mA is shown in figure 1.2(a), where the circle indicates the position of the magnet. In the plane analysed, the magnitude of the maximum velocity is 5.8×10^{-3} m/s ($Re = 110$) and is located at $x = 0$, $y = -4.5 \times 10^{-3}$ m. Figure 1.2(b) shows the velocity field when the electric current is increased to 50 mA. Consequently, the maximum velocity is also increased reaching a magnitude of 9.8×10^{-3} m/s ($Re = 186$) at $x = 0$, $y = -7.6 \times 10^{-3}$ m, further downstream from the point of maximum velocity for $I = 25$ mA. The counter-rotating vortices are elongated in the direction of the force so that the centers of the recirculation structures (where the magnitude of the velocity is nearly zero) are displaced downstream. This is clearly a non-linear convective effect that breakes the symmetry of the vortex dipole with respect to the x-axis. The general features of the velocity field are more clearly observed in figures 1.3(a–d), where the velocity components u and v are plotted as functions of position for $I = 25$ mA at two different z-planes. Figures 1.3(a) and 1.3(b) correspond to $z = 3.5$ mm while 1.3(c) and 1.3(d) to $z = 1.5$ mm. Each figure contains both components, 1.3(a) and 1.3(c) as a function of x-coordinate at $y = 0$, and 1.3(b) and 1.3(d) as a function of y-coordinate at $x = 0$. Note that, in general, the u velocity component is approximately an order of magnitude smaller than the v-component. The velocity distribution in the direction perpendicular to the injected current (v component, figures 1.3(a) and 1.3(c)), is nearly symmetric in the x-coordinate. The velocity profiles at the two z-planes are alike, the most salient difference

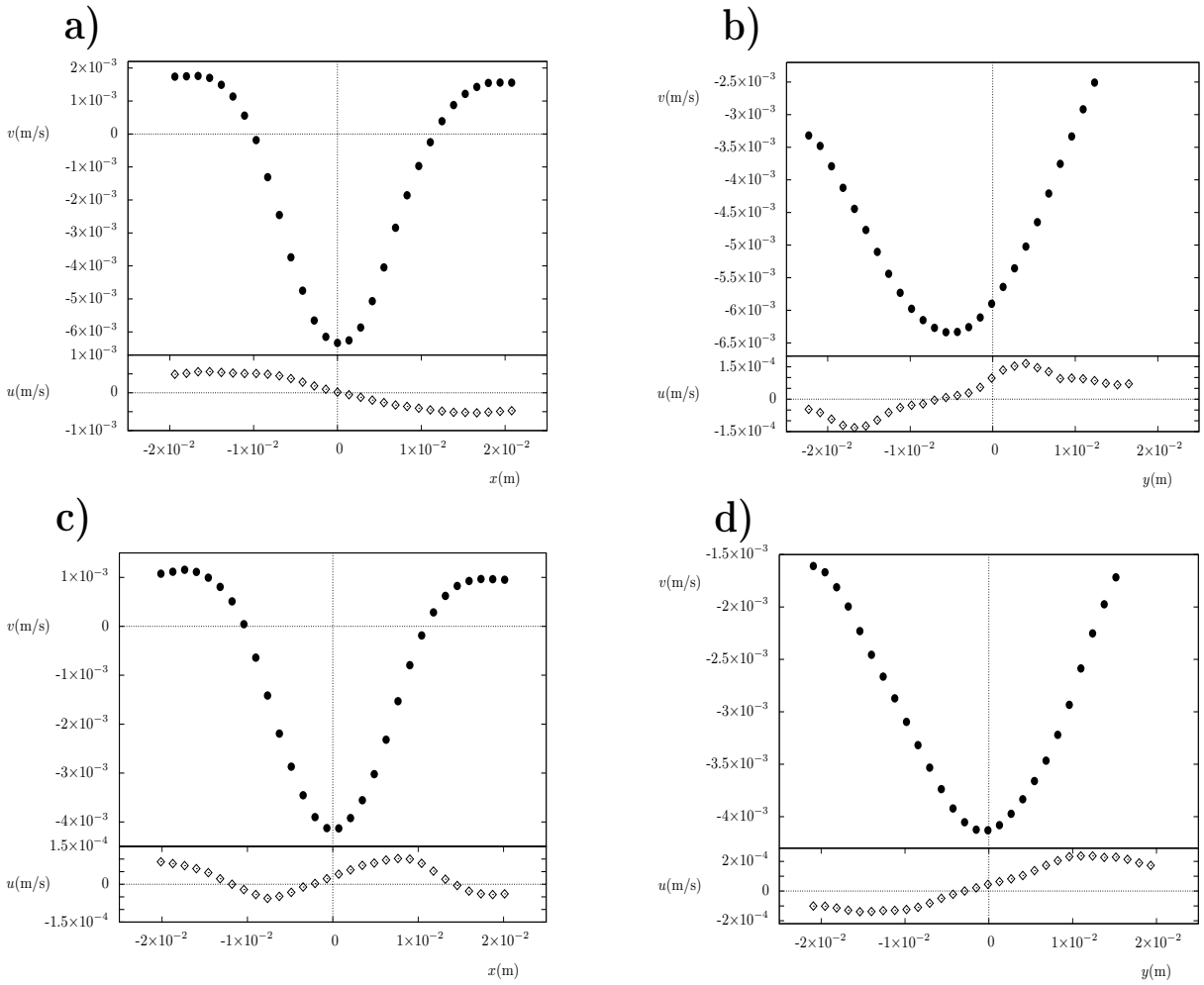

Figure 1.3: Velocities in the direction perpendicular (•) and parallel (◇) to the injected electric current as a function of position for $I = 25$ mA. a) $y = 0$, $z = 3.5$ mm, $B_{max} = 0.14$ T ($Ha = 0.20$); b) $x = 0$, $z = 3.5$ mm, $B_{max} = 0.14$ T ($Ha = 0.20$); c) $y = 0$, $z = 1.5$ mm, $B_{max} = 0.19$ T ($Ha = 0.27$); d) $x = 0$, $z = 1.5$ mm, $B_{max} = 0.19$ T ($Ha = 0.27$). Note the change of scale in the ordinates.

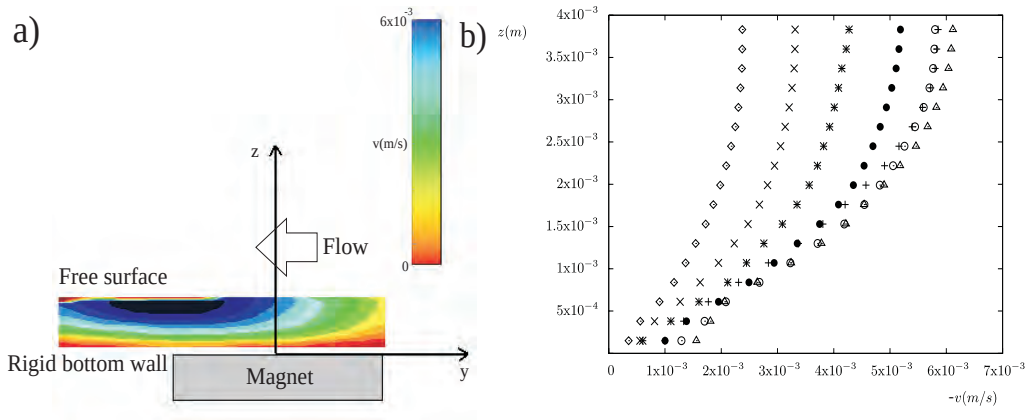

Figure 1.4: a) Magnitude of the velocity component perpendicular to the injected electric current (v) at the vertical $x = 0$ plane for $I = 25$ mA. b) Profiles of the v velocity component as a function of the depth z at the symmetry plane $x = 0$, for different positions upstream and downstream of the magnet center. $\diamond$, y=$0.53d$; $\times$, y=$0.33d$; $*$, $y = 0.19d$; $\bullet$, y=0; $\odot$, $y = -0.19d$; $\triangle$, $y = -0.38d$; $+$, $y = -0.58d$. At $z = 0$, $B_{max} = 0.22$ T ($Ha = 0.32$).

being the attenuation of velocity at the plane closer to the bottom wall. In turn, the profile of the u component (parallel to the injected current) as a function of the x-coordinate changes its shape from $z = 3.5$ mm to $z = 1.5$ mm as a result of a stronger bottom friction as well as a more intense Lorentz force. As a function of the y-coordinate, the v component shows a marked asymmetry dictated by the main flow direction. This asymmetry is stronger at the plane $z = 3.5$ mm, closer to the free surface (see figure 1.3(b)) where convective effects displace the maximum velocity downstream from the point of maximum magnetic field strength. The influence of the bottom friction is clearly noticed in figure 1.3(d) where, in addition to the attenuation, the maximum v velocity is reached at the point of maximum magnetic field strength. To estimate the rate of attenuation as a function of the distance to the bottom wall, we made PIV measurements at planes normal to this wall.

1.2.2 Flow measurements in vertical planes

In order to get PIV measurements at planes normal to the bottom wall, we turned around the light sheet 90° to obtain a vertical light plane which entered the cell

through the glass wall. A $50\% - 50\%$ cubic prism (2 cm $\times$ 2 cm $\times$ 2 cm) was placed inside the cell at a distance of 15 cm from the illuminated plane. The light reflected by the particle tracers was refracted 90° by the prism and captured by the camera, as shown in figure 1.1(c). The total area of analysis in this arrangement was 4.1 mm $\times$ 28 mm and we used interrogation areas of 16 $\times$ 64 pixels or equivalently 0.23 mm $\times$ 0.92 mm. This relatively large aspect ratio interrogation area was used since the vertical velocity is extremely small. An adaptive correlation with an overlap of 50% gave the best results. With this arrangement we could get a minimum of 18 points in the vertical direction, which is considered to resolve the boundary layer. In all reported PIV measurements, the rejected vectors were $2 - 3\%$ which is smaller than the recommendend 5%. Observations in the plane normal to the bottom wall are useful to determine the quasi-two-dimensionality of the flow. The general feature of the flow as observed in the $y - z$ plane is that the z-component of the velocity is three orders of magnitude smaller than the y-component, indicating that the flow is mostly in the horizontal direction with negligible vertical motion. In fact, no recirculations were observed in the $y - z$ plane within the explored range of injected currents. Figure 1.4(a) displays the magnitude of the velocity as a function of position in the vertical $x = 0$ plane at the region above the magnet for $I = 25$ mA. The figure shows the reduction of velocity as the fluid gets closer to the bottom wall, while due to convective effects, the overall maximum value is attained in the region close to the free surface, downstream from the point of maximum magnetic field strength. The flow development as the fluid traverses the non-homogeneous magnetic field region is shown in figure 1.4(b), where the negative of the y-velocity component v as function of the vertical coordinate z, is displayed for several locations in the y-direction. All profiles are increasing functions of the coordinate z and display $\partial v/\partial z = 0$ at the free surface. The maximum velocity at $y = 0.53d$, the most upstream location observed, is a factor of three smaller than the corresponding value for $y = -0.58d$, which shows the acceleration transmitted to the fluid by the Lorentz force in this region. The global maximum velocity is observed downstream of the magnet center at $y = -0.38d$, while at $y = -0.58d$, the flow has slowed down and the velocity profile almost coincides with the profile at position $y = -0.19d$. Mass is of course conserved since at this location the flow is slightly divergent (see figure 1.2(a)). Due to the presence of the magnetic field, two distinctive features are displayed in these profiles, namely, the flattening of the profiles, clearly observed at $y = 0.33d$, $y = 0.19d$, and $y = 0$ and the appearance of incipient inflection points close to the bottom wall. Since the Hartmann number is very small, the flattening

cannot be attributed to induced effects but, as will be shown, to the variation of the applied field in the normal direction.

1.3 Theoretical model

The theoretical model considers the main features of the experimental situation, namely, a thin layer of a conducting incompressible viscous fluid with a free surface, contained in a rectangular rigid box under a localized non-uniform magnetic field, $\boldsymbol{B}^0 = \boldsymbol{B}^0(x, y, z)$. The field is produced by a dipole magnet located at the insulating bottom wall with its dipole moment pointing in the normal z-direction, located in the geometrical center of the container. A uniform steady electric current density injected in the positive x-direction interacts with the applied field giving rise to a rotational Lorentz force that stirs the fluid. The total current density is given by the injected current plus the current induced by the motion of the fluid within the applied magnetic field. In turn, the total magnetic field is composed by the applied field plus the field generated by induced currents. We assume that the induced field remains very small in comparison with the applied field, in other words, that the magnetic Reynolds number, $Rm = \mu\sigma U_0 L$, is much less than unity, a condition fully satisfied in the experiment. Here, σ and μ are the electric conductivity and magnetic permeability of the fluid, respectively, and U_0 and L are a characteristic velocity and length, respectively, to be defined below. By neglecting $\mathcal{O}(Rm)$ terms, the governing equations of motion can be expressed as

$$\boldsymbol{\nabla} \cdot \boldsymbol{u} = 0, \tag{1.1}$$

$$\frac{\partial \boldsymbol{u}}{\partial t} + (\boldsymbol{u} \cdot \boldsymbol{\nabla})\boldsymbol{u} = -\frac{1}{\rho}\boldsymbol{\nabla} p + \nu \boldsymbol{\nabla}^2 \boldsymbol{u} + \frac{1}{\rho}(\boldsymbol{j}^0 \times \boldsymbol{B}^0 + \boldsymbol{j}^i \times \boldsymbol{B}^0), \tag{1.2}$$

where the last term on the right-hand side of equation (1.2) considers the Lorentz force due to both the injected ($\boldsymbol{j}^0 = j^0 \hat{\boldsymbol{x}}$) and induced ($\boldsymbol{j}^i$) current densities. In the previous equation ρ and ν denote the mass density and kinematic viscosity of the fluid.

From the electromagnetic equations in the quasi-static approximation (Moreau 1990) we can get the so-called induction equation that, neglecting $\mathcal{O}(Rm)$ terms, reads

$$0 = \frac{1}{\mu\sigma}\boldsymbol{\nabla}^2\boldsymbol{b} + (\boldsymbol{B}^0\cdot\boldsymbol{\nabla})\boldsymbol{u} - (\boldsymbol{u}\cdot\boldsymbol{\nabla})\boldsymbol{B}^0, \tag{1.3}$$

where the induced magnetic field, $\boldsymbol{b}$, implicitly satisfies the equations

$$\boldsymbol{\nabla}\cdot\boldsymbol{b} = 0, \tag{1.4}$$
$$\boldsymbol{\nabla}\times\boldsymbol{b} = \mu\boldsymbol{j}^i. \tag{1.5}$$

Ampere's law (1.5) gives an expression to calculate induced electric currents once $\boldsymbol{b}$ is determined and guarantees that the electric current density is divergence-free, $\nabla\cdot\boldsymbol{j}^i = 0$. Further, the applied magnetic field $\boldsymbol{B}^0$ must satisfy the magnetostatic equations (Moreau 1990),

$$\boldsymbol{\nabla}\cdot\boldsymbol{B}^0 = 0, \qquad \boldsymbol{\nabla}\times\boldsymbol{B}^0 = 0, \tag{1.6}$$

which assure its solenoidal and irrotational character.

1.3.1 Quasi-two-dimensional numerical model

Vortical flows in shallow layers have been successfully modeled in both hydrodynamic (Zavala Sansón, van Heijst & Backx 2001; Clercx, van Heijst & Zoeteweij 2003) and MHD flows (Sommeria 1988a) using a quasi-two-dimensional approach that involves the intergration (averaging) of governing equations in the vertical direction or along the magnetic field lines. Here, we follow an averaging approach recently presented by Cuevas *et al.* (2006) (see also Lavrent'ev *et al.* 1990 and Smolentsev 1997) in the analysis of the flow past a localized magnetic field where both Hartmann and classic viscous boundary layers are considered. However, in the present contribution an important difference is introduced, since the dependence of the applied magnetic field on the z-coordinate is considered.

A fundamental ingredient of the numerical solution is the accurate modelling of the applied magnetic field. In fact, for flows in shallow layers, a good agreement between numerical and experimental velocity fields depends to a great extent on a good theoretical reproduction of the dominant normal component according with the experimental measurements. The transversal components seem to have a weak influence. Therefore, we assume that the only non-negligible component is the normal one (straight magnetic field approximation (Alboussière 2004)).

For the permanent magnet used in the experiments, the normal dimensionless magnetic field component was reproduced analytically through the expression

$$B_z^0(x, y, z) = \mathcal{B}_z^0(x, y)g(z), \tag{1.7}$$

which is normalized by the maximum magnetic field strength at a given horizontal plane, B_{max}. Here, $\mathcal{B}_z^0(x, y)$ reproduces the variation of the field in the $(x - y)$ plane using an analytical expression for the field of a magnetized rectangular surface uniformly polarized in the normal direction (McCaig 1977; Cuevas *et al.* 2006). We considered the field created by the superposition of two parallel magnetized square surfaces of side length L, with opposing polarization axes and separated by a distance c, so that the external surfaces acted as the north and south poles of the permanent magnet. L was taken as the characteristic length in the $(x - y)$ plane and was used to normalize coordinates x and y. Although experiments were carried out using a cylindrical magnet, a good fit with experimental values can be obtained using square magnetized surfaces provided measurements correspond to planes separated from the surface of the magnet, so that border effects are smoothed out. The strength of the normal component of the magnetic field was measured at different planes from the magnet surface corresponding with the flow planes explored experimentally using the PIV. For each plane, the lengths L and c used in the fitting, were chosen so that the distribution of magnetic field matches with the experimentally measured corresponding distribution. The comparison between experimental measurements and the fitting based on the expression by McCaig (1977) for the plane $z = 3.5$ mm, is presented in figure 1.5(a). The fitting is excellent except in the nighbourhood of one of the edges of the magnet where a small asymmetry in the field distribution is detected. Appart from this detail, the field distribution can be considered axially symmetric. In turn, the function $g(z)$ in equation (1.7), that introduces the field variation in the normal direction, was obtained from the fitting of the experimental data in the form

$$g(z) = \exp(-\gamma\varepsilon z), \tag{1.8}$$

where z is normalized by the depth of the layer, h, at a given vertical position, and $\gamma = 2.05$. Here $\varepsilon = h/L$ is the aspect ratio that compares the characteristic lengths in normal and transversal directions. Figure 1.5(b) compares the experimental measurements and the fitting obtained from equation (1.8).

In addition, we assume that the transport of momentum in the normal direction is mainly diffusive, so that the dimensionless velocity components in the

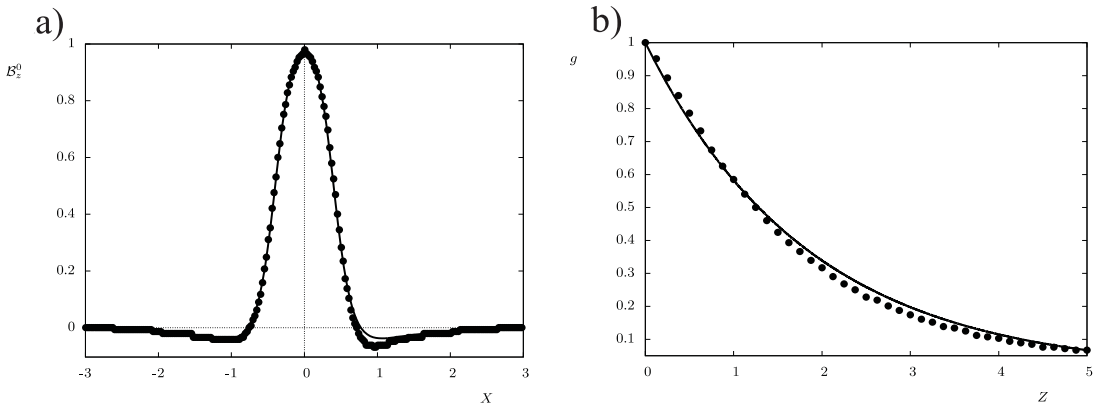

Figure 1.5: a) Normalized z-component of the magnetic field at $z = 3.5$ mm as a function of x. The continuous line is the fitting based on the analytic expression (see McCaig 1977) for magnetized surfaces of side length $L = 15.2$ mm separated by a distance $c = 14$ mm. b) Normalized z-component of the magnetic field as a function of the vertical coordinate z. The region $z \leq 1$ corresponds to the layer thickness. The continuous line is the fitting based on equation (1.8) with $\gamma = 2.05$. In both figures, black dots correspond to experimental measurements.

$(x - y)$ plane can be expressed as

$$u(x, y, z, t) = \bar{u}(x, y, t)\ \hat{f}, \qquad u(x, y, z, t) = \bar{u}(x, y, t)\ \hat{f}. \tag{1.9}$$

The components u and v are normalized by $u_0 = \nu/L$, and time, t, is normalized by the viscous time L^2/ν. The functions $\bar{u}$ and $\bar{v}$ denote the averaged velocity components in the $(x - y)$ plane. The function $\hat{f}$ may, in principle, depend on x, y and z, and satisfies the normalization condition $\int_0^{\varepsilon} \hat{f} dz = 1$. According to the shallow flow approximation, ε is assumed to be less than unity (in the experiment, the maximum value of ε, obtained at the free surface, is 0.21). The function $\hat{f}$ should reproduce the velocity profile in the normal direction both in the neighbourhood of the magnet and far from it. The explicit form of $\hat{f}$ can be obtained from a balance between viscous and Lorentz forces generated by both injected and induced currents. Since the applied Lorentz force points in the negative y-direction and is maximum in the center of the magnet, we establish the balance at the central $(y - z)$-plane ($x = 0$). Then, f must satisfy the equation

$$\frac{d^2 f}{dz^2} - (Ha \mathcal{B}_z^0 g)^2 f = \varepsilon^2\ Re_*\ \mathcal{B}_z^0 g. \tag{1.10}$$

In equation (1.10) the function f has still to be normalized. In turn, the Reynolds number $Re_* = U_0 L/\nu$, is based on the characteristic bulk velocity $U_0 = j^0 B_{max} L^2/\rho\nu$, obtained from a balance between viscous and applied Lorentz forces. Note, however, that this balance only considers lateral viscous diffusion and does not take into account the friction at the bottom wall. Therefore, Re_* does not coincide with the experimental Reynolds number based on the maximum velocity at a given flow plane. The terms on the left-hand side of equation (1.10) correspond to the viscous and induced Lorentz forces while the term on the right-hand side is the applied Lorentz force. Since in the experiments the Hartmann number is of order 10^{-1}, the induced Lorentz force in equation (1.10) can be neglected. Further, f must satisfy non-slip conditions at the bottom wall ($f(z=0)=0$) and the absence of shear stresses at the free surface ($df/dz(z=\varepsilon)=0$). Once it is normalized, $\hat{f}$ takes the form

$$\hat{f} = \frac{\left[e^{-\gamma z} + z\gamma\varepsilon e^{-\gamma\varepsilon^2} - 1\right]}{\frac{1}{\gamma\varepsilon}(1-e^{-\gamma\varepsilon^2}) + \frac{\gamma\varepsilon^3}{2}e^{-\gamma\varepsilon^2} - \varepsilon}. \tag{1.11}$$

Due to normalization, $\hat{f}$ is independent of $\mathcal{B}_z^0$ and Re_*. An averaged quasi-two-dimensional system of equations can now be obtained if equations (1.7)-(1.9) and (1.11) are substituted in (1.1) and (1.2) and integrated in the z-coordinate from 0 to ε, assuming that the bottom wall and the free surface are electrically insulated. If the electric current density and the induced magnetic field are normalized, respectively, by j^0 and RmB_{max}, it can be shown that the induced Lorentz force is of order Ha^2 and, consequently, can be neglected in equation (1.2). Therefore, the averaged equations of motion in dimensionless form read

$$\frac{\partial u}{\partial x} + \frac{\partial v}{\partial y} = 0, \tag{1.12}$$

$$\frac{\partial u}{\partial t} + \left(u\frac{\partial u}{\partial x} + v\frac{\partial u}{\partial y}\right) = -\frac{\partial p}{\partial x} + \nabla_\perp^2 u - \frac{u}{\tau}, \tag{1.13}$$

$$\frac{\partial v}{\partial t} + \left(u\frac{\partial v}{\partial x} + v\frac{\partial v}{\partial y}\right) = -\frac{\partial p}{\partial y} + \nabla_\perp^2 v - \frac{v}{\tau} - \alpha Re_* \mathcal{B}_z^0, \tag{1.14}$$

where the overline in the velocity components has been dropped, the pressure, p, is normalized by ρu_0^2, and the subindex $\perp$ denotes the projection of the ∇^2 operator on the $(x-y)$ plane. Velocity components statisfy non-slip conditions

at the boundaries of the container. Note that in the absence of injected current, $Re_* = 0$ and no motion exists. In the right-hand side of equations (1.13) and (1.14) appears a linear term accounting for the effects of viscous boundary layers at the bottom wall. This term involves a (dimensionless) characteristic time scale, τ, for the damping of vorticity due to dissipation in the viscous layers, and whose inverse is given by

$$\tau^{-1} = \frac{1}{\varepsilon^2}\frac{d\hat{f}}{dz}\Bigg]_0^{\varepsilon} = \frac{\gamma(1-e^{-\gamma\varepsilon^2})}{\frac{1}{\gamma}(1-e^{-\gamma\varepsilon^2}) + \frac{\gamma\varepsilon^4}{2}e^{-\gamma\varepsilon^2} - \varepsilon^2}. \tag{1.15}$$

Further, due to the variation of the magnetic field in the normal direction, the Lorentz force term in equation (1.14) includes the factor α given by

$$\alpha = \int_0^{\varepsilon} g(z)dz = \frac{1}{\gamma\varepsilon}(1-e^{-\gamma\varepsilon^2}). \tag{1.16}$$

The inductionless system of equations (1.12)-(1.16) was used to model the electromagnetically driven flow at different depths in the shallow layer.

1.4 Comparison of numerical model with experimental observations

1.4.1 The friction model

In shallow flows, a good quantitative numerical reproduction of experimental results relies to a great extent in the correct assessment of bottom friction effects that, due to the small value of the Hartmann number, in the present experiments are mainly of viscous origin. In our simulation this is accomplished through the linear friction model (see equations (1.11)-(1.15)) that results from the averaging of the governing equations in the normal direction, using the velocity distribution (1.11) in this direction. Reliability of the averaging procedure depends, in turn, on the proper modelling of the velocity profiles in the depth of the shallow layer. In figures 1.6(a–c), the scaled analytical profiles given by equation (1.11) are compared against experimental profiles of the velocity component in the y-direction (v) as functions of the z-coordinate at different y-positions and at $x = 0$, corresponding to $I = 25$ mA. The continuous line in figures 1.6 shows the fit of the analytical velocity profile (1.11), properly scaled by a constant, obtained with the maximum aspect ratio, $\varepsilon = 0.21$. The comparison shown in figures

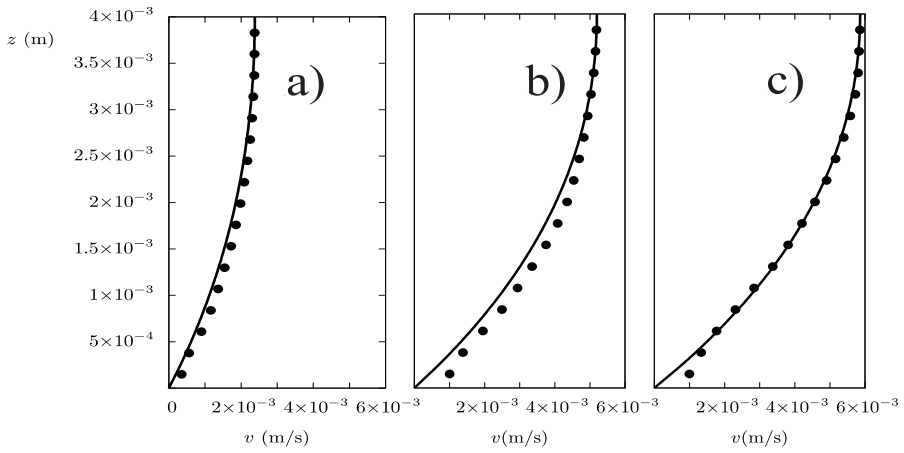

Figure 1.6: The v-component of velocity as a function of z for $I = 25$ mA at $x = 0$. a) $y = 0.53d$; b) $y = 0$; c) $y = -0.58d$. Dots are experimental data and continuous lines show the scaled velocity profiles from equation (1.11).

1.6(a–c), indicates that the shape of the developing experimental observations as the flow traverses the non-homogeneous magnetic field region can be adequately reproduced by the velocity profile (1.11) that considers the decay of the magnetic field strength in the vertical direction. In fact, the observed flattening of the profile seems to be due to this effect. It is therefore expected a reasonable assessment of the bottom friction based on this velocity profile. However, an important point has to be noted. A careful observation of experimental velocity profiles (see also figure 1.4(b)) reveals the existence of incipient inflection points located very close to the bottom wall that cannot be captured with profile (1.11).

1.4.2 General features of the flow structure

The system of equations (1.12)-(1.14) with the friction model based on equations (1.11) and (1.15) and the magnetic field distribution given from the analytic expression by McCaig (1977), was solved numerically in a rectangular domain corresponding to the dimensions of the experimental setup, using a finite difference method based on the procedure described in Griebel, Dornseifer & Neunhoeffer (1998), adapted to consider MHD flows. A detailed explanation of the numerical procedure can be found in Cuevas *et al.* (2006).

In figure 1.7, the velocity components in the horizontal plane predicted by the

theoretical model (see § 1.3) are compared with experimental results for the case $I = 25$ mA at the plane $z = 3.5$ mm ($Re_{max} = 110$). Symbols correspond to experimental values while continuous and dotted lines denote numerical predictions. Figure 1.7(a), shows both velocity components as functions of the x-coordinate at the center line $y = 0$. The velocity distribution is symmetric for the component v, in the direction perpendicular to the injected current, and antisymmetric for the component u, parallel to the injected current. The slight asymmetry of the experimental (positive) values of v, reflects the corresponding asymmetry in the magnetic field distribution of the magnet shown in figure 1.5(a). The velocity profiles along the symmetry line ($x = 0$) are given in figure 1.7(b). As noted in § 1.2.1, due to convective effects the maximum value of component v is not reached at $y = 0$ but downstream. The continuous lines correspond to numerical results obtained with the experimental conditions, $I = 25$ mA, $B_{max} = 0.14$ T and $z = 3.5$ mm ($\varepsilon = 0.18$). The numerical prediction of the v profile as a function of x and y underestimates the magnitude of the velocity by less than 15%, hence, a quasi-two-dimensional description of electromagnetically forced shallow laminar flows seems to be compatible with experimental results. In fact, the model reproduces the main physical effects observed experimentally. For instance, it predicts correctly the position where the profile changes from negative to positive values (see figure 1.7(a)). Further, we observe in figure 1.7(b) that the position of the maximum velocity is correctly predicted which indicates that convective effects are suitably captured by the model. The dotted lines in figure 1.7, that approach closer to the experimental results, correspond to calculations performed for the plane $z = 4.0$ mm ($\varepsilon = 0.21$). Note that the difference in the plane position is within the uncertainity of the position of the laser sheet, namely, $\pm$ 0.7 mm.

1.4.3 Flow features as functions of the applied current

The main effects of increasing the applied current is the elongation of the vortices in the main direction of the localized Lorentz force. This was briefly described in § 1.2.1 and illustrated in figure 1.2(b). In fact, the centers of the recirculation regions as well as the location of maximum velocity are convected a larger distance in the direction of the main Lorentz force for larger electric currents. This effect is correctly predicted by the model. In table 1.1, the experimental y-positions of the maximum velocity as function of the electrical current are shown together with the predictions of the model at the plane $z = 3.5$ mm. In all cases, the abscissa of the maximum velocity is $x = 0$. The relative error is smaller than

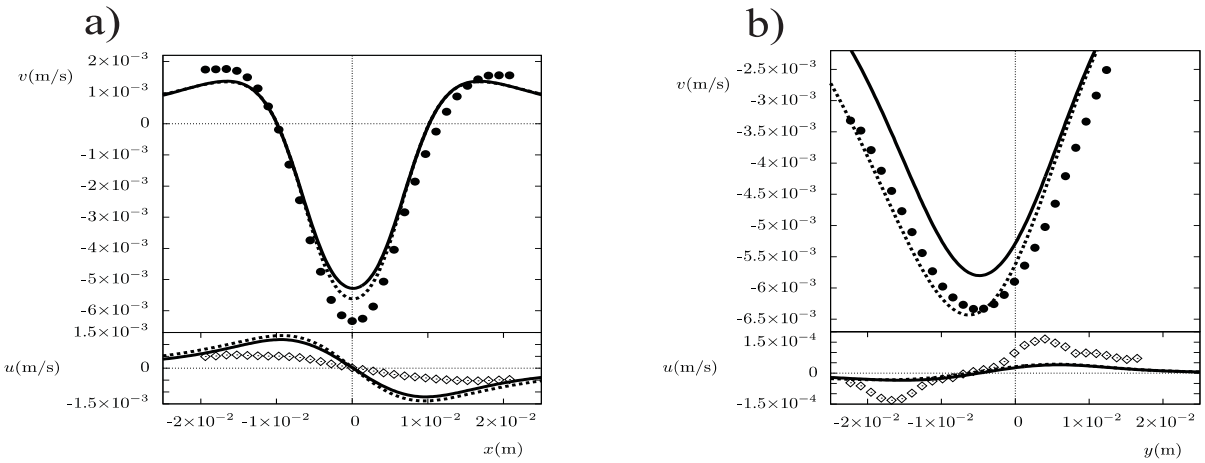

Figure 1.7: Experimental velocities in the direction perpendicular (•) and parallel (⋄) to the injected electric current as functions of position for $I = 25$ mA, $z = 3.5$ mm. a) $y = 0$, b) $x = 0$. Continuous lines show numerical simulations for $I = 25$ mA, $z = 3.5$ mm. Dotted lines show numerical simulations for $I = 25$ mA, $z = 4.0$ mm.

I (mA)	y_e(m)	y_n(m)	$(y_e - y_n)/\overline{y}$
10	-2.1×10^{-3}	-2.3×10^{-3}	-0.090
15	-3.5×10^{-3}	-3.3×10^{-3}	0.059
20	-4.9×10^{-3}	-4.1×10^{-3}	0.178
25	-4.5×10^{-3}	-4.9×10^{-3}	-0.085
30	-4.9×10^{-3}	-5.6×10^{-3}	-0.133
40	-6.2×10^{-3}	-6.6×10^{-3}	-0.062
50	-7.6×10^{-3}	-7.4×10^{-3}	0.026
60	-7.6×10^{-3}	-7.9×10^{-3}	-0.039
70	-9.0×10^{-3}	-8.4×10^{-3}	0.069
80	-9.0×10^{-3}	-8.6×10^{-3}	0.045
90	-1.04×10^{-2}	-8.9×10^{-3}	0.155
100	-1.04×10^{-2}	-9.1×10^{-3}	0.133

Table 1.1: y-positions of the points of maximum velocity as functions of electric current at $z = 3.5$ mm. The subscripts e and n indicate the experimental measurements and numerical calculations, respectively. $\overline{y} = (y_e + y_n)/2$.

18% and less than 10% for most cases.

In figure 1.8, the experimental results and numerical predictions of the absolute value of the maximum flow velocity (v_{max}) at the plane $z = 3.5$ mm are shown as a function of the imposed electric current. Four measured values are reported in the curve for every electric current strength. The experimental observations fit the curve $|v_{max}| = -8 \times 10^{-7} I^2 + 2 \times 10^{-4} I + 5 \times 10^{-4}$. The numerical results present a very good quantitative agreement with experimental measurements in the full range of explored electric currents. These results indicate that the quasi-two-dimensional model is able to reproduce the steady electromagnetically forced flow in the shallow layer.

1.5 Discussion

In this Chapter, we have presented PIV observations of laminar vortex dipoles driven by the interaction of a uniform D.C. injected current and the field produced by a small permanent magnet in a shallow layer of an electrolyte. In contrast with high-Hartmann number electrolytic flows (Andreev, Heberstroh & Thess 2001), the very small values of Ha in the present experiment ($\mathcal{O}(10^{-1})$) lead to

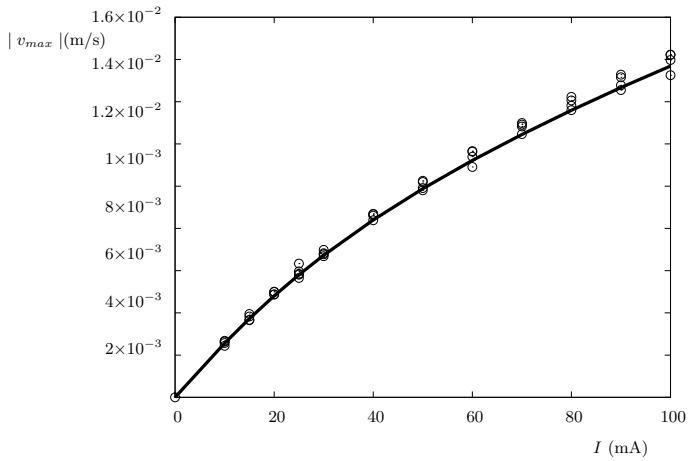

Figure 1.8: Absolute value of the maximum velocity ($|v_{max}|$) as a function of the applied current I at the plane $z = 3.5$ mm. Each symbol corresponds to an individual experimental observation. The continuous line corresponds to numerical simulations.

negligible induced effects and to the predominance of viscous and imposed non-uniform Lorentz forces. Although several experimental studies have addressed the decay properties of vortical shallow flows of electrolytes initially generated by electromagnetic forcing, the detailed exploration and modelling of flows in shallow layers continuously stirred by localized electromagnetic forces have, to the best of our knowledge, not been previously considered. The presumption of quasi-two-dimensionality of these flows was corroborated by exploring flow planes parallel to the bottom wall at different depths as well as flow planes normal to this wall, so that an approximate three-dimensional picture of the flow structure was reconstructed. For small injected currents, a quite symmetric dipolar vortex structure is formed mainly by diffusive momentum transport. As the current is increased, convective effects are manifested by the elongation of the vortices in the main direction of the Lorentz force along with the displacement of the point of maximum velocity downstream. The damping of velocity due to bottom friction was measured at flow planes close to the bottom wall and by looking at planes normal to that wall. In fact, it appears that the experimental measurement of velocity profiles in the vertical direction in electromagnetically driven shallow flows have been overlooked in the past. In spite of the weakness of the applied

magnetic field, this information reveals developing velocity profiles with a shape that depends on the location within the non-uniform magnetic field region and, in particular, on the field strength in the normal direction. Based on the maximum velocity near the free surface, the Reynolds numbers of the flow varied from 50, for injected currents of 10 mA, to 290 for 100 mA. Under the explored conditions, no recirculations were observed in planes normal to the bottom wall indicating that the transport of momentum in the normal direction is mainly diffusive. However, the velocity profiles at the entrance to the magnetic field region are marked by the appearance of incipient inflection points that, for stronger injected currents, might lead to the instability of the boundary layer. The exploration of this effect may deserve further study.

A quasi-two-dimensional model was introduced and numerical simulations were compared with available experimental results. This simple model, that correctly captures the main physical features of the basic flow and avoids difficulties of a full three-dimensional approach, includes convective effects and involves the integration (averaging) of governing equations in the vertical direction. Since the depth of the electrolyte layer is much smaller than its horizontal extension, the local magnetic field originated by a permanent dipole magnet can be realistically approximated by considering only its component in the vertical direction. This assumption, that greatly simplifies the analysis, seems to be more justified for shallow flows than for duct flows in non-homogeneous magnetic fields (Alboussière 2004). The vertical field component is modeled analytically and fitted accurately to reproduce the experimental field. The results reported in the present study show that a quasi-two-dimensional flow description is suitable. In general, a good quantitative comparison is found between numerical results and experimental observations. One of the key elements that allow an accurate estimation of the bottom viscous friction and the magnitude of the Lorentz force is to consider the variation of the magnetic field strength in the vertical direction. In fact, the observed flattened profiles in the zone of more intense magnetic field are due precisely to this variation. The model seems to be a useful tool for the analysis of steady electromagnetically forced flows at low-Hartmann and intermediate Reynolds (< 300) numbers in shallow layers of electrolytes.

Chapter 2

Stokes layer in oscillatory dipolar vortex flow

In this Chapter[1], we report experimental observations of the laminar flow generated by the concurrent action of an alternate, unidirectional electric current and a localized dipolar magnetic field in a thin (4 mm), horizontal layer of electrolyte. The time-dependent Lorentz force generates a periodically oscillating dipolar vortex which displays some spatial and temporal symmetries.

The attention is focused on the motion of the oscillatory layer in planes perpendicular to both the bottom wall and the injected current. The flow is analogous to the Stokes's oscillating plate problem but with a body force (Lorentz force) driving the motion. Velocity fields were obtained using Particle Image Velocimetry at different flow planes in the zone of more intense magnetic field as well as close to the edge of the magnet where the inhomogeneity of the field is more pronounced. Four different frequencies of the injected current were explored, namely, 10, 50, 100, and 200 mHz, with a fixed amplitude of 70 mA. Velocity profiles as functions of the normal coordinate are determined in characteristic points at different phases and oscillation frequencies. Experimental results are compared with a simple analytical solution derived from the balance of inertial, viscous and electromagnetic forces that considers the decay of the magnetic field in the normal direction. Further, a full three-dimensional numerical simulation that reproduces satisfactorily the experimental observations, was implemented. Under the explored conditions and available experimental resolu-

[1]This Chapter is mainly based on the paper: Figueroa, A., Cuevas, S. & Ramos, E., 2010, "Stokes layer in electromagnetically driven oscillatory dipolar vortex". Submitted to *Phys. Fluids*.

tion, results indicate that except in the zone above of the lateral edges of the magnet, no recirculating flows appear and vertical velocity components are negligible. In the lateral edge zone, velocity components are at least one order of magnitude smaller than components in the central region.

2.1 Introduction

Electromagnetically driven flows in shallow layers of electrolytes have been widely used for the study of vortex dynamics and mixing. In these flows, an injected electric current interacts with an imposed magnetic field created by permenent magnets to generate a Lorentz force that stirs the fluid. In the past, thin fluid layers have been used to study the decay of quasi-two-dimensional (Q2D) turbulence by assuming that the small depth of the layer as compared with its horizontal extension ensures the quasi-two-dimensionality of the flow. In this context, there has been a great interest in clarifying the existence and intensity of three-dimensional (3D) structures in shallow layers driven by electromagnetic forces. Proof of the existence of three dimensional vortical structures in a flow generated by a pulse force in shallow layers was provided by Akkermans *et al.* (2008a; 2008b). These authors studied a dipolar vortex in a shallow electrolytic layer of 9.3 mm thickness created by a single 1 s constant current pulse of 4.4 A interacting with the nonuniform field of a disk-shaped magnet. They report significant 3D structures and vertical motions occurring throughout the flow evolution, during and after the forcing phase. These results have been confirmed and extended by numerical simulation. In turn, Lardeau *et al.* (2008) analyzed through 3D numerical simulations the flow driven by the interaction of a uniform external current and the field created by a multiscale distribution of pairs of magnets in a 5 mm electrolytic layer. Results were compared with experimental data (Rossi *et al.* 2006; Ferrari *et al.* 2008). They concluded that 3D simulations are required to model multiscale shallow flows driven by electromagnetic forcing. In particular, they found that the usual approach of considering a Rayleigh friction to model the bottom wall-normal friction in the form $-\alpha\boldsymbol{u}$, where $\boldsymbol{u}$ is the velocity field and α is a constant friction coefficient, is not appropriate to model the broad range of forcing intensities occurring across the shallow layer. On the other hand, Figueroa *et al.* (2009) analyzed a steady dipolar vortex flow continuously driven by the interaction of a dc uniform electric current and the magnetic field produced by a small dipolar permanent magnet in an electrolytic layer of 4 mm thickness, also described in Chapter 1. Velocity profiles in the

neighbourhood of the zone affected by the magnetic field were obtained with particle image velocimetry (PIV) in planes parallel and normal to the bottom wall. It was found that the boundary layer attached to the bottom wall shows a slightly flattened developing profile due to the variation of the magnetic field in the normal direction. No recirculations were observed under the explored experimental conditions. The main characteristic behavior of the flow was suitably reproduced through a Q2D numerical model that considers the decay of the magnetic field in the normal direction so that different forcing intensities across the thin fluid layer can be evaluated.

The analysis of the boundary layer existing between the rigid bottom wall and the upper free surface is, evidently, an essential element for determining the 3D structure of a shallow flow. Although it is clear that three-dimensionality is favoured the thicker the fluid layer, the influence of other factors that may promote the departure of the flow from a Q2D behavior and the formation of 3D flow patterns in electromagnetically driven flows, is worth evaluating. For instance, the time-dependent nature of the forcing, its strength, as well as inhomogeneities in the magnetic field, are important elements to be explored. This is a relevant issue since time-dependent forcing using localized magnetic fields is interesting for mixing purposes. In the present article, we analyze the behavior of the oscillating boundary layer created by the interaction of an alternate electric current and the magnetic field of a disk-shaped magnet in a thin electrolytic layer. In planes parallel to the bottom wall, the flow is visualized as an oscillating dipolar vortex (see figure 2.1) whose behavior was briefly described by Figueroa *et al.* (2008). A more complete description will be analyzed in Chapter 3. It is worth mentioning that the study of oscillatory vortices is interesting as a model to describe geophysical time-periodic flows (Wells *et al.* 2003; Kunnen *et al.* 2010).

Oscillatory boundary layers have been widely studied in different contexts. Stokes's solution (Stokes 1851) for the flow generated in a viscous fluid by an oscillating solid wall, represents the classic example of an oscillatory boundary layer. Owing to the invariance of the governing equations for incompressible flow under an unsteady Galilean transformation, Stokes's problem can be interpreted as produced by an oscillating free stream, created by an oscillating pressure gradient, in the presence of a fixed solid wall (Panton 2005).

Oscillatory boundary layers under magnetic fields have also been studied in the past. Motivated by the possibility of measuring in the laboratory the effect of a magnetic field on the propagation of sound in a tube containing mercury, Hide & Roberts (1960) analyzed the magnetohydrodynamic (MHD) extension of the

Stokes's problem. These authors addressed the problem in very general terms, considering the effect of a uniform rotation and a uniform magnetic field acting simultaneously on the flow of a conducting fluid produced by the oscillation of a solid insulating plane. More recently, the magnetic damping of steady streaming generated by oscillatory flows near rigid boundaries was analyzed (Cuevas & Ramos 1997; Cuevas *et al.* 2002). Oscillatory boundary layers also occur in the damping of surfaces waves through the action of a uniform transverse magnetic field (Srineevasan *et al.* 2005).

A common feature of the previous problems is that oscillatory motion is produced by a mechanical surface force, that is, an oscillating wall or piston. In contrast, the oscillatory boundary layer analyzed in the present contribution is generated by an imposed periodic Lorentz which is a nonuniform body force. The structure of the boundary layer in regions of different magnetic field intensity is explored experimentally through PIV following a methodology previously implemented for the analysis of steady boundary layers, see § 1.2.2. In addition, a Stokes-like analytic solution that reproduces qualitatively the velocity profiles in the vicinity of the point of maximum magnetic field strength is obtained. Results are complemented with 3D numerical simulations that present a good agreement with experiments.

2.2 Experimental procedure and observations

The experimental setup used in the present experiments was described somewhat in detail in § 1.2.2. The main modification with respect to the previous experiments is the injection through a pair of parallel electrodes of an alternate current instead of a dc current. The origin of coordinates is located at the bottom wall above the center of the magnet with the z-axis pointing normally. The velocity components in the x, y, and z-directions are denoted by (u, v, w). Once transients have died out, the flow generated by the Lorentz force that results from the simultaneous action of the alternate electric current injected in the x-direction and the localized magnetic field, gives rise to an oscillatory dipolar vortex in the $(x - y)$ plane, as shown in figure 2.1. The flow structure presents a symmetry line along the y axis, as is clearly observed in the picture. This means that a mirror symmetry is displayed by the flow with respect to the x coordinate:

$$\left.\begin{array}{l} u(x,y,t) = -u(-x,y,t), \\ v(x,y,t) = v(-x,y,t). \end{array}\right\} \tag{2.1}$$

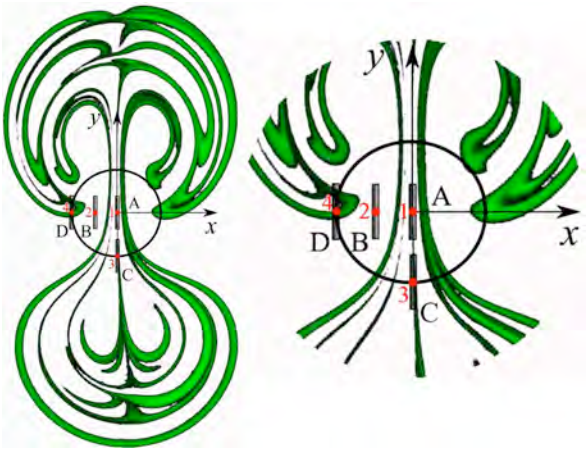

Figure 2.1: Left picture: plan view of the flow generated by the alternate electrical current injected in the x-direction and the field of a localized magnetic dipole magnetized in the normal z-direction. The circle denotes the footprint of the magnet and the visualization was made by injecting dyed water. Right picture: zoom of the central part of the flow. Lines A, B, C, and D indicate the position of the planes analyzed in § 2.4. The vertical velocity profiles described in figures 2.4, 2.5, 2.6, and 2.8 were obtained at points 1, 2, 3, and 4, respectively.

The formation of a pair of counter rotating lobes occurs every half cycle as the direction of the Lorentz force, that points mainly along the y-axis, is inverted. Therefore, the velocity components in the $(x-y)$ plane also show the following cyclic symmetry:

$$\left.\begin{array}{l} u(x,y,t) = u(x,-y,t+\pi), \\ v(x,y,t) = -v(x,-y,t+\pi). \end{array}\right\} \tag{2.2}$$

In the present experiments, the attention is focused on flow planes normal to both the bottom wall and the injected current, in the region above the magnet (see figure 2.2). The oscillatory behavior of the layer was investigated in four different $(y-z)$-planes denoted as A, B, C, and D in figure 2.1. Planes A and C lay along the symmetry axis covering the central and edge regions of the magnet, respectively. In turn, plane B is located half way between the symmetry axis and the left magnet edge, while plane D lies tangent to this magnet edge. The oscillatory forcing was produced by injecting a sinusoidal electric current from a *DS345* function generator system that produce a voltage of $\pm$ 10 V at

frequencies in the range 1 μHz to 30.2 MHz with 1 μHz frequency resolution. Four different current frequencies were explored, 10, 50, 100, and 200 mHz, while the amplitude of the injected current was kept fixed to 70 mA with a serially connected potentiometer. Electric signals were monitored with an oscilloscope and a digital multimeter ensuring their oscillatory nature. Experimental velocity fields were obtained using a PIV system (Dantec FlowMap PIV1100) with a double pulsed Nd : YAG laser from New Wave Research. Flow images were captured with a Kodak model Megaplus ES1.0/Type 16 (30Hz) camera, with a trigger sincronized with the illumination. The camera sits on a holder 10 cm above the fluid layer. The camera has a 1008 $\times$ 1016 pixels CCD and the actual area of the captured image is approximately 1 cm $\times$ 1 cm. The PIV software Dantec Flow Manager was used to perform the anaysis, we used interrrogation areas of 62 $\times$ 62 pixels with 50% overlap in x and y, cross correlation and peak validation. These conditions gave us a spatial resolution of 0.15 mm $\times$ 0.15 mm. The time interval for the PIV measurements was $T/20$, where T is the period of the forcing frequency. Avoiding the transient flow, we obtained 40 snapshots per cycle, the time interval between two subsequent images for the majority of experiments was 30 ms. Measurements were taken not caring about the phase of the forcing; in the data analysis they were reconstructed to fit the signal's phase. A minimum of 10 cycles were averaged for the frequencies 10 and 50 mHz, while only 5 cycles were averaged for the frequencies 100 and 200 mHz. This was due to a technical problem concerning the bus interconnection device of the PVI's flow map processor, that is, data measurements after 5 cycles for higher frequencies was lost or corrupted. The error in the velocity data was obtained by adjusting a normal distribution to the data at sample points.

2.3 Theoretical model

In flows driven by Lorentz forces created by the interaction of injected electric currents with applied magnetic fields in shallow electrolytic layers, induced effects are negligible (Figueroa *et al.* 2009). This means that currents induced by the motion of the fluid in the magnetic field, as well as Lorentz forces produced by these currents, can be completely disregarded. In this case, the flow is governed only by the continuity equation and the Navier-Stokes equation with the Lorentz force term. The latter is fully determined provided the injected current $\boldsymbol{j}_0$ and the applied magnetic field $\boldsymbol{B}^0$ are known. In dimensional terms the governing equations read

$$\boldsymbol{\nabla} \cdot \boldsymbol{u} = 0, \tag{2.3}$$

$$\frac{\partial \boldsymbol{u}}{\partial t} + (\boldsymbol{u} \cdot \boldsymbol{\nabla})\boldsymbol{u} = -\frac{1}{\rho}\boldsymbol{\nabla} p + \nu \boldsymbol{\nabla}^2 \boldsymbol{u} + \frac{1}{\rho}\boldsymbol{j}^0 \times \boldsymbol{B}^0, \tag{2.4}$$

where the last term on the right-hand side of equation (2.4) considers the oscillating Lorentz force created by the alternate current injected in the x-direction, namely, $\boldsymbol{j}^0 = j^0 \sin(\omega t)\, \hat{\boldsymbol{x}}$ where $\omega = 2\pi f$ is the angular frequency and f is the ordinary frequency. In addition, $\boldsymbol{B}^0 = \boldsymbol{B}^0(x, y, z)$ is the applied field produced by a permanent dipole magnet located under the insulating bottom wall with its dipole moment pointing in the normal z-direction (see figure 2.2). The origin of coordinates is placed at the bottom wall above the geometrical center of the magnet.

2.3.1 Unidimensional analytic solution

Let us first address the problem in a very simplified way that allows to obtain an analytic solution for the velocity profile in the symmetry plane of the flow ($x = 0$). We consider an infinite layer of electrolyte of thickness h limited in the lower boundary by a rigid insulating wall and in the upper boundary by a free surface. Let us assume that the imposed magnetic field consists only of the normal component, B_z^0, and therefore, an oscillating Lorentz force is produced in the y-direction. Since the magnetic field decays along the layer thickness, we consider that this component is a function of the vertical coordinate z. Hence, the Lorentz force will decrease from its maximum strength at the bottom wall to its minimum at the free surface. If border effects are disregarded, i.e. we do not consider any variation of the field in the x- or y-directions, the Lorentz force will drive a unidirectional oscillating flow that will depend only on the normal z-coordinate and time. By establishing the balance among inertial, viscous and Lorentz forces, the equation of motion can be expressed in the form

$$\frac{\partial v}{\partial t} = \nu \frac{\partial^2 v}{\partial z^2} - \frac{j^0}{\rho} \sin(\omega t) B_z^0(z). \tag{2.5}$$

The terms on the right-hand side of equation (2.5) correspond to the viscous and applied Lorentz forces, respectively. As assumed in equation 1.8, the magnetic field dependence on the normal coordinate can be simply expressed as

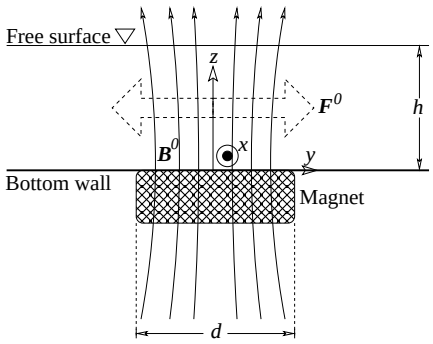

Figure 2.2: Sketch of the experimentally explored flow planes, not drawn to scale. The alternate electric current is injected perpendicular to the $(y-z)$-plane.

$$B_z^0(z) = B_o \exp(-\gamma z). \tag{2.6}$$

The strength $B_o = 0.224$ T and the rate of decay $\gamma = 138$ m^{-1} were found with measurements performed along the axis of the cylindrical permanent magnet used in the experiments. Neglecting the transient flow, the solution of equation (2.5) that satisfies non-slip conditions at the bottom wall ($v(z=0)=0$) and the absence of shear stresses at the free surface ($dv/dz(z=h)=0$) takes the form

$$v(t,z) = \Re\left\{ i\frac{j^0 B_o}{\rho\nu(\gamma^2 - 2i\delta^{-2})}\left[\frac{(\sqrt{2i}/\delta)\cosh(\sqrt{2i}(z-h)/\delta) - \gamma e^{-\gamma h}\sinh(\sqrt{2i}\,z/\delta)}{(\sqrt{2i}/\delta)\cosh(\sqrt{2i}h/\delta)} - e^{-\gamma z}\right] e^{i\,\omega t}\right\}, \tag{2.7}$$

where $\Re$ indicates the real part of the expression inside the brackets $\{\}$, and $\delta = \sqrt{2\nu/\omega}$ is the Stokes's layer thickness. As it will be shown in the next section, the solution (2.7) reproduces qualitatively the experimental velocity profiles in a small neighborhood where the magnetic field presents its maximum intensity. The main features of solution (2.7) can be better understood by analyzing a closely related situation which can be expressed in a simpler form, when the conducting fluid has no upper bound, as in the Stokes's classic problem (Stokes 1851). If we impose that the fluid velocity vanishes at infinity, a situation that is physically reasonable since the magnetic field decays as $z \to \infty$, the velocity profile is given by

$$v(t,z) = \frac{j^0 B_o}{\rho\nu(\gamma^4+4\delta^{-4})}\left\{e^{-\gamma z}\left[\frac{2}{\delta^2}\cos(\omega t)+\gamma^2\sin(\omega t)\right]\right.$$
$$\left.-e^{-z/\delta}\left[\frac{2}{\delta^2}\cos(\omega t-\frac{z}{\delta})+\gamma^2\sin(\omega t-\frac{z}{\delta})\right]\right\}. \quad (2.8)$$

We can clearly identify two different damping mechanisms in solution (2.8). The first term expresses a purely time-periodic motion modulated by the magnetic field decay. The second term is essentially a Stokes-like flow where viscous effects are responsible for the phase lag and the flow damping. Note that the characteristic length scale in the layer is determined necessarily by both mechanisms. The scales for the damping of the motion are γ and $1/\delta$. Hence, for $\gamma\delta < 1$, the characteristic thickness of the oscillatory boundary layer is mainly determined by viscous effects, while for $\gamma\delta > 1$, this thickness is determined by the decay of the magnetic field.

An interesting limit is obtained when a constant magnetic field is assumed. In that case $\gamma = 0$, and solution (2.8) presents the same time and space dependence as in the flow created by an oscillatory free stream:

$$v(t,z) = \frac{j^0 B_o \delta^2}{2\rho\nu}\left[\cos(\omega t) - e^{-z/\delta}\cos\left(\omega t - \frac{z}{\delta}\right)\right]. \quad (2.9)$$

Although formally solution (2.9) presents a similar structure as Panton's solution (Panton 2005), a basic difference exists since the latter is obtained through a surface force (an oscillatory pressure gradient) while the driving force in solution (2.9) is an electromagnetic body force.

2.3.2 Three-dimensional numerical solution

The previous analytical solutions are helpful for the physical understanding of the flow but their range of validity are rather limited. In fact, a simple analytical solution that includes border effects due to the finite size of the magnet, is not available. In general, border effects may promote the three-dimensionality of the flow and therefore, an accurate modeling requires a 3D numerical approach. By considering the interaction of the alternate current injected in the x-direction and the full (3D) magnetic filed, the governing equations of motion can be expressed as

$$\frac{\partial u}{\partial x}+\frac{\partial v}{\partial y}+\frac{\partial w}{\partial z}=0, \tag{2.10}$$

$$\frac{\partial u}{\partial t}+u\frac{\partial u}{\partial x}+v\frac{\partial u}{\partial y}+w\frac{\partial u}{\partial z}=-\frac{1}{\rho}\frac{\partial p}{\partial x}+\nu\nabla^2 u, \tag{2.11}$$

$$\frac{\partial v}{\partial t}+u\frac{\partial v}{\partial x}+v\frac{\partial v}{\partial y}+w\frac{\partial v}{\partial z}=-\frac{1}{\rho}\frac{\partial p}{\partial y}+\nu\nabla^2 v-\frac{j^0}{\rho}\sin(\omega t)B_z^0, \tag{2.12}$$

$$\frac{\partial w}{\partial t}+u\frac{\partial w}{\partial x}+v\frac{\partial w}{\partial y}+w\frac{\partial w}{\partial z}=-\frac{1}{\rho}\frac{\partial p}{\partial z}+\nu\nabla^2 w+\frac{j^0}{\rho}\sin(\omega t)B_y^0, \tag{2.13}$$

where B_y^0 and B_z^0 are the y and z components of the magnetic field, respectively. We must note that by considering the full magnetic filed a Lorentz force in the z-direction is created, see equation (2.13). In order to get the complete velocity field at different locations of the flow region, the system of equations (2.10)-(2.13) was solved numerically in a volume with a rectangular floor that corresponds to the dimensions of the experimental setup. A finite difference method based on the procedure described in Griebel *et al.* (1998) was adapted to include electromagnetic forces. The calculation of the oscillatory Lorentz force terms in equations (2.12-2.13) requieres the y and z components of the magnetic field distribution of the permanent magnet. With this purpose, a superposition of the magnetic fields produced by magnetized rectangular surfaces uniformly polarized in the normal direction was used (McCaig 1977). If we place the coordinate system in the center of a rectangular surface with side lengths $X = 2x_0$ and $Y = 2y_0$, the components of the three-dimensional field produced by a single magnetized surface laying on the plane $Z = z_0$, can be expressed

$$\begin{aligned} B_y^0(x,y,z) &= \varsigma B_o \log\left\{\left(\frac{(x+x_0)+\left[(x+x_0)^2+(y-y_0)^2+(z-z_0)^2\right]^{1/2}}{(x-x_0)+\left[(x-x_0)^2+(y-y_0)^2+(z-z_0)^2\right]^{1/2}}\right)\right. \\ &\left.\left(\frac{(x-x_0)+\left[(x-x_0)^2+(y+y_0)^2+(z-z_0)^2\right]^{1/2}}{(x+x_0)+\left[(x+x_0)^2+(y+y_0)^2+(z-z_0)^2\right]^{1/2}}\right)\right\}, \end{aligned} \tag{2.14}$$

$$
\begin{aligned}
B_z^0(x,y,z) &= \varsigma B_o \left\{ \tan^{-1}\left(\frac{(x+x_0)\,(y+y_0)}{(z-z_0)\left[(x+x_0)^2+(y+y_0)^2+(z-z_0)^2\right]^{1/2}} \right) \right. \\
&+ \tan^{-1}\left(\frac{(x-x_0)\,(y-y_0)}{(z-z_0)\left[(x-x_0)^2+(y-y_0)^2+(z-z_0)^2\right]^{1/2}} \right) \\
&- \tan^{-1}\left(\frac{(x+x_0)\,(y-y_0)}{(z-z_0)\left[(x+x_0)^2+(y-y_0)^2+(z-z_0)^2\right]^{1/2}} \right) \\
&- \left. \tan^{-1}\left(\frac{(x-x_0)\,(y+y_0)}{(z-z_0)\left[(x-x_0)^2+(y+y_0)^2+(z-z_0)^2\right]^{1/2}} \right) \right\},
\end{aligned}
\tag{2.15}
$$

where ς is a normalization constant, Numerical solutions consider stress-free boundary conditions at the flat free surface, while at the rest of the boundaries no-slip conditions are satisfied. A spatial resolution of 220×170×22 was used in calculations with a time step of $1\times10^{-4}\ T_\omega$, where $T_\omega = 2\pi f$.

2.4 Results

In this section, we present experimental results and provide a comparison with analytical and numerical calculations. As mentioned in § 2.2, experimental observations correspond to four different flow planes, as shown in figure 2.1. All observations reported here were obtained once the effects of the initial conditions have died out. This required typically 10 cycles of the imposed electrical current oscillation. The reference value for the phase in the oscillation, φ=0, is taken at the point where the oscillatory external electric current is zero and increasing as a function of time. The maximum velocity attainable experimentally is $U = 1.28 \times 10^{-2}$ m-s^{-1}, that corresponds to an injected steady direct current of 70 mA (see figure 1.8). If this is taken as the velocity scale, the maximum Reynolds number based on the layer thickness, h, $Re_h = Uh/\nu$ is equal to $Re_h = 50$. Another relevant dimensionless parameter is the oscillation Reynolds number, $R_\omega = \omega h^2/\nu$, which estimates the ratio of the viscous time and the characteristic oscillation period. The four explored current frequencies, 10, 50, 100, and 200 mHz, correspond to values of R_ω equal to 1, 5, 10, and

20, respectively. In all cases, the larger velocity component lies along the symmetry $(y-z)$-plane that passes through the origin of coordinates and is oriented perpendicular to the direction of the imposed electric current (see figure 2.2).

For planes A, B, and C, the flow is practically unidirectional (pointing essentially in y-direction) during most of the cycle with alternating direction every half cycle. This is illustrated in figures 2.3(a-d) where the velocity field in the symmetry plane A is shown for $f = 100$ mHz ($R_\omega = 10$) at different phases. The reversal process is relatively fast, lasting approximately one fifth of the cycle and, with the available experimental resolution, no recirculation zones were detected. However, regions where the velocity almost vanishes are observed. In most of the initial half of the cycle *i.e.* $0 \leqslant \varphi \leqslant \pi$, the velocity field is similar to that shown in figure 2.3(a), with the fluid moving horizontally in the negative y-direction. At approximately $\varphi = 12/10\ \pi$ (figure 2.3(b)), the flow reverses its direction; the process starts near the bottom wall, developing a region with a wedge shape where the flow moves in the opposite direction, from left to right. In the transition region that lies between the two opposite running streams, the fluid has a very low velocity whose magnitude our experiment is unable to capture. At $\varphi = 13/10\ \pi$ (figure 2.3(c)), the right and left moving streams occupy approximately the same areas of our experimental window and eventually, at $\varphi = 14/10\ \pi$ most of the fluid runs to the right, completing the flow reversal (figure 2.3(d)). A similar transition process, but with opposite moving flows is observed at $1/10\ \pi \leqslant \varphi \leqslant 4/10\ \pi$. It is important to remark that even during the transition, the flow remains mainly horizontal with the vertical component w smaller than 4% of the horizontal v-component, which is the threshold of accuracy of our measurements. As will be shown below, numerical calculations confirm the general properties of the flow described above, as well as the quantitative agreement, within the experimental error, of the horizontal velocity component v at position ($x = 0$, $y = 0$). The maximum vertical velocity obtained with the numerical calculations is 1×10^{-4} m-s^{-1} and is located in the region corresponding to the low velocity of figure 2.3. Results obtained in this plane for all explored frequencies display the same qualitative features. In general, velocity fields in planes B and C basically present the behavior already described, for all the explored frequencies.

Figure 2.4 shows the profiles of the horizontal velocity component v as a function of the vertical z-coordinate for different phases in the cycle at point 1 ($x = 0$, $y = 0$), that is, along the midline of plane A. The first column displays the experimental observation, the plots on the second column are the results obtained with the numerical calculations and the third column contains the pro-

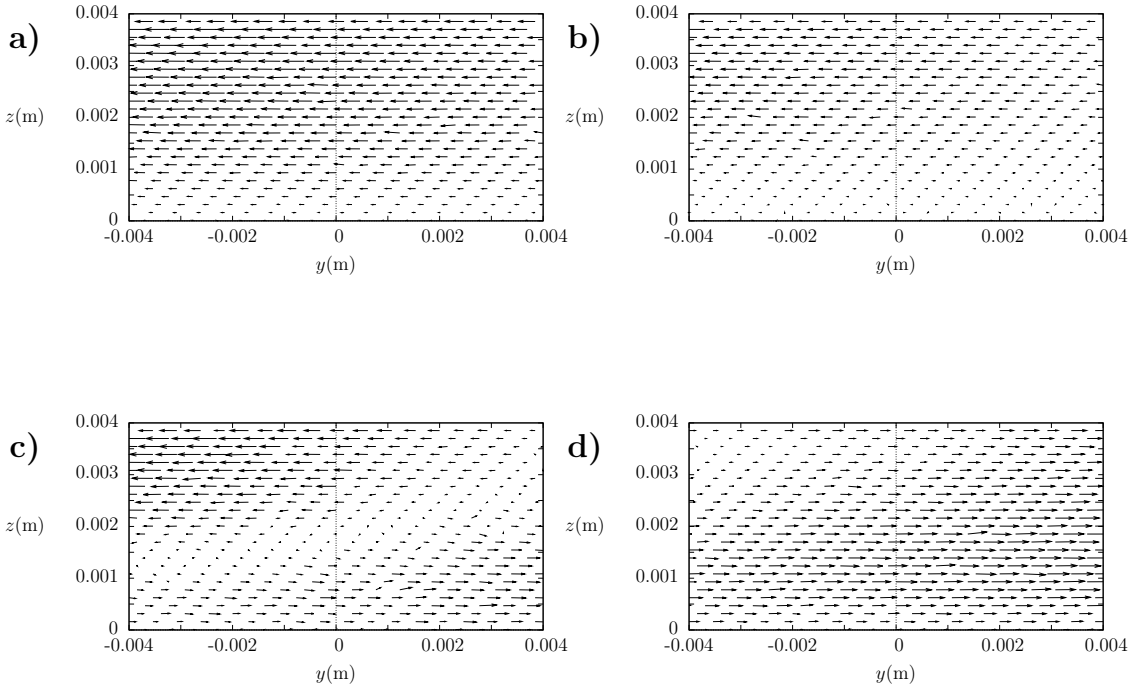

Figure 2.3: Experimental velocity field in a vertical plane passing through the center of the magnet ($x = 0$) and oriented perpendicular to the direction of the electric current (plane A in Fig. 2.1). Phases in different pictures are: a) $\varphi = \frac{11}{10}\pi$, b) $\varphi = \frac{12}{10}\pi$, c) $\varphi = \frac{13}{10}\pi$, d) $\varphi = \frac{14}{10}\pi$. Forcing frequency f=100 mHz (R_ω=10). For clarity, only half the number of vectors obtained in the y-direction is presented.

files according to the simple analytical model (equation 2.7). In fact, point 1 is where the assumptions made in the analytical model are better approached. The rows correspond to cases with R_ω =1, 5, 10, and 20, respectively. The profiles are clearly symmetric and it is observed that the amplitude of the horizontal velocity oscillation reduces as the frequency increases. Note also that, except for R_ω =20, the maximum velocity amplitude is reached at the free surface. The numerical solution reproduces the flow behavior qualitatively and quantitatively. The simplified analytical model captures qualitatively the oscillatory behavior of the flow in a small vicinity of the point of maximum magnetic field strength. However, the velocities calculated with equation (2.7) are approximately a factor of three larger than the experimental observation. This overestimation is attributed to the fact that the idealized analytical model considers a horizontal driving force which does not depend on the x and y-coordinates. In the experiment, this is not the case. Note that the qualitative agreement is better for higher frequencies (R_ω =10 and 20). As the frequency decreases, the analytical solution predicts velocity amplitudes larger than those observed in the numerical and experimental profiles. In fact, for the latter profiles the maximum velocity amplitude seems to saturate as the frequency decreases. According to solution (2.8) for a semi-infinite fluid region, the horizontal velocity is damped vertically due to both the magnetic field decay and viscous dissipation. In the analyzed cases, $0.17 \leqslant \gamma\delta \leqslant 0.78$ and therefore, the damping and the characteristic thickness of the oscillatory boundary layer is determined by viscous effects. In this case, the amplitude in the analytical solution becomes inversely proportional to the frequency (see equation (2.9)) so that it is unbounded as $\omega \to 0$.

The experimental and numerical velocity profiles at ($x = -d/4$, $y = 0$) in plane B (point 2 in figure 2.1), where d is the magnet diameter, are shown in figure 2.5. The left column displays the experimental results, the right column shows the results of numerical computations and, as in figure 2.4, the rows correspond to the four different explored frequencies. The profiles are symmetric and very similar to those at point ($x = 0$, $y = 0$) although due to the decrease of the magnetic field strength, velocity amplitudes are roughly half the value at central point 1.

Figure 2.6 shows the velocity profiles at point 3 of plane C (see figure 2.1), that is, ($x = 0$, $y = -d/2$), where the magnetic field inhomogeneity is more pronounced. In this case, the first and second columns correspond, respectively, to the experimental and numerical velocity profiles for the horizontal v component. The third column shows the numerical profiles of the vertical w component. The magnitude of this component is too small to be captured with the experimental

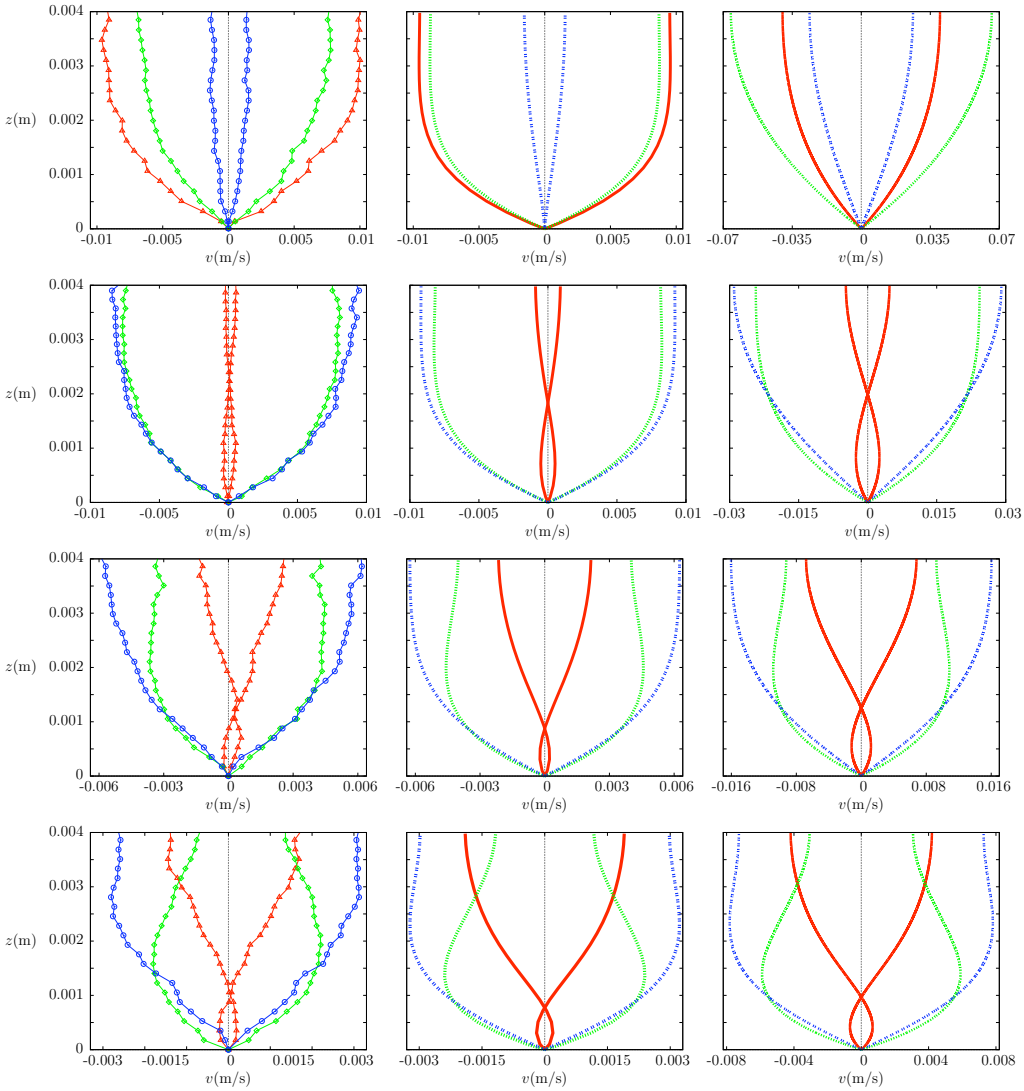

Figure 2.4: Profiles of the horizontal velocity component v as functions of the vertical z-coordinate at (x =0, y =0) which corresponds to point 1 in Fig. 2.1. Left column, experimental observations. Central column, numerical calculations. Right column, velocity distributions according to Eq. (2.7). First row, $f = 10$ mHz (R_ω=1), second row, $f = 50$ mHz (R_ω=5), third row, $f = 100$ mHz (R_ω=10), fourth row, $f = 200$ mHz (R_ω=20). Symbols and lines donote experimental data and theoretical predictions, respectively. In all cases, the phases displayed are $\varphi = \frac{1}{3}\pi$ & $\varphi = \frac{4}{3}\pi$ (in red: triangles and continuos lines), $\varphi = \frac{2}{3}\pi$ & $\varphi = \frac{5}{3}\pi$ (in green: rhombs and dotted lines) and $\varphi = \frac{3}{3}\pi$ & $\varphi = \frac{6}{3}\pi$ (in blue: circles and dahed lines).

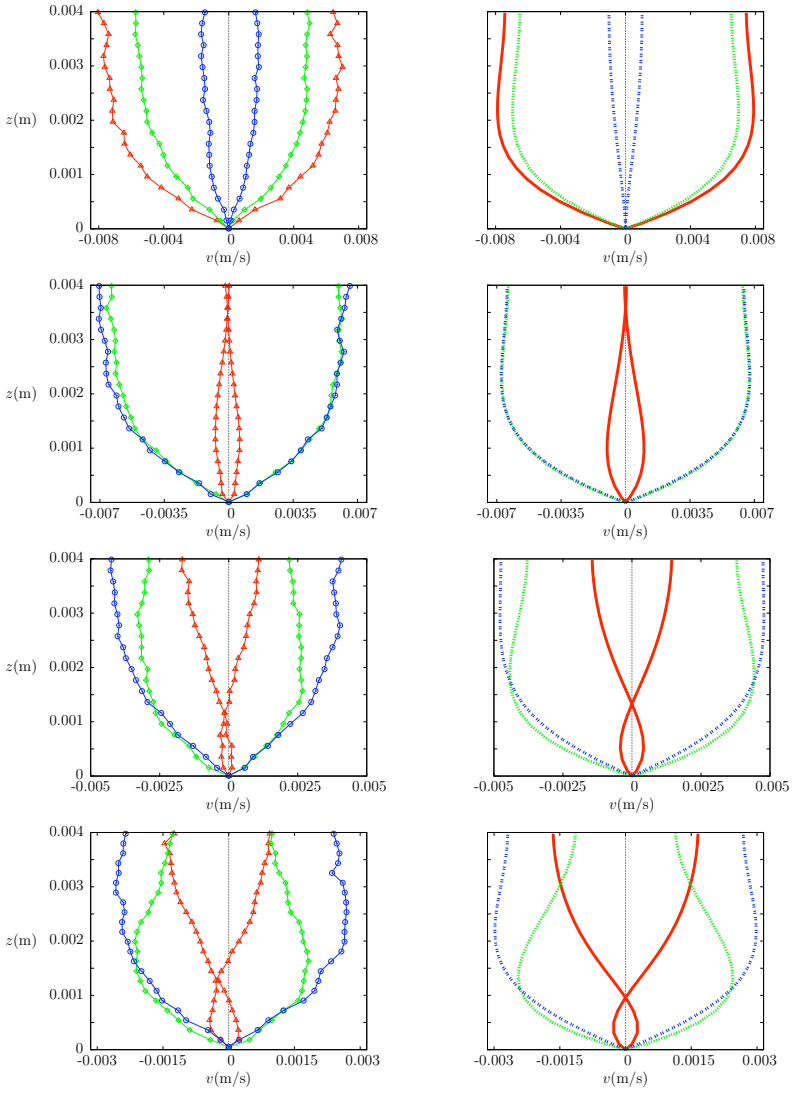

Figure 2.5: Profiles of the horizontal velocity component v as functions of the vertical z-coordinate at ($x = -d/4$, y =0) which corresponds to point 2 in Fig. 2.1. Left column, experimental observations. Right column, numerical calculations. First row, $f = 10$ mHz (R_ω=1), second row, $f = 50$ mHz (R_ω=5), third row, $f = 100$ mHz (R_ω=10), fourth row, $f = 200$ mHz (R_ω=20). Symbols and lines donote experimental data and theoretical predictions, respectively. In all cases, the phases displayed are $\varphi = \frac{1}{3}\pi$ & $\varphi = \frac{4}{3}\pi$ (in red: triangles and continuos lines), $\varphi = \frac{2}{3}\pi$ & $\varphi = \frac{5}{3}\pi$ (in green: rhombs and dotted lines) and $\varphi = \frac{3}{3}\pi$ & $\varphi = \frac{6}{3}\pi$ (in blue: circles and dahed lines).

device. A reasonable agreement between the numerical and experimental results for the v component is found for low frequencies. At high frequencies (100 and 200 mHz) the dispersion is considerable due to limitations of our experimental equipment. In these cases we could only capture five cycles to implement the averaging procedure leading to poor signal to noise ratio. Clearly, five cycles is not enough to smooth out the noise. A third order polynomial fit has been drawn to guide the eye. Again, it is found that maximum amplitudes are mainly reached at the free surface. The local asymmetry in the profiles at the corresponding phases is due to inertial effects. As it was also observed in the electromagnetically driven vortex flow with a direct current (Chapter 1), the maximum velocity not necessarily occurs at the point of maximum magnetic field strength but downstream. Note that the maximum negative velocities at point 3 for frequencies 10 and 50 mHz are larger than the corresponding ones at point 1. Since the magnetic field is rather weak at the edge, inertial effects are more important than the nonuniformity of the field in this region. Given the cyclic symmetry expressed by conditions (2.2), corresponding profiles will be found at the oposite edge of the magnet after half cycle. The numerical results for the w component show the effects of the magnetic field inhomogeneity which creates a force in the vertical direction. However, the maximum magnitude of the w component created by this force is again smaller than 4% of the horizontal v-component.

As already mentioned, the flow in planes A, B, and C is essentially unidirectional, the magnitude of the velocity component v being substantially larger than the vertical component w. Likewise, the mass entrainment across planes A and C is practically zero while it is negligibly small across plane B. This situation changes drastically in plane D where the three velocity components seem to have approximately the same magnitude. However, this magnitude is smaller than the experimental resolution and a clear velocity field in this region is not available with the present experimental equipment. Instead, we present results from the numerical simulation in order to provide a picture of the flow structure in plane D. Figure 2.7 shows the velocity field in this plane for $R_\omega = 10$ at different phases of the cycle. In this case, the mesh used in the numerical calculation was refined to $1320 \times 1020 \times 40$ and the domain was reduced to the window observed in the experiments. Clearly the flow is not unidirectional, and at some phases the vertical component appears to be comparable with the horizontal one.

Figure 2.8 shows the velocity profiles of components v (left column) and w (right column) at point 4 ($x = -d/2$, $y = 0$) at different phases in the cycle for the four explored frequencies. It is interesting to observe that the maximum amplitude of v is not reached at the free surface but rather close to the bottom

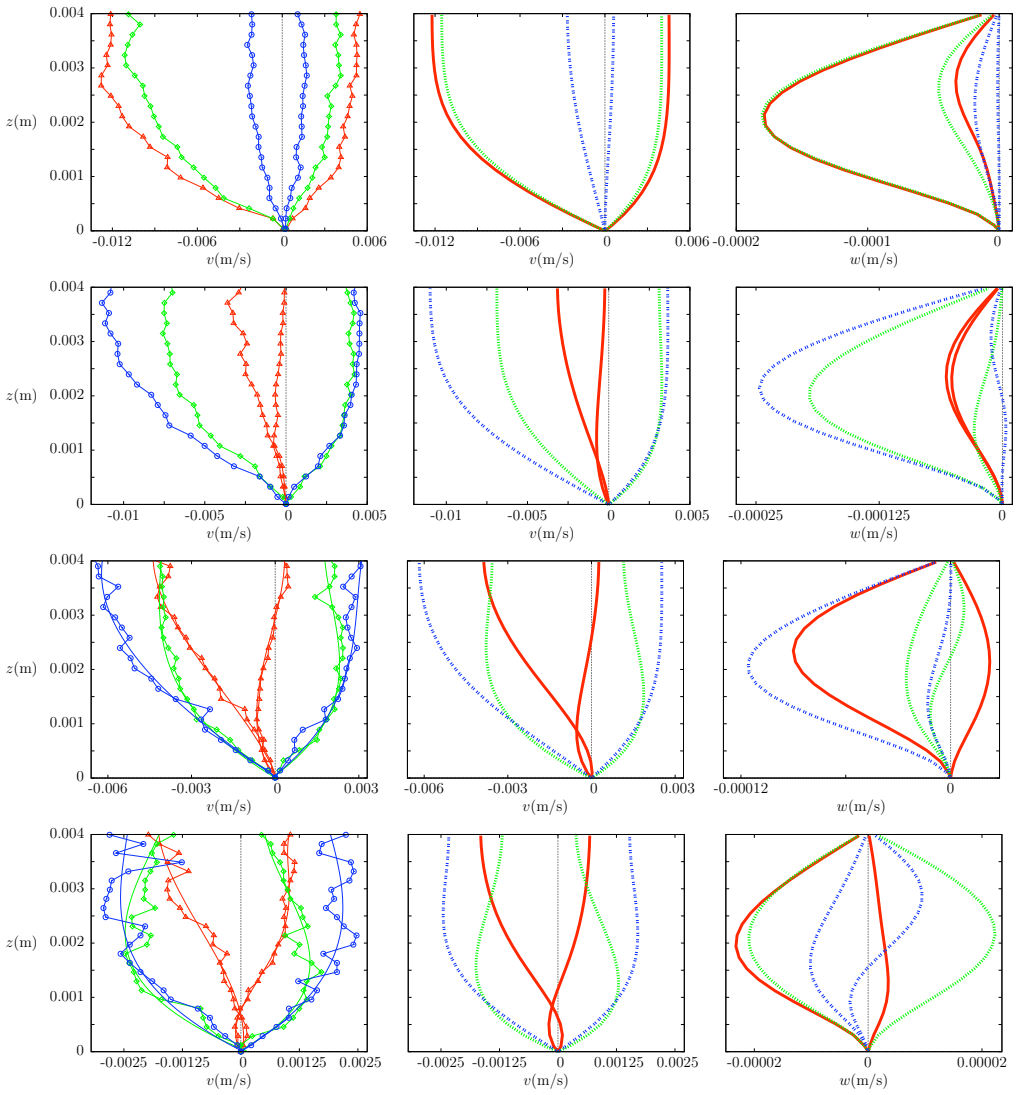

Figure 2.6: Velocity profiles as functions of the vertical z-coordinate at ($x = 0$, $y = -d/2$) which corresponds to point 3 in Fig. 2.1. Left column, experimental observations of v horizontal component. Central column, numerical calculations of v component. Right column, numerical calculation of vertical w component. First row, $f = 10$ mHz (R_ω=1), second row, $f = 50$ mHz (R_ω=5), third row, $f = 100$ mHz (R_ω=10), fourth row, $f = 200$ mHz (R_ω=20). Symbols and lines donote experimental data and theoretical predictions, respectively. In all cases, the phases displayed are $\varphi = \frac{1}{3}\pi$ & $\varphi = \frac{4}{3}\pi$ (in red: triangles and continuos lines), $\varphi = \frac{2}{3}\pi$ & $\varphi = \frac{5}{3}\pi$ (in green: rhombs and dotted lines) and $\varphi = \frac{3}{3}\pi$ & $\varphi = \frac{6}{3}\pi$ (in blue: circles and dahed lines). The lines in the third and fourth rows of the first column are polynomial fits.

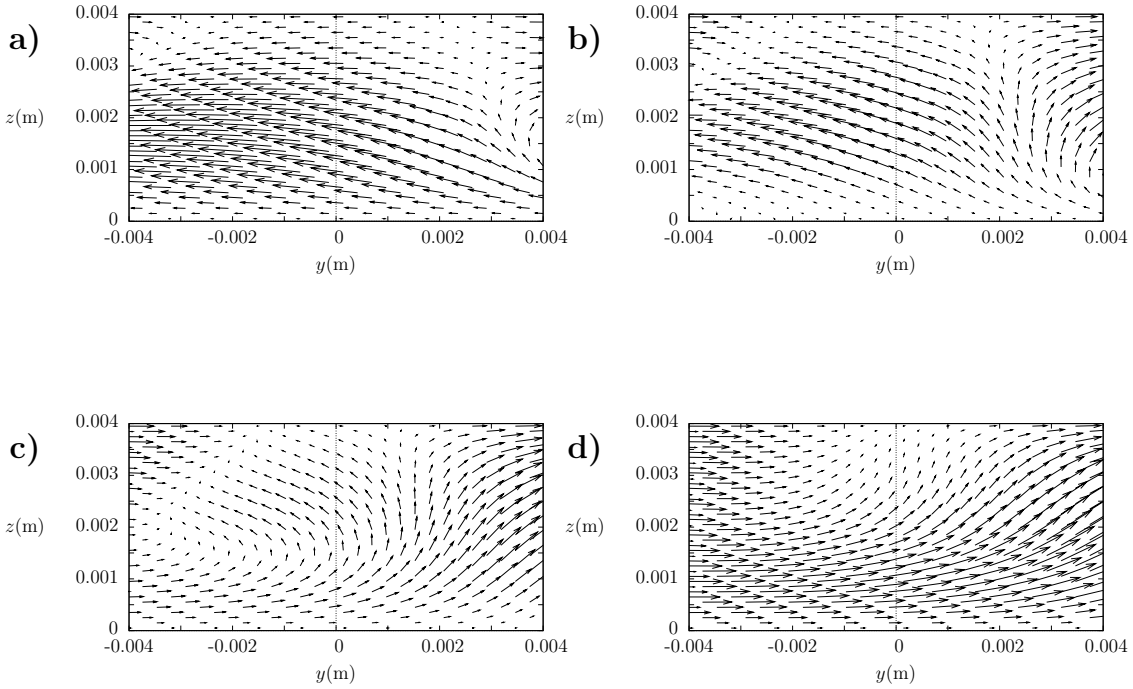

Figure 2.7: Numerically calculated velocity field in plane D ($x = -d/2$), see Fig. 2.1. Phases in different pictures are: a) $\varphi = \frac{11}{10}\pi$, b) $\varphi = \frac{12}{10}\pi$, c) $\varphi = \frac{13}{10}\pi$, d) $\varphi = \frac{14}{10}\pi$. Forcing frequency f=100 mHz (R_ω=10). For clarity, only half the number of vectors obtained in the y-direction is presented.

wall while that of w is reached at the mid layer position. Note also that the maximum amplitude of component v is four to ten times larger than that of w. However, the magnitude of component v is at least one order of magnitude smaller than the corresponding one in point 1.

2.5 Discussion

In this Chapter, the laminar flow generated in a thin electrolyte layer by the oscillatory Lorentz force produced by the interaction of a localized magnetic field and an imposed alternate electric current, has been studied with theoretical and experimental tools. The investigated region embraces mainly the extent of the magnet where the flow is more intense. The analysis was focused on exploring the structure of the induced oscillatory boundary layer in planes perpendicular to both the bottom wall and the injected current. The maximum Reynolds number of the flow based on the layer depth was $Re_h = 50$. PIV measurements were complemented with 3D numerical simulations to provide velocity fields in different planes, as well as velocity profiles as a function of the normal coordinate at characteristic points. In addition, a simple analytical model that approximately reproduces the behavoir of the Stokes-like oscillatory layer in the zone of maximum magnetic field strength, was derived. It has been observed that in contrast to the classical Stokes layer, the change in the direction of motion takes place as an advancing front which is tilted with respect to the horizontal lower wall. An emphasis was put in the search of three-dimensional structures formed as a result of the cycling forcing. Under the considered experimental conditions, it is possible to conclude that the flow is mostly Q2D in the planes A, B, and C (see figure 1), with regions where small vertical velocities are present at the phases in the cycle where flows with opposite directions meet, as illustrated in figure 2.3. Unfortunately, due to the smallness of the magnitude of the vertical velocity in these regions, our experimental equipment is unable to give reliable data. In plane D, located above the lateral edge of the magnet, we found that the magnitude of all velocity components is smaller than our experimental resolution. This result was confirmed by numerical calculations which also indicate that 3D structures do exist in this region.

To the best of our knowledge, there is no other available study on the 3D characteristics of shallow flows driven by oscillatory electromagnetic forces. Nevertheless, it is interesting to contrast our results and conditions with reported works on electromagnetically driven flows. For instance, in the unsteady inertial

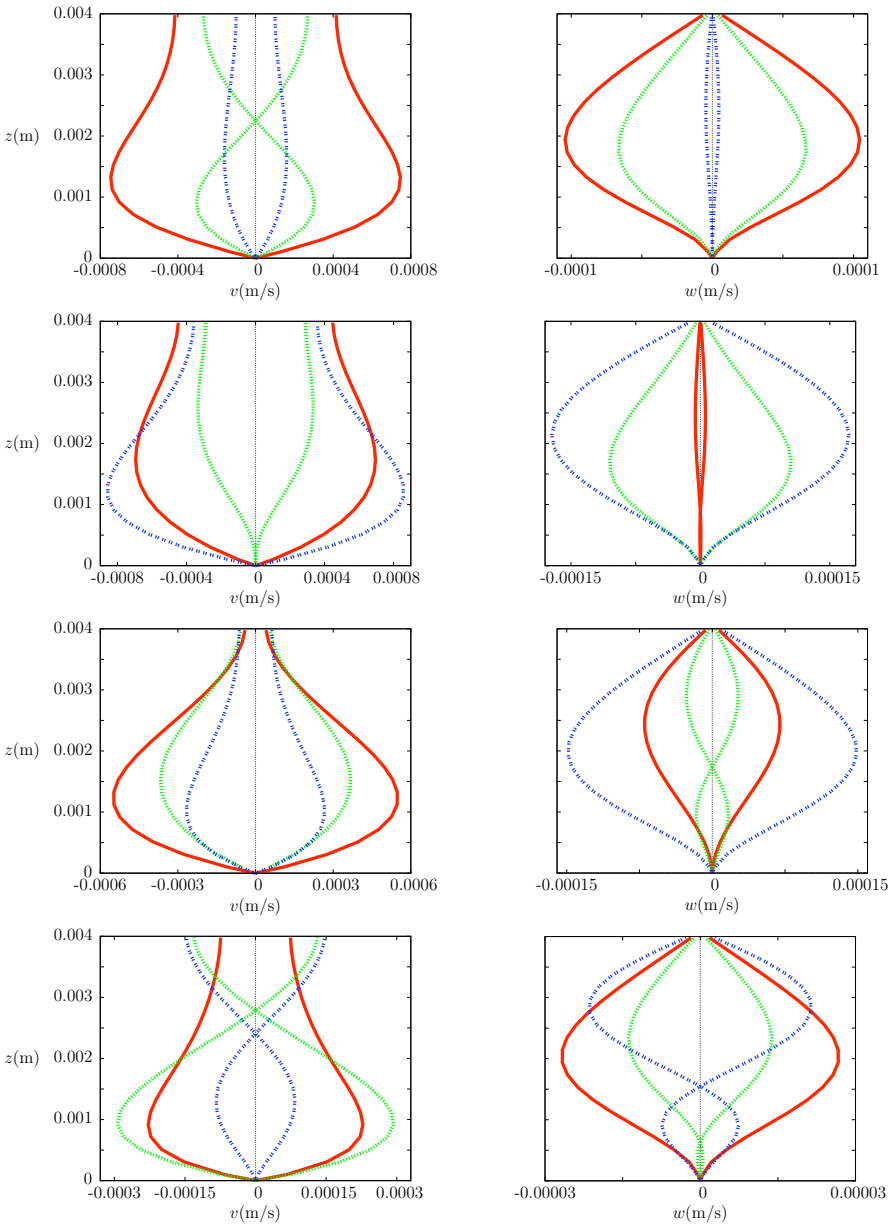

Figure 2.8: Numerically calculated velocity profiles as function of the vertical z-coordinate at ($x = -d/2$, y =0) which corresponds to point 4 in Fig. 2.1. Left column, velocity profiles of horizontal component v. Right column, velocity profiles of vertical component w. First row, $f = 10$ mHz (R_ω=1), second row, $f = 50$ mHz (R_ω=5), third row, $f = 100$ mHz (R_ω=10), fourth row, $f = 200$ mHz (R_ω=20). Symbols and lines donote experimental data and theoretical predictions, respectively. In all cases, the phases displayed are $\varphi = \frac{1}{3}\pi$ & $\varphi = \frac{4}{3}\pi$ (in red: triangles and continuos lines), $\varphi = \frac{2}{3}\pi$ & $\varphi = \frac{5}{3}\pi$ (in green: rhombs and dotted lines) and $\varphi = \frac{3}{3}\pi$ & $\varphi = \frac{6}{3}\pi$ (in blue: circles and dahed lines).

vortex dipole reported by Akkermans *et al.* (2008a; 2008b), the flow is generated by a current pulse in a localized magnetic field that leads to a maximum forcing term $|\mathbf{j} \times \mathbf{B}/\rho|$ of 0.88 m-s^{-2}. The resulting ratio of vertical to horizontal kinetic energies is $q = E_v/E_h = 0.08$ while the characteristic Reynolds number is $Re_h = 520$. In contrast, our flow is generated by an oscillatory Lorentz force with a maximum forcing term $|\mathbf{j} \times \mathbf{B}/\rho|$= 0.02 m-s^{-2} leading to $q = E_v/E_h = 0.0002$ while $Re_h = 50$. These differences may account for the fact that while in the experiments by Akkermans *et al.* intrinsic three-dimensionality was found in the flow, in the present study 3D structures appear mainly in the neighborhood of the lateral edge of the magnet (plane D in figure 1) while a Q2D behavior was found in the other analyzed regions. Our numerical results indicate that vertical velocities do exist in the flow, but they are too small to be measured with our present experimental technique.

Rossi and colleagues have made experimental observations and numerical simulations of flows driven my multiscale electromagnetic forcing (Lardeau *et al.* 2008). Although there are many differences in the geometrical and physical conditions between their analysis and ours, some common features of the flows are worth discussing. They emphasize that in order to correctly modeling the flow, it is necessary to take into account the vertical variation of the magneic field, and consequently, of the Lorentz force (Lardeau *et al.* 2008). This feature is definitely borne out by the analysis reported here. They also point out that a 3D model of the flow is required for accurately reflecting the experimental observations, and this conclusion is reached by comparing information from horizontal velocity fields. They mention, however, that in the whole range of forcing intensities considered, the ratio of the magnitudes of the vertical to the horizontal velocity components is very small, varing between 0.35% and 0.84%. Therefore, compared with the mean energy in the horizontal direction, the mean energy in the wall-normal direction can be considered negligible and the flow, in this sense, is Q2D. This observation is coincident with our own measurements and numerical results.

Although the dipolar vortex owes its characteristic structure to the inhomogeneity and localization of the magnetic field, locally the field gradients in the horizontal plane seem to have a less pronounced effect than the vertical gradient. Our results show a clear effect of the magnetic field inhomogeneity in the vertical direction. In fact, the decay of the field influences the form of the vertical velocity profiles since the driving force diminishes with the increase in the vertical distance from the magnet, as was also found in the analysis of a steady vortex dipole (Figueroa *et al.* 2009). Incidentally, Akkermans *et al.* (2008a),

reported that the vertical structure of the flow does not relax to a Poiseuille-like flow. On the other hand, the inhomogeneity of the field in horizontal planes is more pronounced around the edge of the magnet and creates a vertical force that promotes flow three-dimensionality. However, in plane C (see figure 2.1), along the y-direction which coincides with the main direction of the horizontal force, the vertical force seems to be overcome by inertial effects. In turn, at the lateral edge of the magnet (plane D) the vertical force along with the mass entrainment, appear to promote noticeable 3D effects though flow strength is rather low.

In the context of elucidating the importance of three-dimensionality in the oscillating flow under the explored conditions, our general conclusion is that although vertical motion and consequently 3D structures were detected in our experiment, owing to their relative small magnitude, the flow presents a Q2D behavior.

Chapter 3

Dynamics of oscillatory vortex flows in multipolar magnetic fields

In this Chapter[1], vortices formed by the concurrent effect on a localized magnetic field and an externally imposed, oscillatory electric current in a shallow (4mm) layer of an electrolyte are experimentally analyzed. Alternate currents with frequencies in the range of 1-500 mHz and amplitude of 80 mA, are explored. Horizontal velocity fields were obtained using Particle Image Velocimetry. For a single dipolar magnetic field and a single electric current, the dominant structure of the flow is an oscillating dipole vortex, composed by a pair of alternating lobes located co-linear with the generated Lorenz force. The flow presents a resonant behavior when the forcing frequency is around 10 mHz. When multipoles are used to generate the magnetic field distribution more complicated vortical flows composed by sets of syncronous alternating lobes are obtained. When two antiparallel magnetic dipoles are close enough, a tripole-like structure is found. The flow patterns were successfully described using a quasi-two-dimensional numerical model. A three-dimensional numerical integration of the conservation equations models corroborates the theoretical results obtained with the simpler model.

[1]This Chapter is mainly based on the paper: Figueroa, A., Cuevas, S. & Ramos, E., 2010, "Dynamics of oscillatory vortex multipoles". In preparation.

3.1 Introduction

Vortical flows generated by the injection of electric currents in a thin layer under a non-uniform magnetic field produced by an array of permanent magnets have been studied as models for two-dimensional turbulence decaying (Cardoso *et al.* 1994; Clercx *et al.* 2002). These electromagnetically driven flows have also been studied with other applications in mind since they present similarities with those found in atmospheric and oceanic and flows, such as tidal jets in bays and estuaries (Fujiwara *et al.* 1992), where nutrient (Wolansky *et al.* 1988) and particle transport (Brown *et al.* 2000) are of great importance. For shallow layers, steady flows and small driving forces, the motion can be described in terms of a two-dimensional core flow with a linear friction that accounts for the effects of the boundary layers, since the small depth of the layer as compared with its horizontal extension ensures the quasi-two-dimensionality (Q2D) of the flow. A usual approach consists of considering a Rayleigh friction to model the bottom wall-normal friction in the form $-\alpha \boldsymbol{u}$, where $\boldsymbol{u}$ is the velocity field and α is a constant friction coefficient. Several studies have been performed to clarify the degree to which these flows are Q2D. In decaying vortex flows initially promoted by electromagnetic forces, Paret *et al.* (1997) determined the time constant associated with the transfer of momentum across the layer, after comparing it with the characteristic time for the decay of energy, these authors stated that after a small transitory time these flows are two-dimensional (2D). Satijn *et al.* (2001) established that since the no-slip boundary implies a vertical shear which leads to secondary circulations within the planar vortices, these flows necessarily possess a three-dimensional structure. Lardeau *et al.* (2008) analyzed using three-dimensional (3D) numerical simulations a multiscale flow with turbulent-like properties, and concluded that even if the flow is Q2D in terms of enegy, a full 3D approach is required to simulate these shallow layer flows. Akkermans *et al.* (2008a, 2008b) studied a dipolar vortex in an electrolytic layer of 9.3 mm thickness created by a single one second current pulse of 4.4 A interacting with the nonuniform field of a disk-shaped magnet. They found that vertical motion occurs throught the flow evolution, during and after the forcing phase so that they cannot be quantified as Q2D. In turn, Figueroa *et al.* (2009) analyzed a steady dipolar vortex flow continuously driven by the interaction of a 5-100 mA dc uniform electric current and the magnetic field produced by a small dipolar permanent magnet in an electrolytic layer of 4 mm thickness. A Q2D model was succesfully compared with experimental velocity profiles in planes parallel and normal to the bottom wall, in the neighbourhood of the zone influenced by the

magnetic field. They found that the boundary layer attached to the bottom wall shows a slightly flattened developing Poiseuille profile. It was demonstrated that the flattening of the profile is due to the variation of the magnetic field in the normal direction. In Chapter 2, the oscillating dipolar vortex flow generated by a sinusoidal electric current was studied. It was observed that, anagously to the problem of the flow attached to a bottom wall produced by an oscillating free stream (Panton 2005), in the central part of the magnet, the velocity profile in the normal direction behaves as a Stokes-like velocity profile. It was also showed that even for a time dependent flow, small recirculations are present but in the vecinity of the magnet, where velocity components are at least one order of magnitude smaller than components in the central region, so that flow behaves as Q2D.

In this Chapter, the flow created in a thin layer of an electrolytic fluid by the interaction of an alternate electric current and different arrays of dipolar magnets is studied both experimentally and theoretically. We observed that the dominant flow pattern is an alternate two-lobe dipole vortex which is suitably represented with a quasi-two-dimensional (Q2D) numerical model that contains the main physical ingredients of the electromagnetically forced laminar flows in shallow layers. The model incorporates a bottom wall friction obtained with a Stokes-like analytic solution that reproduces qualitatively the velocity profiles in the vicinity of the point of maximum magnetic field strength (see Chapter 2 for details). The Q2D model appears to be particularly suited for the analysis of electromagnetically driven flows in shallow electrolytic layers, since the comparison of the numerical and experimental velocity profiles shows a good quantitative agreement. The results are complemented with 3D numerical simulations that present, in general, a fairly good agreement with experiments. Three-dimensionality of the different flows depending on the magnet array is quantified with a kinetic energy analysis.

3.2 Experimental procedure

Only a brief account of the experimental setup used in these experiments will be given, since more detailed descriptions have already been given in § 1.2 and § 2.2. Oscillatory electric currents with frequencies ranging from 1 to 500 mHz were injected through the electrodes and the amplitude of the electric current was 80 mA. Experiments were performed with two permanent magnets. In the first set of experiments, the magnet is cylindrical with a diameter of 19 mm, height of 5 mm

and maximum strength of 0.33 T. In the second set, the magnet is a rectangular parallelepiped with a side length of 25.4 mm, height of 12.7 mm and maximum strength of 0.38 T. Quantitative measurements of the horizontal velocity field on the flow plane at a distance from the bottom wall of 3.5 mm (z=3.5 mm) were obtained with a Particle Image Velocimetry system (Dantec FlowMap PIV1100). We recorded 20 velocity fields per cycle with a spatial resolution of 2.24 mm. A minimum of 5 cycles were averaged, for each reported data set.

3.3 Theoretical model

Weak electrolite flows electromagnetically driven can be mathematically modeled through the continuity equation (2.3) and the Navier-Stokes equations (2.4) with the Lorentz force as source term. The last term on the right-hand side of equation (2.4) considers the oscillating Lorentz force created by the three-dimensional magnetic field distribution $\boldsymbol{B}^0 = \boldsymbol{B}^0(x, y, z)$ and the sinusoidal injected electrical current distribution, $\boldsymbol{j}^0 = j^0 \sin(\omega t)\, \hat{\boldsymbol{x}}$, where $\omega = 2\pi f$ is the angular frequency, and f is the ordinary frequency.

Following the averaging approach and the dimensionless variables presented in Chapter 1 for the analysis of the dipole vortex shallow flow where the stationary classic viscous boundary layers is considered, we assume that the transport of momentum in the normal direction is mainly diffusive, so that the dimensionless velocity components in the $(x - y)$ plane can be expressed as

$$u(x, y, z, t) = \bar{u}(x, y, t)\, \hat{f}(z, t), \qquad v(x, y, z, t) = \bar{v}(x, y, t)\, \hat{f}(z, t), \tag{3.1}$$

where time t is normalized by ω. We also assume that the only non-negligible component of the magnetic field is the normal one B_z^0 (straight magnetic field approximation (Alboussière 2004)). For the permanent magnets used in the experiments, the normal dimensionless magnetic field component were reproduced analytically through the expression (1.7). In turn, for the function $g(z)$ in equation (1.7), γ=2.53 and 2.16 was obtained by experimental fitting for cylindrical and squared shaped magnets, respectively. Dropping the overline, the averaged quasi-two-dimensional system of equations read

$$\frac{\partial u}{\partial x} + \frac{\partial v}{\partial y} = 0, \tag{3.2}$$

$$R_\omega \frac{\partial u}{\partial t} + \left(u\frac{\partial u}{\partial x} + v\frac{\partial u}{\partial y} \right) = -\frac{\partial P}{\partial x} + \nabla_\perp^2 u - \frac{u}{\tau} \tag{3.3}$$

$$R_\omega \frac{\partial v}{\partial t} + \left(u\frac{\partial v}{\partial x} + v\frac{\partial v}{\partial y} \right) = -\frac{\partial P}{\partial y} + \nabla_\perp^2 v - \frac{v}{\tau} - \alpha Re_* \mathcal{B}_z^0 \sin(t), \tag{3.4}$$

where the parameters $Re_* = U_0 L/\nu$ and $R_\omega = \omega L^2/\nu$, stand for the Reynolds and oscillation Reynolds numbers, respectively. The characteristic bulk velocity U_0 is obtained from a balance between viscous and Lorentz forces, see § 1.3.1. The Rayleigh friction term in equations (3.3) and (3.4) involves a characteristic time scale, τ for the damping of vorticity due dissipation in the viscous layers (eq. (1.15)). In order to obtain the friction term we must first calculate the function $\hat{f}$, which should reproduce the velocity profile in the normal direction. The Stokes velocity profile in equation (2.7) is used as a explicit form of function $\hat{f}$. Once it is normalized with condition $\int_0^\varepsilon \hat{f} dz = 1$, function $\hat{f}$ takes the form

$$\hat{f} = \Re \left\{ \frac{\sqrt{a\epsilon^2}\cosh\left(\sqrt{a\epsilon^2}(z-\epsilon)\right) - \gamma\epsilon e^{-\gamma\epsilon^2}\sinh\left(\sqrt{a\epsilon^2}z\right) - \sqrt{a\epsilon^2}e^{-\gamma\epsilon z}\cosh\left(\sqrt{a}\epsilon^2\right)}{\sinh\left(\sqrt{a}\epsilon^2\right) - \frac{\gamma e^{-\gamma\epsilon^2}}{\sqrt{a}}\left(\cosh\left(\sqrt{a}\epsilon^2\right) - 1\right) + \frac{\sqrt{a}}{\gamma}\cosh\left(\sqrt{a}\epsilon^2\right)\left(e^{-\gamma\epsilon^2} - 1\right)} \right\}, \tag{3.5}$$

where $a = iR_\omega$, and $\Re$ indicates the real part of the expression inside the brackets. Using equation (1.15), the friction parameter can be calculated as

$$\tau^{-1} = \Re \left\{ \frac{a\sinh\left(\sqrt{a}\epsilon^2\right) + \sqrt{a}\gamma\left(e^{-\gamma\epsilon^2} - \cosh\left(\sqrt{a}\epsilon^2\right)\right)}{\sinh\left(\sqrt{a}\epsilon^2\right) - \frac{\gamma e^{-\gamma\epsilon^2}}{\sqrt{a}}\left(\cosh\left(\sqrt{a}\epsilon^2\right) - 1\right) + \frac{\sqrt{a}}{\gamma}\cosh\left(\sqrt{a}\epsilon^2\right)\left(e^{-\gamma\epsilon^2} - 1\right)} \right\}. \tag{3.6}$$

Further, due to the variation of the magnetic field in the normal direction, the Lorentz force term in equation (3.4) includes the factor α given by equation (1.16). According to the shallow flow approximation, ε is assumed to be less than unity. In the experiment, the maximum value of ε, obtained at the free surface for the cylindrical magnet is 0.21.

The system of equations (3.2)-(3.4), along with the friction model, equation (3.6), the factor α (eq. (1.16)) and the bidimensional distribution of the magnetic field ($\mathcal{B}_z^0(x,y)$), was solved numerically using a finite difference method based on the procedure described in Chapter 1. The velocity components satisfy non-slip conditions at the boundaries of the container. Aditionally to the quasi-two-dimenional model, the full three-dimensional system of equations (2.10-2.13)

was solved using a numerical algorithm also based in the projection technique (Griebel *et al.* 1998). The three-dimensional numerical solutions consider the full magnetic field from the dipolar magnets and stress-free boundary conditions at the flat free surface, while at the rest of the boundaries no-slip conditions are satisfied. The quasi-two and three dimensional models were solved in a rectangular domain corresponding to the dimensions of the experimental setup.

3.4 Results

3.4.1 Flow analysis

In order to describe the properties of the flow, we make use of the identification of special points in the velocity fields with the methodology presented by Ouellette $\&$ Gollub (2007). The nature of the critical points is discerned through the Okubo-Weiss (OW) criterion in two dimensions (Weiss 1991). When the OW parameter is positive, the region is dominated by rotation, identifying elliptical points. In contrast, if OW parameter is negative, local deformation dominates, indicating that the critical point is hyperbolic.

Oscillating dipole vortex

When a single magnet is used, the flow promoted by the alternate Lorentz force consist of a central jet that generates two counter-rotating vortices that oscillate in the y-direction, namely, the oscillating dipole vortex (see Chapter 2). Figure 3.1 shows four snapshots representing the dynamics of a half cycle of the experimental velocity field of the oscillating dipole vortex with a forcing frequency f=50 mHz. The reference value for the phase in the oscillation, φ=0, is taken at the point where the oscillatory external electric current is zero and increasing as a function of time. The Lorentz force generates a dipole vortex with the main stream pointing in the negative y-direction, figure 3.1(a). As the force is increased with time, the centers of the vortical regions as well as the location of maximum velocity (denoted by the symbol $\bullet$) are convected in the direction of the main Lorentz force, elongating the vortices, see figures 3.1(b)-3.1(c). When the Lorentz force is reduced, after $\varphi = \pi/2$, the vortices dissipate reducing the flow velocity and elongating further, figure 3.1(d). Finally, the Lorentz force is inverted, generating a pair of vortices in the opposite direction while the vortices generated in the previous half cycle move away from the magnet and dissipate.

Along with the vector velocity field, in figure 3.1 we can observe the dynamics of the critical points and the instantaneous maximum velocity of the flow. Every half cycle, two elliptical points (asteriscs $*$) are generated each at the center of a vortex. Up to four elliptical points can be identified in the area displayed at any given time. The hyperbolic point (cross $\times$) is located at the vertical mid-line that separates the vortices that rotate in opposite directions. The instantaneous maximum velocity point moves along the y-axis close to the central line joining the centers of the stronger dipole vortex. Note that the points of instantaneous maximum velocity are generated alternatively every half cycle on the upper and lower half of the (x,y) region analyzed.

Figure 3.2(a) shows the instantaneous maximum velocity v_{max} as a function of time during a cycle of the applied Lorenzt force. Experimental data are represented by circles ($\odot$) and Q2D and 3D theoretical predictions are represented by continuous and dashed lines, respectively. As expected, the instantaneous maximum velocity displays a periodic bahavior but the graph is composed of disjoint segments since the points of maximum velocity arise at locations different from where they disappear. As can be appreciated from the figure, the fit of Q2D and 3D models is very good for the location of maximum velocity points. Figure 3.2(b) shows the absolute amplitude of the maximum velocity signal $\mid v_{max} \mid$ as a function of the forcing frequency f. For large frequencies, the amplitude of the maximum velocity signal decreases when f is increased. As $f \rightarrow 0$, the amplitude $\mid v_{max} \mid \rightarrow 1.38 \times 10^{-2}$ m-s^{-1}, which is the corresponding velocity of an injected steady direct current of 80 mA (see figure 1.8). The amplitude of maximum velocity signal shows resonant response around $f \simeq 10$mHz, which was unexpected. Both models show a good agreement with experiments, but the Q2D model predicts a value which is 10$\%$ smaller than the experimental. It is remarkable that the Q2D model reproduce the resonant behavior, implying that at least it is not entirely a 3D effect.

The general features of the velocity field are more clearly observed in figures 3.3(a–d), where the velocity component v is plotted as function of position for forcing frequency $f = 50$ mHz at two phases. In figures 3.3(a) and 3.3(b) velocity component v is plotted as a function of x coordinate at y=0 ($v(x, 0)$), while 3.3(c) and 3.3(d) v is plotted as a function of y coordinate at x=0 ($v(0, y)$). The left column in figure 3.3 shows the comparison between the experimental and the profiles provided by the Q2D model, while right column compares the 3D model profiles. Each figure contains two time phases, diamond $\diamond$ and continuous line: $\varphi = 2/10\ \pi$; circle $\odot$ and dashed line: $\varphi = 4/10\ \pi$. The velocity distribution $v(x, 0)$ is nearly symmetric, but the velocity profile $v(0, y)$ shows

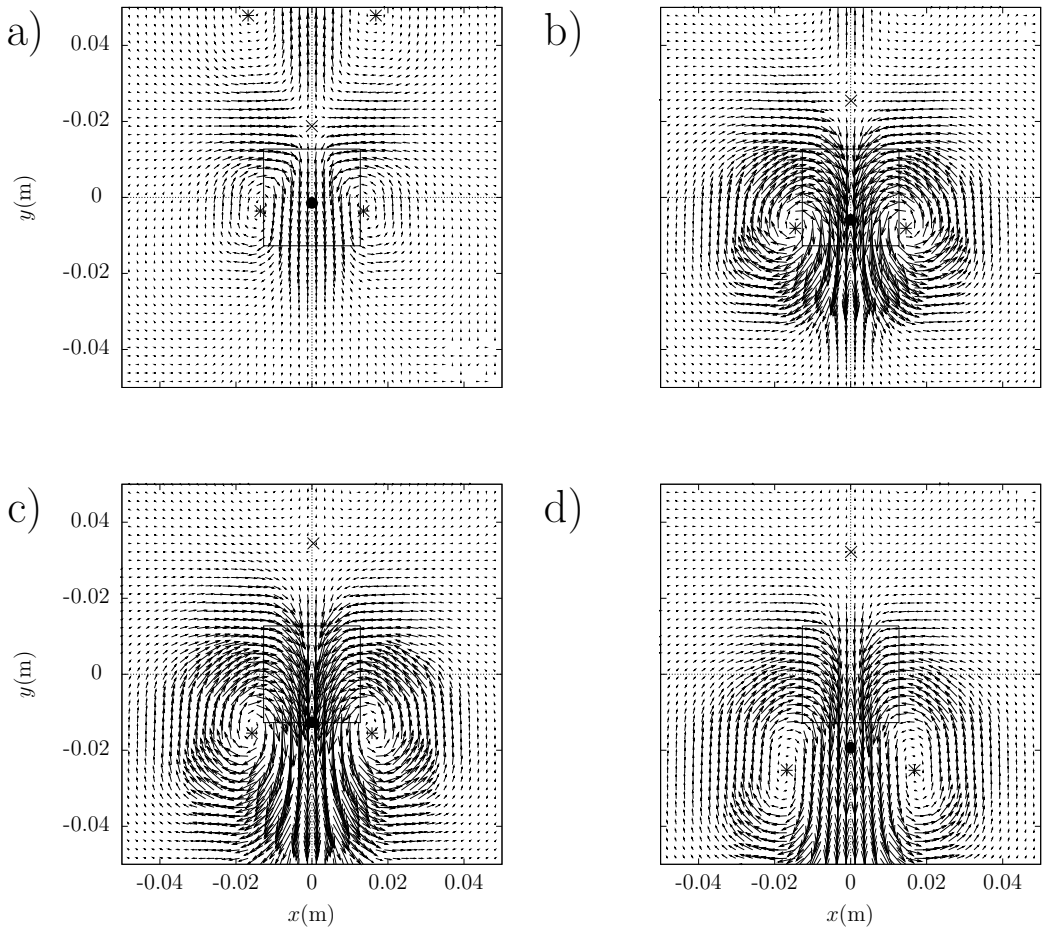

Figure 3.1: Oscillating dipole vortex, experimental velocity field. The black dot • corresponds to point of instantaneous maximum velocity. Asteriscs $*$ and crosses $\times$ denote the elliptical and hyperbolic points in the flow, respectively. Phases in different pictures are: a) $\varphi = 2/10\ \pi$, b) $\varphi = 4/10\ \pi$, c) $\varphi = 6/10\ \pi$ and d) $\varphi = 8/10\ \pi$. The square denotes the footprint of the magnet with its dipole moment pointing in the positive $z-$direction. For the velocity scale, see figure 3.3. Forcing frequency f=50 mHz.

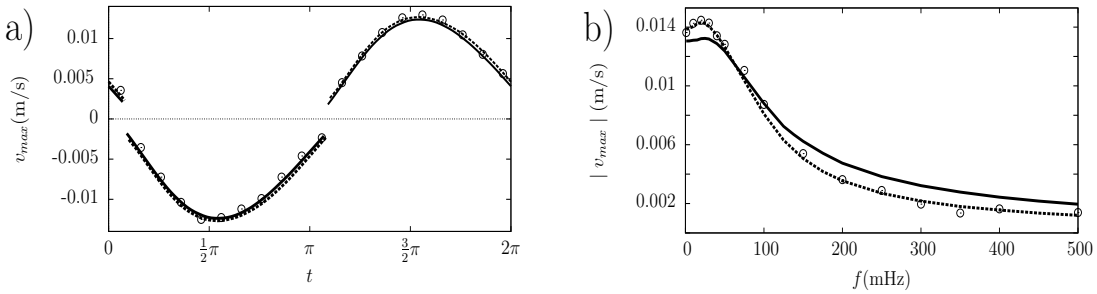

Figure 3.2: Oscillating dipole vortex. a) Instantaneous maximum velocity as a function of time t for forcing frequency f=50 mHz. b) Amplitude of the instantaneous maximum velocity as a function of the forcing frequency f. Experimental data and theoretical predictions are represented by open symbols and lines, respectively. Continuous line Q2D model; dashed line 3D model. Cylindrical magnet

a marked asymmetry dictated by the main flow direction. This asymmetry is stronger at $\varphi = 4/10\ \pi$, that is, when Lorentz force is increased and convective effects displace the maximum velocity downstream from the point of maximum magnetic field strength. The change of sign in the velocity is due to the existence of two dipole vortex, whose main jet points in opposite directions every half cycle. Also, zero magnitude of velocity $v(0, y)$ denotes the position of the hyperbolic point of the flow. As stated in Chapter 2, the formation of the pair of counter rotating lobes occurs every half cycle as the direction of the Lorentz force is inverted. Therefore, the velocity components in the $(x - y)$ plane show the following cyclic symmetry:

$$\left.\begin{aligned} u(x, y, t) &= u(x, -y, t + \pi), \\ v(x, y, t) &= -v(x, -y, t + \pi). \end{aligned}\right\} \tag{3.7}$$

Both numerical predictions of the velocity profiles as a function of position and time are compatible with the experimental results. Since the friction model was built with the flow base, namely, the oscillating vortex dipole generated by the interaction of the magnetic field produced by a single magnet and a transver-

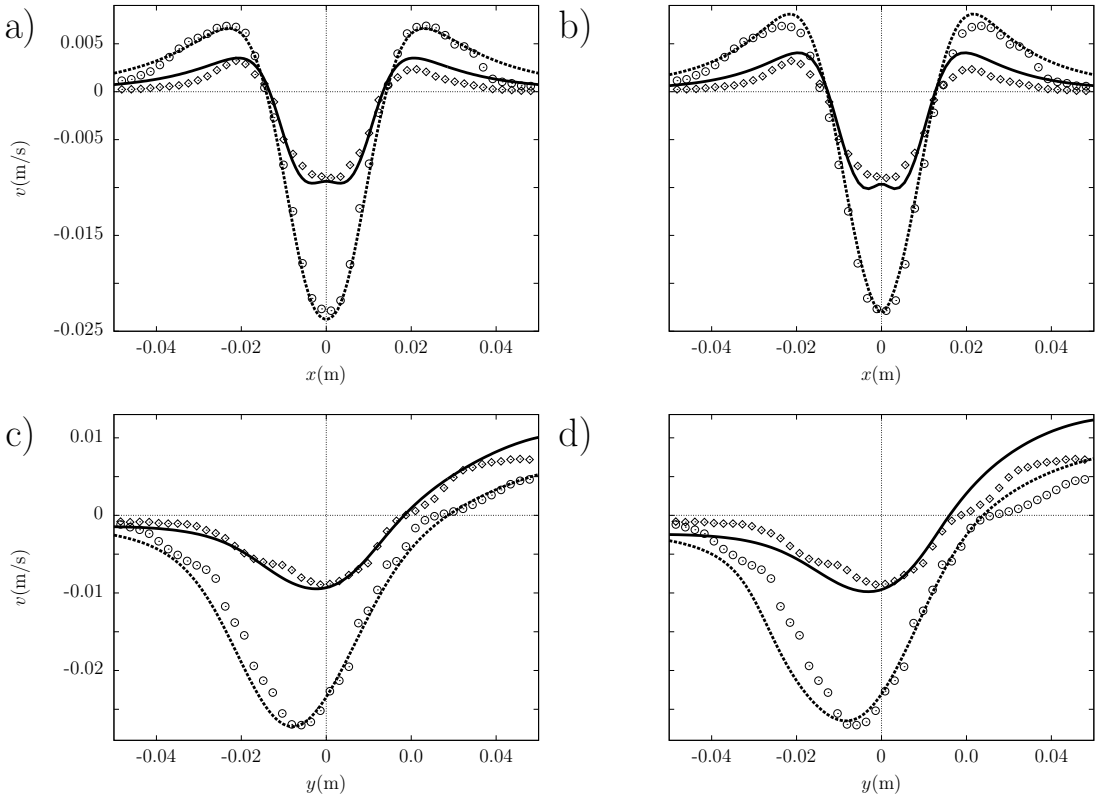

Figure 3.3: Velocity component v as a function of position for oscillating dipole vortex. Experimental data and theoretical predictions are represented by open symbols and lines, respectively. Diamond $\diamond$ and continuous line: $\varphi = 2/10\ \pi$; circle $\odot$ and dashed line: $\varphi = 4/10\ \pi$. First row, $v(x, 0)$; second row, $v(0, y)$. Left column: Q2D model. Right column: 3D model. Forcing frequency f=50 mHz. Rectangular magnet.

sal electric current, the quasi-two-dimensional description reproduce satisfactorily the main physical effects observed experimentally. Unexpectedly, when comparing velocity profiles from both models, the Q2D model seems to fit better the experimental observations than the 3D model. This is attributed to the calibration of the models. The Q2D model was calibrated with ten runs. In contrast, for the sake of time, the 3D model was calibrated with only 3 runs. Every run consisted in increasing from 5 to 25% the maximum magnitude of the magnetic field distribution, since both models seem to underestimate the driving Lorentz force. The run that best fitted the experimental observations was chosen. A better fitting of the 3D model is expected by increasing the amount of runs for the calibration.

Oscillating vortex flow in a quadrupolar magnetic field

When an array of two magnets symetrically aligned along the y-axis with their dipole moment pointing in opposite directions is used, two pairs of dipole vortex are generated, as seen in figure 3.4. In this figure, we present two snapshots at $\varphi = 4/10\ \pi$ and $\varphi = 14/10\ \pi$ of the experimental velocity field, together with the critical points of the oscillating vortex flow in a quadrupolar magnetic field. The forcing frequency is f=50 mHz. This time-dependent flow presents cyclic symmetry with a period of one cycle:

$$\left.\begin{array}{l} u(x,y,t) = u(x,y,t+2\pi), \\ v(x,y,t) = v(x,y,t+2\pi). \end{array}\right\} \tag{3.8}$$

When $0 < \varphi \leq \pi$, central flow of the dipole vortices collide with each other giving rise to a couple of two opposite dipole vortices in the x-direction, see figure 3.4(a). When $\pi < \varphi \leq 2\pi$, figure 3.4(b), dipole vortices move away from each other in the y-direction. With this magnet array, up to four dipole vortices can be identified by determining the elliptic points (asteriscs $*$), as can be seen in figure 3.4(b). Hyperbolic points (crosses $\times$) are located at the central region where two dipole vortices are connected.

Figures 3.5(a) and 3.5(b) show the velocity component v plotted as a function of y-coordinate at x=0 ($v(0,y)$) for two phases. Figure 3.5(a) shows the comparison between the experimental profiles and the corresponding ones with the Q2D model, while figure 3.5(b) displays the comparison with the 3D model profiles. The velocity distribution is nearly symmetric around the $y = 0$ line, showing a maximum magnitude at the middle of each dipole vortex center. Since the

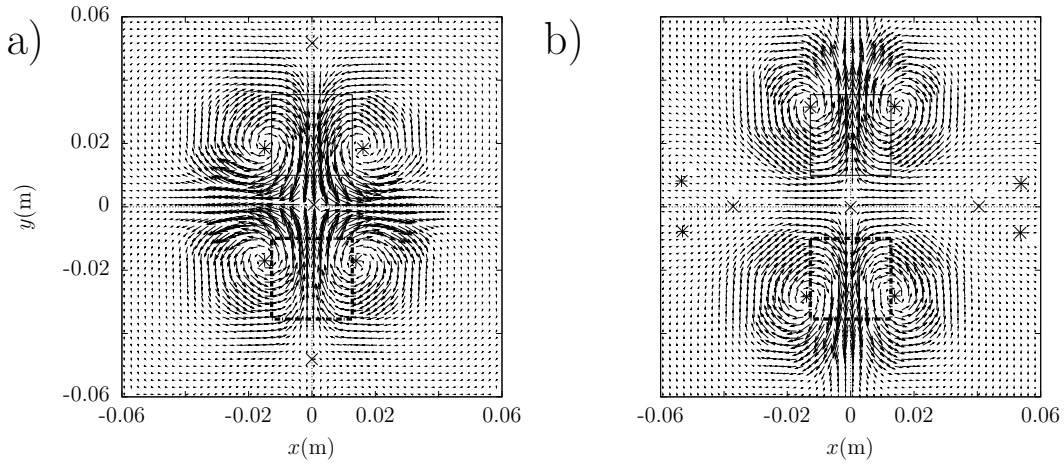

Figure 3.4: Oscillating vortex flow in a quadrupolar magnetic field, experimental velocity field. Asterisc $*$ and crosses $\times$ denote the elliptical and hyperbolic points in the flow. Phases in different pictures are: a) $\varphi = 4/10\ \pi$ and b) $\varphi = 14/10\ \pi$. The squares denote the footprint of the magnets. Continuous lines indicate that the dipole moment points in the positive z direction. The dipole moment of the dashed square points in the negative z direction. For the velocity scale, see figure 3.5. Forcing frequency f=50 mHz.

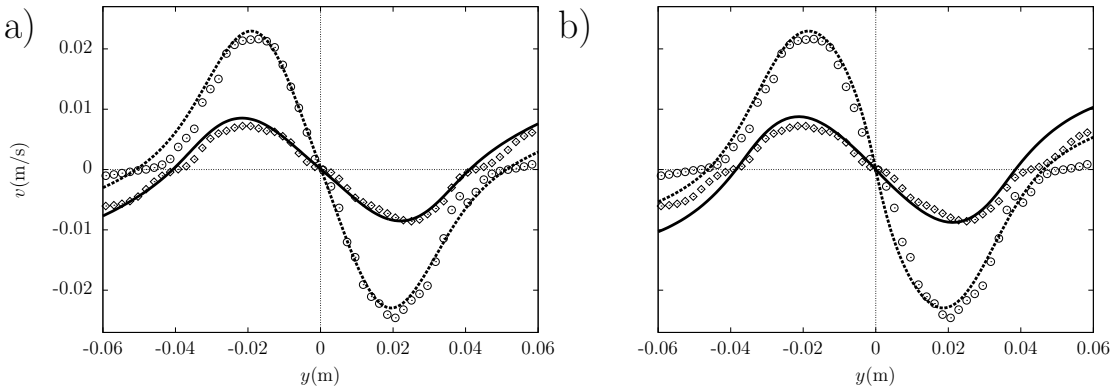

Figure 3.5: Velocity component v as a function of y coordinate at $x = 0$ for oscillating vortex flow in a quadrupolar magnetic field. Experimental data and theoretical predictions are represented by open symbols and lines, respectively. Diamond $\diamond$ and continuous line: $\varphi = 2/10\ \pi$; circle $\odot$ and dashed line: $\varphi = 4/10\ \pi$. a) Q2D model. b) 3D model. Forcing frequency f=50 mHz. Rectangular magnet.

Lorentz force generates the two dipole vortices in opposite directions, the magnitude of the velocity changes its sign. The hyperbolic points are located at points where the magnitude of the velocity vanishes.

Oscillating vortex flow in an octopolar magnetic field

The flow generated by an array of four magnets symetrically located at each quadrant of the $(x-y)$ plane is shown in figure 3.6. The magnetic dipole of the magnets in quadrants I and II point in the positive z-direction while the magnetic dipole of magnets in quadrants III and IV are pointing in the negative z-direction. The Lorentz force generates a complex flow structure for each half cycle. This time-dependent flow also presents cyclic symmetry with a period of one cycle (eq. (3.8)). Elliptical points (asteriscs $*$) show that both flow structures are composed of a total of eight vortices. We must note that in contrast with the vortex flows due to arrays of one and two magnets, isolated dipole vortices are no longer distiguished in the flow in an octopolar magnetic field. Along the x axis we can observe three hyperbolic points (cross $\times$) located at points where jets collide. Four outer hyperbolic points are located at the regions connecting the main flow structure with four dipole vortices, expelled when the Lorenz force

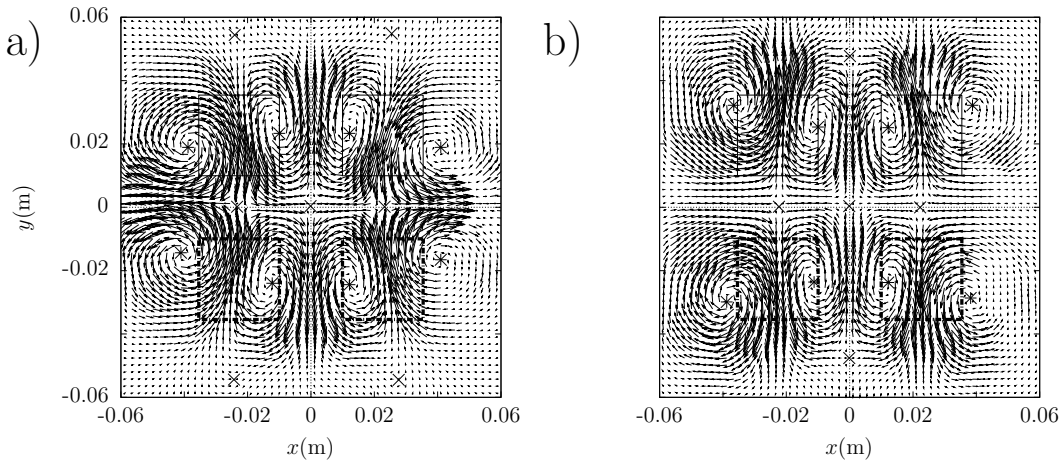

Figure 3.6: Oscillating vortex flow in an octopolar magnetic field, experimental velocity field. Asterisc $*$ and crosses $\times$ denote the hyperbolic and elliptical points in the flow. Phases in different pictures are: a) $\varphi = 4/10\ \pi$ and b) $\varphi = 14/10\ \pi$. The squares denote the footprint of the magnets. Continuous lines indicate that the dipole moment points in the positive z direction. The dipole moment of the dashed square points in the negative z direction. For the velocity scale, see figure 3.7. Forcing frequency f=50 mHz.

is inverted. In figure 3.6(a) we observe that two dipole vortices were expelled in the positive y direction, and the remaining in the negative y direction. Although in figure 3.6(b) only two outer hyperbolic points along the y axis are observed, indicating that two dipole vortices were expelled in the positive and negative y direction, the remaining hyperbolic points are located along the x axis, showing that another two dipole vortices were expelled in the positive and negative x direction.

Figure 3.7(a) shows the comparison between the experimental and profiles provided by the Q2D model, while figure 3.7(b) displays the comparison with the 3D model profiles. Since during the second half of the cycle two jets collide in the central region (figure 3.6(b)), as it also happens in the flow in a quadrupolar magnetic field (figure 3.4(a)), the profile of the v velocity component along the y axis shows a similar behavior as the corresponding for the flow in the quadrupole magnetic field, see figure 3.5.

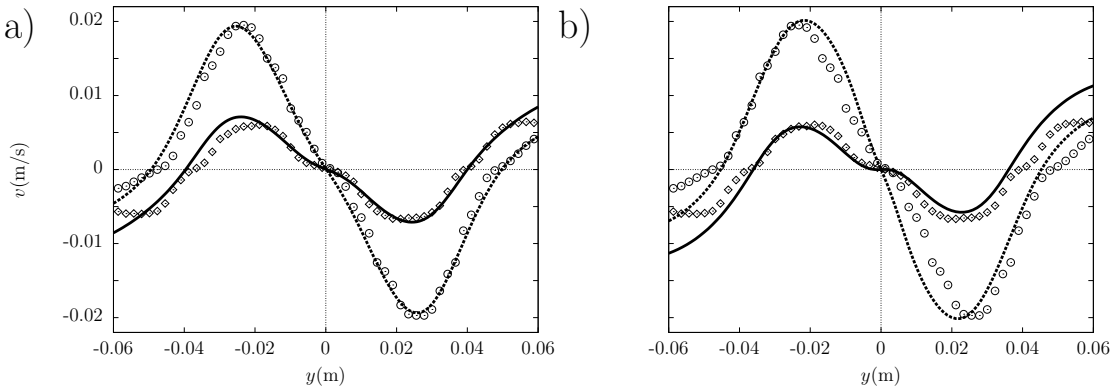

Figure 3.7: Velocity component v as a function of y coordinate at $x = 0$ for oscillating vortex flow in an octopolar magnetic field. Experimental data and theoretical predictions are represented by open symbols and lines, respectively. Diamond $\diamond$ and continuous line: $\varphi = 12/10\ \pi$; circle $\odot$ and dashed line: $\varphi = 14/10\ \pi$. a) Q2D model. b) 3D model. Forcing frequency f=50 mHz. Rectangular magnet.

Oscillating vortex flow due to a disordered array of five magnets

Figure 3.8 shows two snapshots at $\varphi = 4/10\ \pi$ and $\varphi = 14/10\ \pi$ of the flow due to a disordered array of five magnets. In contrast with the previous flow patterns (in dipolar, quadrupolar and octopolar magnetic fields), the Lorentz force generates complex nonsymmetric flow structures which do not follow the rule of $2n$ vortices, where n is the number of magnets. Since the flow structure is composed of only nine vortices, not ten. Magnets in the center generate two colliding dipoles resulting in a flow structure similar to a tripole, which consist of a linear arrangement of three vortices of alternating sign. However, strictly, this flow pattern cannot be considered as a tripole since the flow a structure does not rotate in the direction of the core vortex rotation (Barba $\&$ Velasco 2008). As well as in the previous figures, hyperbolic points indicate the position of the crossing of separatrices lines.

Figures 3.9(a) and 3.9(b) show the velocity component u plotted as func-

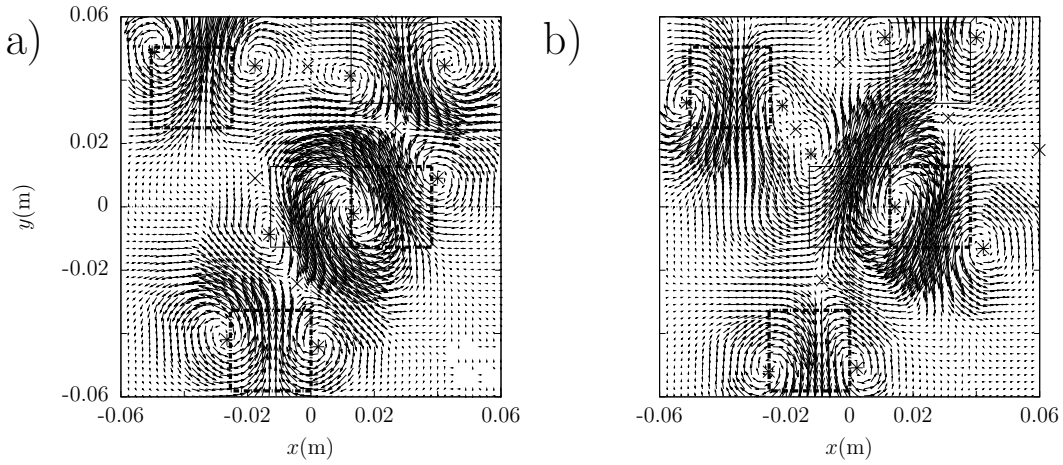

Figure 3.8: Oscillating vortex flow due to a disordered array of five magnets, experimental velocity field. Asterisc $*$ and crosses $\times$ denote the hyperbolic and elliptical points in the flow. Phases in different pictures are: a) $\varphi = 4/10\ \pi$ and b) $\varphi = 14/10\ \pi$. The squares denote the footprint of the magnets. Continuous lines indicate that the dipole moment points in the positive z direction. The dipole moment of the dashed square points in the negative z direction. For the velocity scale, see figure 3.9. Forcing frequency f=50 mHz.

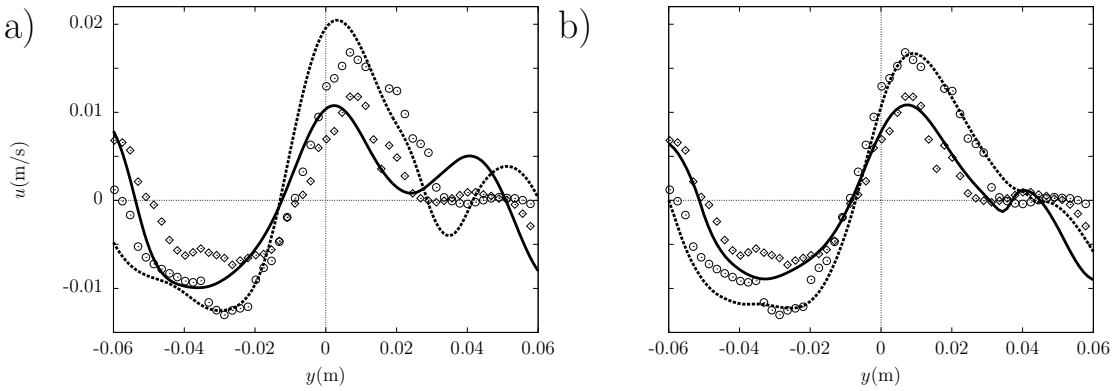

Figure 3.9: Velocity component u as a function of y coordinate at $x = 0$ for oscillating vortex flow due to a disordered array of five magnets. Experimental data and theoretical predictions are represented by open symbols and lines, respectively. Diamond $\diamond$ and continuous line: $\varphi = 12/10\ \pi$; circle $\odot$ and dashed line: $\varphi = 14/10\ \pi$. a) Q2D model. b) 3D model. Forcing frequency f=50 mHz. Rectangular magnet.

tion of y-coordinate at x=0 ($u(0, y)$) for two phases. Figure 3.9(a) shows the comparison between the experimental and profiles provided by the Q2D model, while figure 3.9(a) displays the comparison with the 3D model profiles. Velocity profiles are no longer symmetric. Clearly, the Q2D model seem to lose capability of prediction. Nevertheless, even with these complex flows, Q2D profiles capture most of the qualitative features of the experimentally observed structure.

In general, the both Q2D and 3D numerical results present a very good quantitative agreement with the experimental measurements in the full range of explored forcing frequencies and arrays of magnets used. These results indicate that the quasi-two-dimensional model is able to reproduce the time-dependent electromagnetically forced flows in the shallow layer. Reliability of the averaging procedure depends, in turn, on the proper modelling of the velocity profiles in the depth of the shallow layer. Even if the time scale dissipation (3.6) used for the Q2D model was calculated through considering a traversal velocity profile (3.5) generated by a single magnet, the friction model seems to be used for considering flows with dipole vortex structures (flows in dipolar, quadrupolar and octopolar magnetic fields), which ensures that boundary layers behave as Stokes layers. It is therefore expected to be a reasonable assessment of the bottom friction based on the Stokes-like velocity profile. Although the Q2D theory seem to reproduce

satisfactorily the flow generated by the disordered array of five magnets, larger differences in comparing the velocity components are found. As will be explained in the following section, this is not attributed to three-dimensionality of the flow, but rather to our friction model.

3.4.2 Three-dimensionality of the flows in terms of kinetic energy

An estimation of the three-dimensionality of the flows calculated numerically was obtained through the kinetic energy ratio between the kinetic energy of the horizontal velocity components u and v, and the the kinetic energy of the vertical velocity component w, both obtained at a given $(x-y)$ plane. Global instantaneous horizontal and vertical kinetic energies E_h and E_v, respectively, are defined as (Akkermans *et al.* 2008b):

$$E_h = \frac{1}{2}h\int\int_S \rho(u^2+v^2)dxdy, \qquad E_v = \frac{1}{2}h\int\int_S \rho w^2 dxdy, \tag{3.9}$$

where S denotes the horizontal plane which will be taken at z=3.5 mm. The kinetic energy ratio is used as a measure for inherent three-dimensionality of the flow. When the kinetic energy ratio $(E_h - E_v)/E_h$ equals to 1, the kinetic energy due to the velocity component w is equal to zero, thus flow is fully quasi-two-dimensional. As the kinetic energy ratio is decreased, the kinetic energy due to the velocity component w accounts and thus the flow is three-dimensional. Figure 3.10 shows the kinetic energy ratio as a function of time for the oscillating dipole vortex for different frequencies. For f=10 mHz, it is shown that three-dimensional effects increase during the onset of the flow and when the driving force is inverted (every half cycle), but after a short period 3D effects dissapear and the kinetic energy ratio increases approximately to 1. This behavior agrees with the previously stated by Paret *et al.* (1997): after a transient state the flow can be treated as two dimensional. This behavior is similar for larger forcing frequencies (f=50, 100 and 200 mHz) but delayed with a larger lag for the larger frequencies. We also note that as increasing f from 10 to 100 mHz, 3D effects also increase. Nevertheless, when f is 200 mHz, 3D effects are noticeable only at starting times. We conclude that since the energy contained in the vertical motions is in most cases less than 0.03 $\%$ of the energy of the horizontal motions, the dipole flow structure can be considered two dimensional.

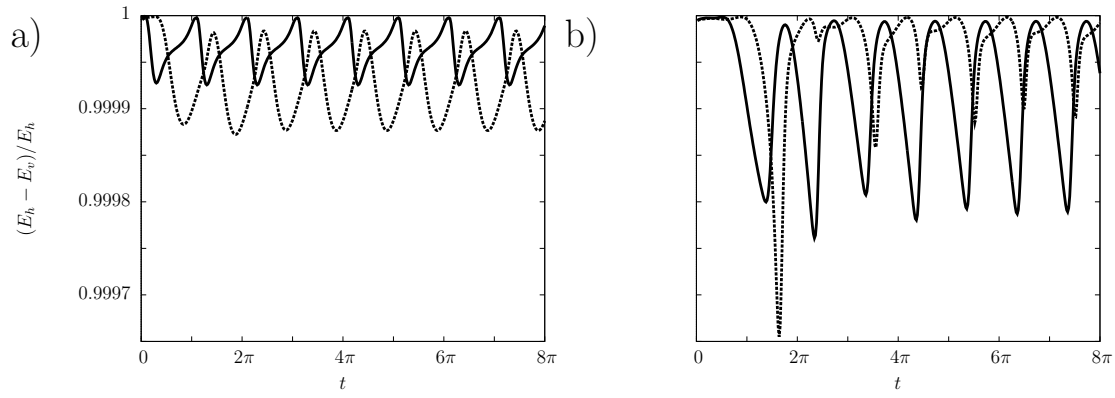

Figure 3.10: Numerically calculated kinetic energy ratio as function of time for dipole oscillating vortex. a) Continuous and dashed line denotes f=10 and 50 mHz, respectively. b) Continuous and dashed line denotes f=100 and 200 mHz, respectively. Cylindrical magnet.

The kinetic energy ratio for the different flows structures is shown as a function of time in figure 3.11. The forcing frequency is f=50 mHz. From this figure we find that the flow in the quadrupolar magnetic field is the most three-dimensional flow. In this case, we note that a different flow structure is generated in the first and second halves every cycle. The flow occurring in $0 < \varphi \leq \pi$ when the jets of the dipole vortices collide is more three-dimensional than that in the second half ($\pi < \varphi \leq 2\pi$), when the dipole vortices evolve without interacting with each other. A similar behavior is observerd for the flow in the octopolar magnetic field. From the previous observations we can say that when dipoles collide, more three-dimensional effects arise in the flow. Unexpectedly, the flow due to the disordered array of magnets is less three-dimensional than the flows due to the quadrupolar and octopolar magnetic fields. From figures 3.10(a) and 3.11(a) we can compare the three-dimensionality for the oscillating dipole vortex flow due to the cylindrical and the rectangular magnet for the forcing frequency f=50mHz. According to the shallow flow approximation, which states that when $\varepsilon \rightarrow 0$ the flow is considered two dimensional, the flow due to the cylindrical shape magnet ε=0.21 is slighly more three-dimensional than the generated by the rectangular magnet ε=0.16. In terms of the energy criterium, all vortex flows analyzed are quasi-two-dimensional.

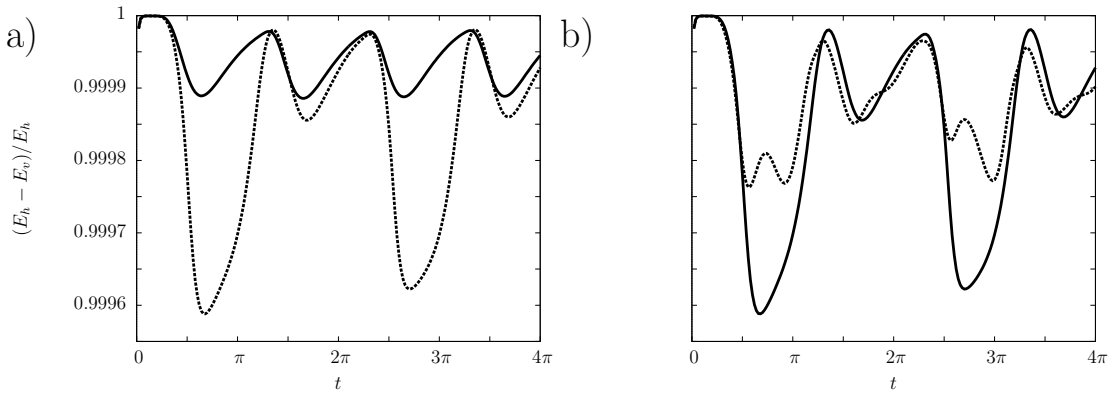

Figure 3.11: Numerically calculated kinetic energy ratio as function of time for different flow patterns. a) Continuous line and dashed line denotes the flows due to arrays of one and twor magnets, respectively. b) Continuous line and dashed line denotes the flows due to arrays of four ordered and five disordered magnets, respectively. Forcing frequency f=50 mHz. Rectangular magnet.

3.5 Discussion

The laminar vortex flows in a shallow layer of an electrolytic solution were studied experimentally and theoretically. The flow patterns were generated by the interaction of magnetic distributions due to arrays of dipolar magnets and a uniform alternate current. Under the explored forcing, from f=1 to 500 mHz, the base flow generated by a single magnet, namely, the oscillating vortex dipole, shows an unexpected resonant behavior around f=10 mHz. When multipoles are used to generate the magnetic field, complex flow patterns are obtained. Convective effects were observed by the elongation of the vortices in the main direction of the Lorentz force along with the displacement of the point of maximum velocity and geometrical points.

Since the depth of the electrolyte layer (4 mm) is much smaller than its horizontal extension (360×280 mm), a relatively simple quasi-two-dimensional theory that correctly compares with available experimental results is proposed. The Q2D model includes convective effects and involves the integration (averaging) of governing equations in the vertical direction. It describes the flows in terms of a two-dimensional core flow with a linear friction that accounts for the effects of the boundary layers. The damping of velocity due to bottom friction was calculated through an analytical velocity profile normal to the wall

(Chapter 2). The magnetic field distribution originated by a dipole permanent magnet was realistically approximated by considering only its component in the normal direction. The numerical quasi-two-dimensional scheme can be extended to consider several magnets. This simple Q2D model greatly simplifies modelling flows, offers reasonable results and avoids difficulties of a full three-dimensional approach. In order to corraborate the quasi-two-dimensional predictions, a full three-dimensional numerical model was built. With the three-dimensional calculated vectorial fields, the presumption of quasi-two-dimensionality of these flows was corroborated by an analysis of kinetic energy at the z=3.5 mm plane.

The results reported indicate that a quasi-two-dimensional description is suitable for time-dependent electromagnetically driven shallow flows. In general, a good quantitative comparison is found between numerical results and experimental observations. For the Q2D model, the key elements are the accurate estimation of the bottom viscous friction and the magnetic field distribution, in both considering the variation of the magnetic field strength in the normal direction. Whereas for the 3D model, a good representation of the three-dimensional magnetic field distribution is the key element.

In general, when comparing velocity profiles from both models, the Q2D model seems to fit better the experimental observations than the 3D model. This is attributed to the calibration of the models with the experimental observations for the oscillating dipole flow. The Q2D model was calibrated with ten runs. In contrast, for the sake of time, the 3D model was calibrated with only 3 runs. Every run consisted in increasing from 5% to 25% the maximum magnitude of the magnetic field distribution, since both models seem to underestimate the driving Lorentz force. The run that best fitted the experimental observations was chosen. A better fitting of the 3D model is expected by increasing the amount of runs for the calibration.

Chapter 4

Mixing in oscillatory vortex flows in multipolar magnetic fields

In this Chapter[1], we study, experimentally and theoretically, the mixing in continuously driven laminar flows produced by oscillating electromagnetic forces in a thin electrolytic fluid layer. We analyze the mixing properties of some of the multipolar vortex flows studied in Chapter 3 and, in addition, new flows produced by the injecting two time-dependent electric currents in orthogonal directions are also considered. First, the stretching and folding process is analyzed by comparing flow visualizations with dyed water and numerical Lagrangian particle tracking. It is found that multipolar flows present symmetries, according to the magnetic field distributions, that inhibit the fluid mixing. Symmetries can be destroyed (and the fluid mixing enhanced) by the use of a disordered array of magnets (Voth et al. 2002; 2003) or by injecting two electric currents perpendicular to each other. In addition, the convection-diffusion of a passive scalar in multipolar flow fields was determined by the use of the diffusive strip method (Meunier & Villermaux 2010) which allows to solve the diffusion phenomena in a two-dimensional field at high Péclet numbers.

[1]This Chapter is mainly based on the paper: Figueroa, A., Meunier, P., Cuevas, S. & Villermaux, E., 2010, "Mixing in electromagnetically driven oscillatory multipolar vortex flows". In preparation.

4.1 Introduction

Fluid mixing is a very important subject for multiple applications in geophysics, chemestry and biology, as well as in many relevant industrial devices. Recently, significant research efforts have been devoted to find methods to quantify and accelerate mixing. Some methods take advantage of mechanical interactions to mix fluids, for instance, by turning a propeller in a container or through the periodic displacement of the container's walls (Chien *et al.* 1986). The mixing obtained in the annular region between rotating concentric cylinders has also received attention (Aref & Balachandar 1986). Of particular interest are non-intrusive methods that rely on the use of electromagnetic forces to produce stirring and eventually mixing in electrically conducting fluids. In particular, electromagnetic forcing has been widely used experimentally to produce mixing in shallow layers of liquid metals (Sommeria 1988a; 1988b) or electrolytes (Voth *et al.* 2003). The idea is to generate a rotational Lorentz force by the injection of electric currents in a thin fluid layer exposed to a steady external magnetic field. In this way, it is possible to explore flows that under certain conditions may present a quasi-two-dimensional behavior. Incidentally, these flows are similar to those found in the ocean and the atmosphere (McWilliams 2006) where the transport of particles (Brown *et al.* 2000) or nutrients (Wolansky *et al.* 1988) are of great importance.

Dynamical systems approaches based on flow kinematics have provided a first insight into chaotic mixing (Aref 1984; Leong & Ottino 1989). Extensive studies of mixing have yielded important insights into the geometric structures that govern the mixing process, particularly in two-dimensional flows. A central goal of the study of fluid mixing is to understand and predict the rate at which an initially inhomogeneous fluid is homogenized. This can be done, for instance, by the measuring scalar concentration fields. Experimental (Rothstein *et al.* 1999) and numerical (Fereday *et al.* 2002) studies have obtained an exponential decay for the variance of a diffusive scalar concentration field in a chaotic mixer, that results in a global exponential decay of the dye's spatial contrast. These studies show that mixing rates are more accurately predicted by an effective diffusion model than by a model based on finite time Lyapunov exponents. While turbulent flows lead to highly efficient mixing, it can be greatly enhanced in laminar flows by subjecting the fluid to chaotic flow kinematics (Aref 1984).

The importance of the stirring mechanism relative to the molecular diffusion of a scalar in a given mixing problem is measured through a nondimensional parameter called the Péclet number, defined as $Pe = UL/D$, where U is a

typical flow speed, L is a characteristic length scale, and D is the molecular diffusivity. Physically, the condition $Pe \gg 1$ implies that the stretching of the fluid interface by convection proceeds for a substantial amount of time before diffusive effects eventually smear out the interface and mix the fluids at small length scales. However, large Pe values also render the numerical solution of the convection-diffusion equation extremely challenging (Gleeson 2005). Chaotic mixing devices aim to achieve exponential growth of the total interface length in time by stretching and folding the fluids in similar fashion to the transformation maps of chaotic dynamics theory (Ottino 1989).

In order to quantify mixing efficiency one has to define what is mixing on mathematical grounds. Indeed, perfect mixing requires the scalar concentration to be uniform. A spatial criterion is not sufficient to quantify mixing efficiency, since the required time to reach a satisfactory dye distribution has to be set as small as possible. A central question in scalar mixing is the satisfactory description of the histogram or probability density function (PDF) $P(c)$ of the concentration levels c of a substance being mixed.

In electromagnetically driven flows, mixing can be enhanced by increasing the number of magnets and by injecting an oscillating electrical current which, under certain conditions, can lead to a resonant flow (Solomon *et al.* 2001). However, as it will be shown below, lines of symmetry that inhibit material transport and thus mixing, are inherent in these kind of flows due to symmetries of the magnetic field distribution. This is particularly clear when ordered arrays of magnets are used. It has been found that symmetry lines can be broken by using a disordered array of magnets or by increasing the intensity of the applied current to create a strong Lorentz force (Voth *et al.* 2003) which also breaks time-reversal symmetry. In these cases, the mixing rates are substantially increased. In fact, even if an ordered array of magnets is used, instability conditions can be reached when a sufficiently strong direct current is injected, leading to spatio-temporal chaos (Ouellette $\&$ Gollub 2007). Moreover, strong currents can be avoided if alternate currents are applied in both cardinal directions, which leads to chaotic mixing that is typically barrier-free (Solomon *et al.* 2008). In the following sections, we explore the mixing characteristics of electromagnetically driven multipolar vortex flows by analayzing the kinematic Lagrangian trajectories as well as the convection-diffusion of a passive scalar in quasi-two-dimensional (Q2D) flows. We start with a brief explanation of the experimental procedure.

4.2 Experimental procedure

Essentially, dyed water visualization experiments were carried out in two different cases. The first case involves the multipolar flows already described in Chapter 3 where a one-directional alternate current is injected in the thin fluid layer in the presence of one or several permanent magnets. Using similar magnetic field distributions, in the second case two alternate currents were injected in orthogonal directions. In order to achieve this condition, the experimental setup already described somewhat in detail in the previous Chapters, was slightly modified. Here we only emphasize the modifications implemented to the experimental device. Avoiding short circuits, two pairs of copper electrodes were placed along the inner borders of the rectangular container. Each pair of electrodes are connected to a *DS345* function generator for obtaining independent electric signals. Each function generator allows to modify the frequency and the phase of the signals. The amplitude of the electric current in both directions was fixed to 80 mA with frequencies of f=50, 100 and 200 mHz. Arrays of rectangular parallelepiped magnets with a side length of 25.4 mm, height of 12.7 mm and maximum strength of 0.38 T were placed underneath the bottom wall. Depending on the number of magnets and their geometrical position, Lorentz force generated different oscillating vortical flow structures in the $(x-y)$ plane. In order to analyze the mixing properties of the electromagnetically driven flows, in a first set of experiments, drops of dyed water of different colors (food colors) were injected at each geometrical quadrant on the surface of the layer. In a second set of experiments, a uniform blob of dye with radius r ≈5 mm was deposited on the surface of the quiescent electrolyte layer. The dye was disodium fluoresceine with initial concentration c_0 ≈10^{-5} mol l^{-1} and molecular diffusivity $D = 5 \times 10^{-10}$ m^2/s. Since fluorescein has a maximum absorption at a wavelength of 494 nm and a maximum emission at 521 nm (in water), experiments were undertaken in a dark room illuminated with two symmetrically placed ultraviolet lamps. Moreover, as the electrolite is a transparent medium, the bottom wall was covered with a black sheet for ensuring the contrast in the visualization. Images of the fluoresceine's concentration field in the whole container domain were recorded every 5 s with a Nikon D80 camera with a AF micro-nikkor 60mm f/2.8D lens. The resulting background subtracted grey levels are proportional to the dye concentration.

4.3 Theoretical model

4.3.1 Quasi-two-dimensional numerical model

The velocity fields of the explored experimental flows were numerically simulated using a Q2D model as the one presented in Chapter 3 but extended to consider Lorentz forces in both x- and y-directions. As stated in the previous Chapter, the Q2D model is based on an averaging approach and flows are described in terms of two-dimensional core variables with a linear friction that accounts for the effects of the oscillating boundary layer. Using the same dimensionless variables of Chapter 3, the governing equations read

$$\frac{\partial u}{\partial x} + \frac{\partial v}{\partial y} = 0, \tag{4.1}$$

$$R_\omega \frac{\partial u}{\partial t} + u\frac{\partial u}{\partial x} + v\frac{\partial u}{\partial y} = -\frac{\partial P}{\partial x} + \nabla_\perp^2 u - \frac{u}{\tau} + \alpha Re_* \sin(\Omega_y t + \phi_y)\mathcal{B}_z^0, \tag{4.2}$$

$$R_\omega \frac{\partial v}{\partial t} + u\frac{\partial v}{\partial x} + v\frac{\partial v}{\partial y} = -\frac{\partial P}{\partial y} + \nabla_\perp^2 v - \frac{v}{\tau} - \alpha Re_* \sin(\Omega_x t + \phi_x)\mathcal{B}_z^0, \tag{4.3}$$

where the parameters $Re_* = U_0 L/\nu$ and $R_\omega = \omega L^2/\nu$, stand for the Reynolds and oscillation Reynolds numbers, respectively. The characteristic bulk velocity U_0 is obtained from a balance between viscous and Lorentz forces, see § 1.3.1. The last terms on the right-hand side of equations (4.2-4.3) consider the oscillating Lorentz force created by the magnetic field distribution $\mathcal{B}_z^0$, and the injected currents in the x- and y-direction, namely, $\sin(\Omega_x t + \phi_x)\ \hat{\boldsymbol{x}} + \sin(\Omega_y t + \phi_y)\ \hat{\boldsymbol{y}}$, which is normalized by the current amplitude j^0. The dimensionless angular frequencies are denoted by $\Omega_x{=}f_x/f$ and $\Omega_y{=}f_y/f$, where $f = (f_x + fy)/2$. The phase-shifts of the electrical signals are denoted by ϕ_x and ϕ_y. Time t is normalized by ω, where $\omega = 2\pi f$. The inverse of the characteristic time scale τ and the parameter α are calculated from equations (3.6) and (1.16), respectively, with $\gamma{=}2.16$. According to the shallow flow approximation, the aspect ratio $\varepsilon = h/L$, where h is the layer thickness and L the characteriztic length of the magnet, is assumed to be less than unity (in the experiment, the maximum value of ε was 0.16). This Q2D model was solved using a numerical scheme alreday described in Chapter 1. The numerical velocity fields were used to calculate the Lagrangian trajectories, as well as the convection-diffusion equation for a passive scalar using the Diffusive Strip Method explained below.

4.3.2 Diffusive Strip Method (DSM)

A central question in scalar mixing is the satisfactory description of the histogram or probability density function (PDF) $P(c)$ of the concentration levels c of a substance being mixed. The concentration c, which acts as a passive scalar, satisfies the convection diffusion equation that in dimensionless terms can be expressed as

$$R_\omega \frac{\partial c}{\partial t} + (\boldsymbol{u} \cdot \boldsymbol{\nabla})\, c = \frac{Re_*}{Pe}\, \boldsymbol{\nabla}^2 c, \tag{4.4}$$

where the previously introduced Péclet number, Pe,(based on the characteristic velocity U_0 and the magnet side length) is a dimensionless parameter which represents the ratio between convective and diffusion effects. In order to obtain the concentration field and document the mixing properties of the electromagnetic stirring, we use the Diffusive Strip Method (DSM) (Meunier & Villermaux 2010) which allows to solve the convection-diffusion of a scalar in a two-dimensional velocity field of an incompressible fluid for large Péclet numbers. Essentially, in this method the scalar is introduced as a material strip represented by an array of Lagrangian passive tracers whose position ($\mathbf{x}_i$) is computed by integrating the equation of motion

$$R_\omega \frac{d\boldsymbol{x}_i}{dt} = \boldsymbol{u}_i, \tag{4.5}$$

where $\boldsymbol{u}_i$ is the velocity of the flow at the tracer position and the subindex i denotes the number of each particle conforming the filament or strip line. In order to solve equation (4.4) a change of frame of reference is performed, so that the new frame is mounted on the i-esim particle of the strip line, as shown in figure 4.1. By introducing the change of variables

$$\frac{d\xi_i}{dt} = \frac{Re_*}{R_\omega\, Pe}\, \frac{1}{s_i^2}, \qquad \mathcal{Y} = \frac{Y}{s_i}, \tag{4.6}$$

where ξ is a dimensionless time, s is the striation thickness and Y is the ordinate of the new reference system, the convection-diffusion equation transforms into a standard diffusion equation (Meunier & Villermaux 2010)

$$\frac{\partial c}{\partial \xi} = \frac{\partial^2 c}{\partial \mathcal{Y}^2}. \tag{4.7}$$

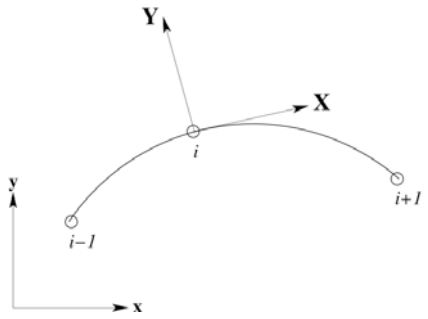

Figure 4.1: Reference frame change.

Using the initial condition $c(0, \mathcal{Y}) = \exp(-\mathcal{Y}^2)$ for equation (4.7), the solution becomes

$$c = \frac{1}{\sqrt{(1+4\xi_i)}} \exp\left(\frac{-\mathcal{Y}^2}{s_i^2(1+4\xi_i)}\right). \tag{4.8}$$

Solution (4.8) can be extended to include transport in the X-direction. In fact, this method solves the associated convection-diffusion problem by computing the local stretching rate along the strip. Thus, the concentration field c is reconstructed by adding small Gaussian ellipses centered on each tracer. The succession of ellipses forms a filament that represents the scalar distribution. In two dimensions the solution for the scalar field c is

$$c = \sum_i \frac{1/1.77264}{\sqrt{1+4\xi_i}} \exp\left(-\frac{\left[(\boldsymbol{x}-\boldsymbol{x}_i)\cdot\widehat{\sigma}_i\right]^2}{\Delta l^2} - \frac{\left[(\boldsymbol{x}-\boldsymbol{x}_i)\cdot\widehat{n}_i\right]^2}{s_i^2(1+4\xi_i)}\right), \tag{4.9}$$

where the term $s_i^2(1+4\xi_i)$ is the local width of the filament, and Δl_i is the distance between two consecutive tracers. The local tangent and normal unitary vectors are denoted by $\widehat{\sigma}_i$ and $\widehat{n}_i$, respectively. The striation thickness s_i can be calculated from

$$s_i = s_0 \, \Delta x_i^0 / \Delta x_i, \tag{4.10}$$

where s_0 is the initial thickness of the strip and Δx_i^0 is the initial separation between consequtive tracers.

A Fortran code was developed to implement the DSM method. Positions of particles are calculated through a second order expansion of equation (4.5). A

detailed explanation of the numerical procedure for the reconstruction of the 2D scalar field (eq. (4.9)) as a function of time with equations (4.6) and (4.10), along with the strip refinement and cusps treatment, can be found in Meunier & Villermaux (2010).

4.4 Results

4.4.1 Lagrangian trajectories and spatial symmetry breaking

In this subsection, pure Lagrangian trajectories (without diffusion effects) calculated numerically by solving equation (4.5) are presented and compared with visualization experiments. Dyed water experimental visualization on the surface of the layer (z=4mm) was mimicked numerically by tracking the motion of a circle with radius r=5 mm, composed initially by an array of 10000 advective particles, uniformly placed in the geometrical center of the flow domain. Once the velocity field is calculated with the Q2D model, these particles are advected by the flow field according to the equation of motion (4.5). Positions of particles are calculated by solving this equation through a second order expansion. Smooth trajectory curves were obtained by inserting new particles if distance between two consecutive particles was larger than a constant. As mention before, this tracking technique does not take into account the diffusion effect of the scalar. Initially, in most of the analyzed flows the circle is divided in four lines, each one lying on a different quadrant. Every line is coulored mimicking the experimental visualization where a drop of different color was set on each quadrant. Figure 4.2(a) shows an experimental picture of the oscillating dipole vortex, whereas figure 4.2(b) shows the corresponding numerical Lagrangian *visualization* or tracking. In this case, the initial circle was divided in two lines (green for $x < 0$ and red for $x > 0$) since two color drops were used in the experiment. As time passes, the Lorentz force stirs the fluid and the flow evolves to form the characteristic dipole vortex that oscillates in the y-direction, clearly showing that the dye is being spread in the spatial domain. Apart from diffusion effects, the Lagrangian tracking reproduces the experimental observation very well. It is clear that fluid mixing occurs, however, it is not homogeneous since a symmetry line exists along the y-axis. This line does not allow the mass to be transported between the left and the right side of the flow domain. Incidentally, this fact is contained in the spatial symmetry of the oscillatory vortex flow stated in Chapter 2, namely,

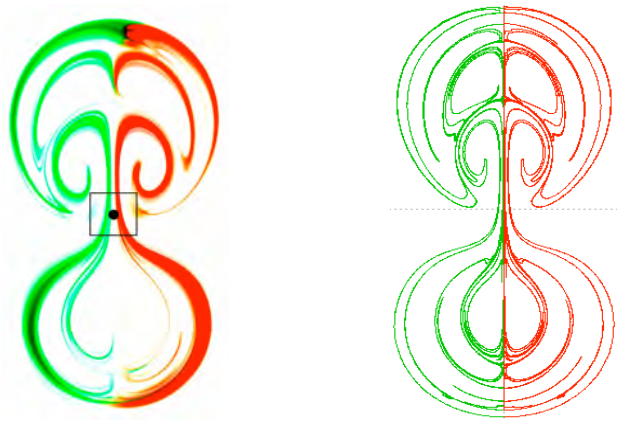

Figure 4.2: Oscillating vortex in a dipolar magnetic field at phase $\varphi = 8/10\ \pi$. a) Experimental visualization. b) Numerical Lagrangian particles tracking. The square denotes the footprint of the magnet. The black dot (•) denotes a magnet with its dipole moment pointing in the positive and negative z-direction. Forcing frequency $f_x = 50$ mHz. Phase-shift $\phi_x = 0$.

$$\left.\begin{aligned} u(x,y,t) &= -u(-x,y,t), \\ v(x,y,t) &= v(-x,y,t). \end{aligned}\right\} \tag{4.11}$$

Figure 4.3 shows the experimental visualization and numerical Lagrangian tracking of an oscillatory vortex flow created when two magnets with opposing polarization are placed along the y-axis, separated by distance slightly larger than the magnet side length. Again, numerical results present a good qualitative comparison with the experiment. It can be observed that, due to the quadrupole magnetic field distribution, the mixed area is larger than in the previous case. Even if the magnetic field is extended with an array of two aligned magnets, the oscillating vortex flow keeps the symmetry line along the y-axis which inhibits mixing between left and right sides. Moreover, a second symmetry line along the x-axis arises. These two symmetry lines prevent mass transport between quadrants, so that mixing occurs indepently at every quadrant. Mathematically, spatial symmetries are expressed in the following way:

$$\left.\begin{aligned} u(x,y,t) &= -u(-x,y,t) = -u(-x,-y,t) = u(x,-y,t), \\ v(x,y,t) &= v(-x,y,t) = -v(-x,-y,t) = -v(x,-y,t). \end{aligned}\right\} \tag{4.12}$$

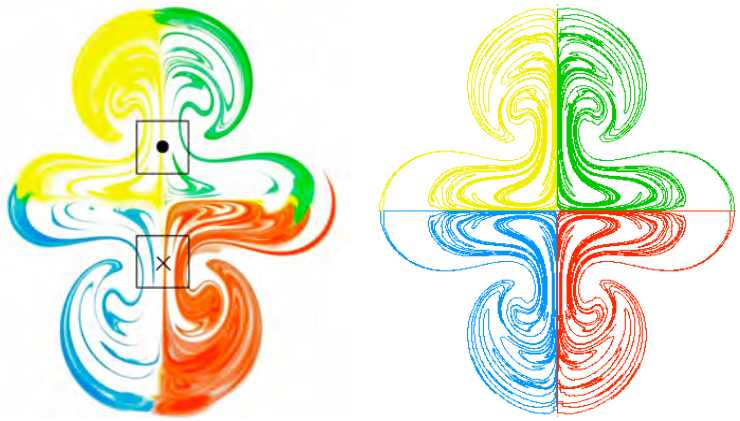

Figure 4.3: Oscillating vortex in a quadrupolar magnetic field at phase $\varphi = 8/10\,\pi$. a) Experimental visualization. b) Numerical Lagrangian particles tracking. The squares denote the footprint of the magnets. The black dot (•) and the cross (×) denote a magnet with its dipole moment pointing in the positive and negative z-direction, respectively. Forcing frequency f_x=100 mHz. Phase-shift $\phi_x = 0$.

In figure 4.4, the oscillatory vortex flow created by an ordered rectangular array of four magnets, is shown. Althoug this octopolar magnetic field distribution generates complex flow structures and increases the mixed area, the oscillating vortex flow keeps the same symmetry lines along the x- and y-axis (equation (4.12)), as the vortex flow in the quadrupolar magnetic field distribution does.

Previous magnetic field distributions generate ordered flow patterns where the mixing is spatially increased as the number of magnets increases, although mixing homogeneity seems to be inhibited by the symmetry conditions. Keeping in mind that flows are in laminar regime and instabilities are avoided, spatial symmetries can be broken when a disordered array of magnets is used (Voth *et al.* 2003). Figure 4.5 shows the experimental visualization and the numerical Lagrangian tracking of the flow generated by a disordered array of five magnets. It can be easily seen that symmetry lines in the x and y-axis are vanished and therefore, mass transport beween quadrants is allowed. In fact, every color can be appreciated at each quadrant and the homogeneity of the mixing is greatly enhanced. Note that the numerical Lagrangian tracking reproduces most of the main flow structures of the time-dependent flow.

Spatial symmetries can also be broken using two orthogonal electric currents.

Figure 4.4: Oscillating vortex in an octopolar magnetic field at phase $\varphi = 18/10\ \pi$. a) Experimental visualization. b) Numerical Lagrangian particles tracking. The squares denote the footpoint of the magnets. The black dot (•) and the cross (×) denote a magnet with its dipole moment pointing in the positive and negative z-direction, respectively. Forcing frequency f_x=100 mHz. Phase-shift $\phi_x = 0$.

Figure 4.5: Flow due to a disordered array of five magnets at phase $\varphi = 8/10\ \pi$. a) Experimental visualization. b) Numerical Lagrangian particles tracking. The squares denote the footprint of the magnet. The black dot (•) and the cross (×) denote a magnet with its dipole moment pointing in the positive and negative z-direction, respectively. Forcing frequency f_x=50 mHz. Phase-shift $\phi_x = 0$.

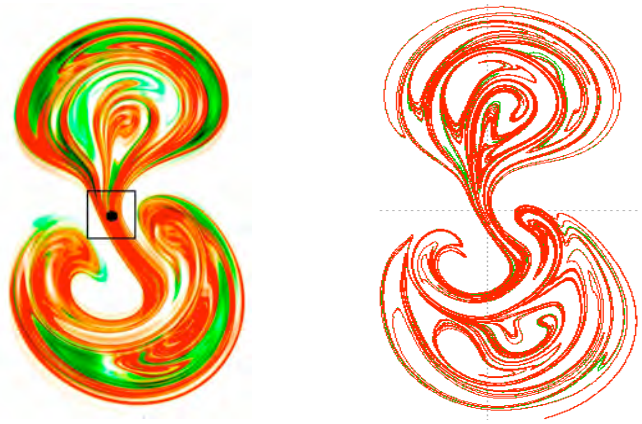

Figure 4.6: Oscillating vortex flow in a dipolar magnetic field created by the injection of two orthogonal currents (phase $\varphi = 18/10\ \pi$). a) Experimental visualization. b) Numerical Lagrangian particle tracking. The square denotes the footprint of the magnet. The black dot (•) denote a magnet with its dipole moment pointing in the positive and negative z-direction, respectively. Forcing frequencies $f_x = 50$ mHz and $f_y = 200$ mHz. Phase-shifts $\phi_x = \phi_y = 0$.

In the simplest case, namely, the oscillating vortex flow in a dipolar magnetic field with a single current (see figure 4.2), the Lorentz force generates a flow pattern with a symmetry line along the y-axis. When an additional orthogonal current is injected, a Lorentz force in the x-direction that breaks the symmetry line appears and then, mass transport occurs between the left and right sides of the flow. Figure 4.6 shows both the experimental visualization and the numerical Lagrangian tracking of the flow created by two orthogonal currents under the field of a single magnet. Phase-shifts (ϕ) of both currents are zero and their frequencies are $f_x = 50$ mHz and $f_y = 200$ mHz. Note that mixing is clearly improved with respect to the case of a single current.

Even if a single magnet is used, unexpected flow patterns can arise from the combination of the electrical parameters, namely the amplitude, the frequency and the phase-shift for each current. Figure 4.7 shows the vortex flow created when the frequencies of both currents are equal to 50 mHz but with a phase-shift of $\pi/2$, that is, $\phi_x = 0$ and $\phi_y = \pi/2$. In other words, sine and cosine current signals are used. These injected currents interacting with the dipolar magnetic field create an effective counter-clockwise rotating Lorentz force that produces an oscillating vortex monopole. Evidently, the Lorentz force distribution breaks

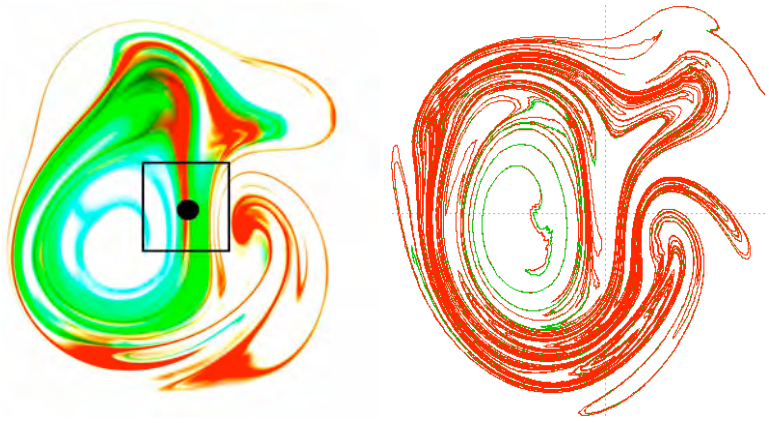

Figure 4.7: Oscillating monopolar vortex flow in a dipolar magnetic field created by the injection of two orthogonal currents (phase $\varphi = 18/10\ \pi$). a) Experimental visualization. b) Numerical Lagrangian particles tracking. The square denotes the footprint of the magnet. The black dot (•) denotes a magnet with its dipole moment pointing in the positive z-direction. Forcing frequencies $f_x = f_y = 50$ mHz. Phase-shifts $\phi_x = 0$, $\phi_y = \pi/2$.

the spatial symmetries and enhance the fluid mixing.

In general, visualization based on numerical Lagrangian particle tracking agrees qualitatively with the experiments. Nevertheless, this visualization method presents the problem of superposition of the coulored lines when symmetry breaking occurs (figures 4.5, 4.6 and 4.7), and does not allow to fully discern the color distribution as the experimental visualization does. On the other hand, Lagrangian tracking only considers convection effects and disregards diffusion effects. In the following subsection, the transport of a scalar by convection-diffusion effects is addressed with the DSM.

4.4.2 Convection-diffusion of a scalar: DSM results

In this subsection, the numerical results of the scalar transport in electromagnetically driven vortex flows calculated with the Diffusive Strip Method are compared with experiments. Only flows generated in multipolar magnetic fields with a single alternate electric current and a fixed frequency, are considered. In principle, the maximum velocity that can be reached in the experiments is $U = 1.4 \times 10^{-2}$ m-s^{-1} , that corresponds to an injected steady direct current of 80 mA (see

figure 1.8). With this velocity scale, the maximum Reynolds number based on the magnet side length is equal to $Re = UL/\nu = 350$. In turn, the oscillation Reynolds number based on the experimental forcing frequency (f=50 mHz) corresponds to $R_\omega = \omega L^2/\nu = 200$, while the Péclet number is equal to $Pe = UL/D = 7 \times 10^5$. In Chapter 3, the Q2D numerical model was validated with velocity fields of multipolar flows with an electrical current amplitude of 80 mA, while in the experiments described here, the maximum current amplitude reached was 60 mA. The smaller amplitude is attributed to the influence of the fluoresceine used in the experiments. It appears that it modifies slighly the physical properties of the electrolite, in particular, the effective electrical conductivity seems to be reduced. It is important to mention that the DSM has been validated with the Lamb-Oseen vortex flow, for which a theoretical prediction exists (Meunier $\&$ Villermaux 2003). Figure 4.8 shows the experimental visualization and numerical simulation of the oscillatory flow in the field of a single magnet. The initial condition ($t = 0$ s) is established by situating a blob of dye at ($x \approx$0,$y \approx$0). At this time, concentation of the blob is uniform, as can be observed in the first column of figure 4.8. As time increases, the tracer is deformed as the oscillating dipolar vortices evolve. At $t = 25$ s, dye concentration is no longer uniform, it is weaker in the magnet region where the Lorentz force stretches the scalar more intensively. In turn, in the outer region where fluid is almost at rest, the concentration is close to the initial one. We can observe that every half-cycle, the scalar is pushed away from the magnet zone forming a kind of semicircles around the central zone (second column in figure 4.8). At $t = 60$ and $t = 75$ s, diffusion effects are clearly observed and the thickness of the lines formed by the dye is not constant (third and fourth columns in figure 4.8). For longer times, due to the continuous electromagnetic stirring, the dye concentration decreases everywhere, indicating the mixing of the fluoresceine with the electrolite. Numerically, the scalar is located initially forming a circle with radius r=5 mm and width s_0=4 mm around the origin. It can be seen that the numerical simulation reproduces quite well the experimental observations (note the scale of gray at the right-hand side of the figure where the normalized concentration of the scalar is shown).

As expected, the scalar transport gets more complicated for flows in multipolar magnetic fields. In fact, stretching and folding produced by a more complex time-dependent flow field along with diffusion effects, promote mixing enhancement. Figure 4.9 shows the experimental visualization and numerical simulation of the scalar transport at a fixed time ($t = 20$ s) in oscillating flows produced by a time-periodic Lorentz force in ordered arrays of two and four magnets and a disordered array of five magnets. At this time, that corresponds to one period,

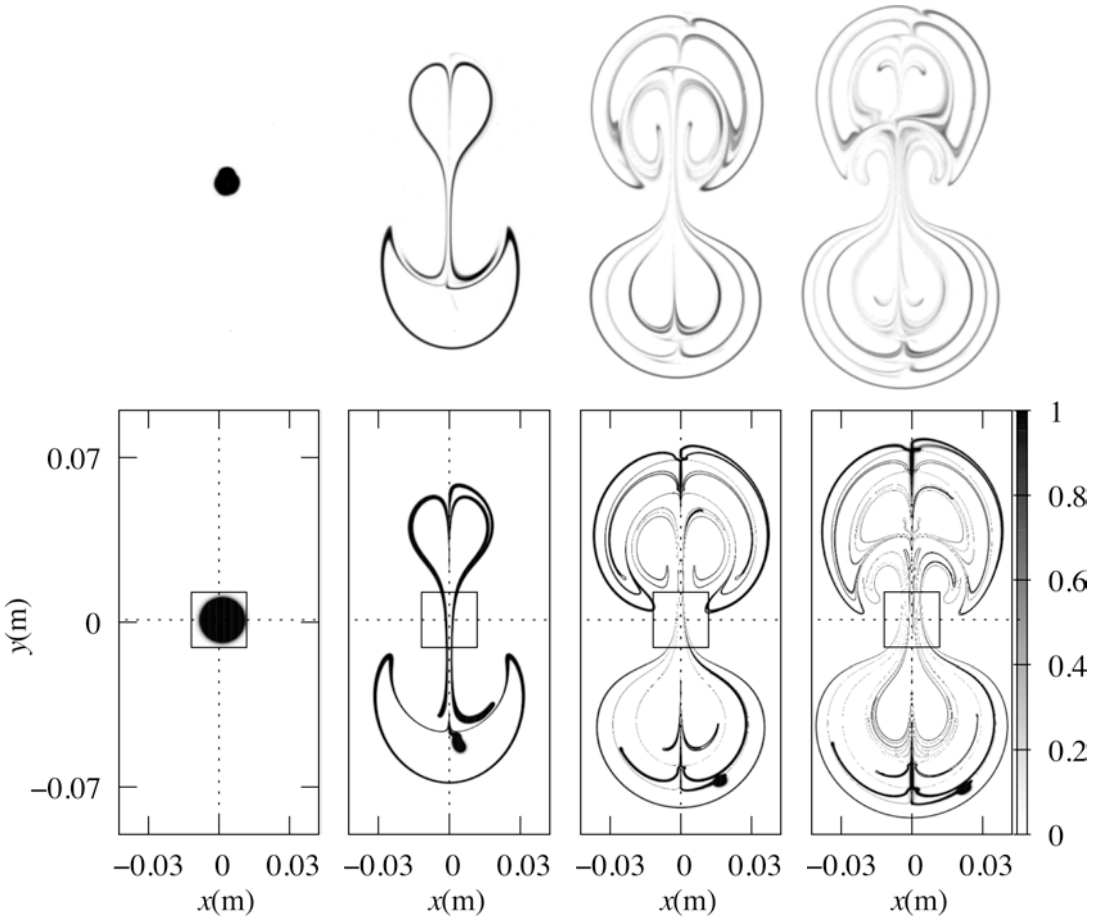

Figure 4.8: Oscillating dipolar vortex flow. First row, experimental visualization, second row, numerical simulation. First column, t=0 s, second column, t=25 s, third column, t= 60 s, fourth column, t= 75 s. The square denotes the footprint of the magnet polarized in the positive z direction. Forcing frequency $f_x = 50$ mHz. Phase-shift $\phi_x = 0$.

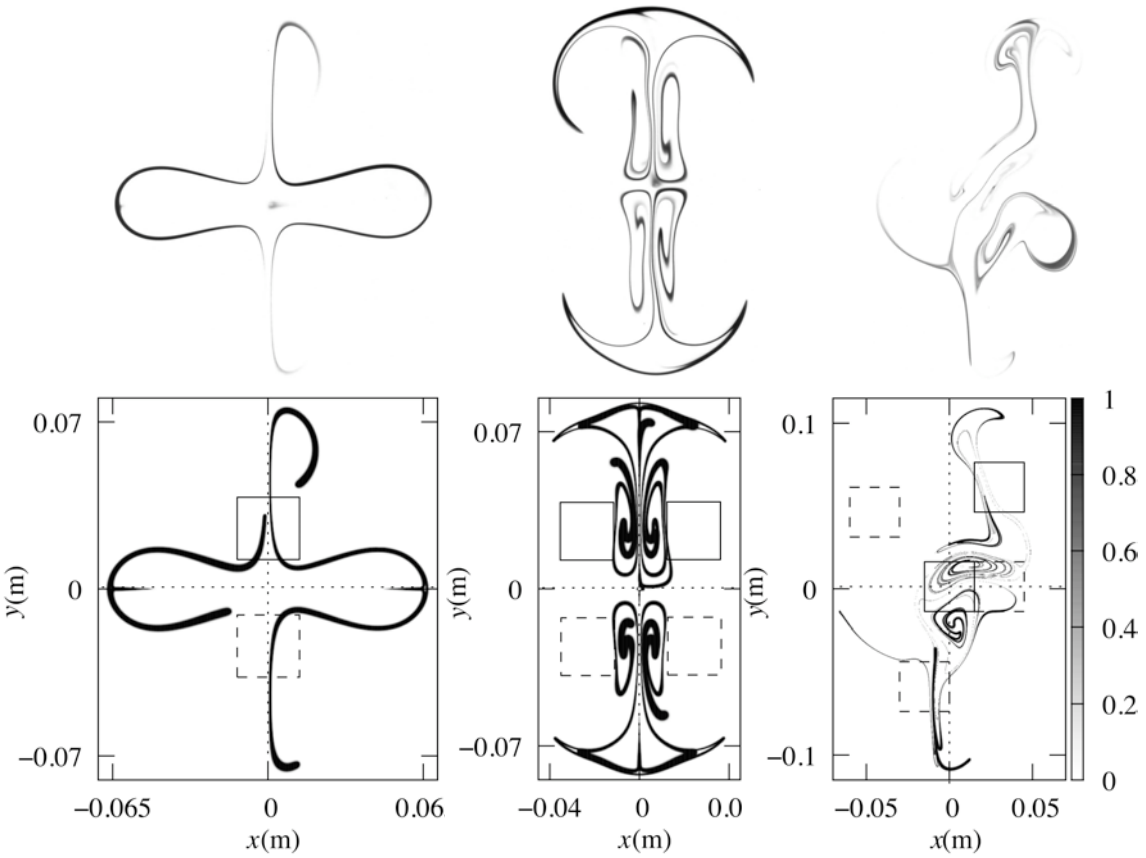

Figure 4.9: Oscillating vortex flows at t=20 s in multipolar magnetic fields. First row, experimental visualization, second row, numerical simulation. First column, vortex flow in a quadrupolar magnetic field. Second column, vortex flow in an octopolar magnetic field. Third column, vortex flow in a disordered array of five magnets. Continuous and dashed squares denote the footprint of magnets polarized in the positive and negative z direction, respectively. Forcing frequency $f_x = 50$ mHz. Phase-shift $\phi_x = 0$.

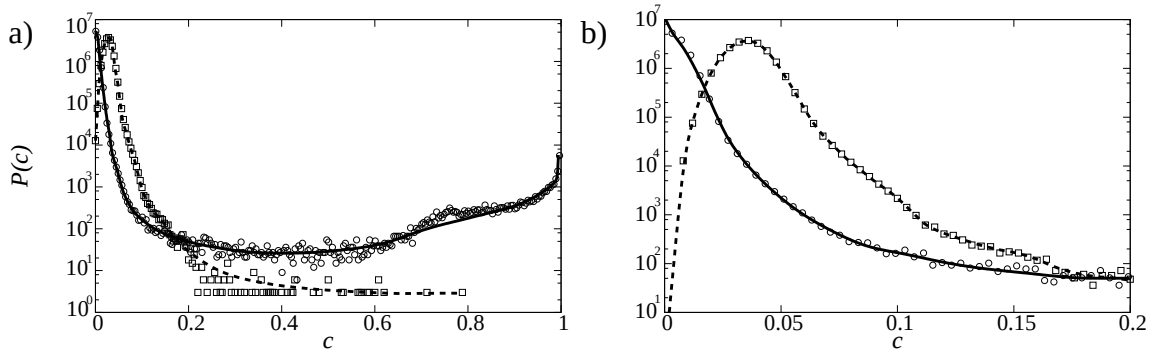

Figure 4.10: PDF of the experimental scalar distribution due to the oscillating vortex dipole. a) t=0 s (circles and continuous line), t =300 s (15 cycles) (squares and dashed line). b) Zoom of the figure. The lines are spline fits to guide the eye.

the dye concentration in the elongated strips for the flows in the quadrupole and octopole magnetic fields, is still close to the initial concentration. In contrast, in the flow with the disordered array of magnets, dye concentration has considerably diminished which indicates that the mixing rate has been increased.

In order to quantify the mixing efficiency, we make use of a spatial and temporal criterium, namely, the histogram or probability density function (PDF) $P(c)$ of the concentration levels c. $P(c)dc$ is defined as the normalized number of pixels whose concentration is in the interval $[c, c + dc]$. Figure 4.10 shows the PDF for experimental visualizations of the oscillating vortex dipole at two time instants. At the initial state ($t = 0$ s), the histogram shows the well known U-shape. It comes from the larger number of pixels of the background (c=0) and the maximal initial concentration (c=1). After 15 cycles (t=300 s), a large amount of low concentration pixels surrounds the small maximum at $c \approx$0.04, and the PDF shows a thin gaussian profile which is an indicative that the scalar concentration is uniform. Since the dye is pushed away from the magnet zone to the outer region where fluid is almost at rest, some pixels in this region still have high concentration levels up to c=0.8

Figure 4.11 shows the PDF of the experimental visualizations for the flows in a dipolar magnetic field and a disordered array of magnets at two time instants. At t=20 s (figure 4.11(a)), the scalar in the dipolar vortex flow has not reached the mixing time so that the maximal concentration is almost everywhere equal to the initial concentration. In turn, for the flow in the disordered array of magnets

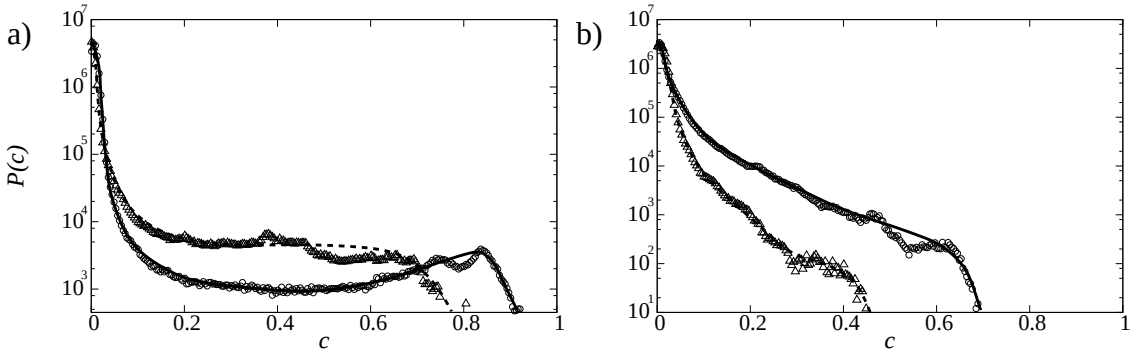

Figure 4.11: PDF of the experimental scalar distribution due to the oscillating vortex flow in a dipolar field and a disorder array of five magnets. a) t=20 s (1 cycles) . b) t =160 s (8 cycles). PDF due to dipolar flow is denoted by circles and continuos line. PDF due to disordered flow is denoted by triangles and dashed line. The lines are spline fits to guide the eye.

the scalar has started to mix, filling the low levels of concentrations in the PDF. With the disordered array, the PDF becomes a decreasing function of c, with an inverted S-shape characteristic of flows with a broad distribution of stretchings (Duplat *et al.* 2009). After 8 cycles (t=160 s), the scalar concentration in the disordered array is more uniform and the average concentration is smaller. PDFs corresponding to flows in quadrupole and octupole magnetic fields are omitted since their curves are located between the dipolar and disordered vortex flow. Nevertheless, at early stages flow in a quadrupole field mixes better than the octopole case. Indeed, the disordered flow is the best mixer since it achieves a uniform scalar concentration in a shorter time than flows in dipolar, quadrupolar and octopolar fields. However, we must note that at late stages (t >160 s), quadrupole show similar mixing results as the disordered flow.

Figure 4.12 shows the PDF of concentration for strips advected by the oscillating dipole and disordered vortex flows at the initial time ($t = 0$) and after one period ($t = 20$). The DSM allows to predict the shape of the PDFs at the different time stages, a U-shaped PDF between $c = 0$ and $c = 1$ as a initial condition and a S-shape PDF as a decreasing function of c at intermediate times. However, numerics refinement must be acomplished in order to reach a quantitative agreement.

Along with the numerical dispersion of the scalar, the DSM method allows to compute the total length of the strip S_L as it is convected by the flows. Figure

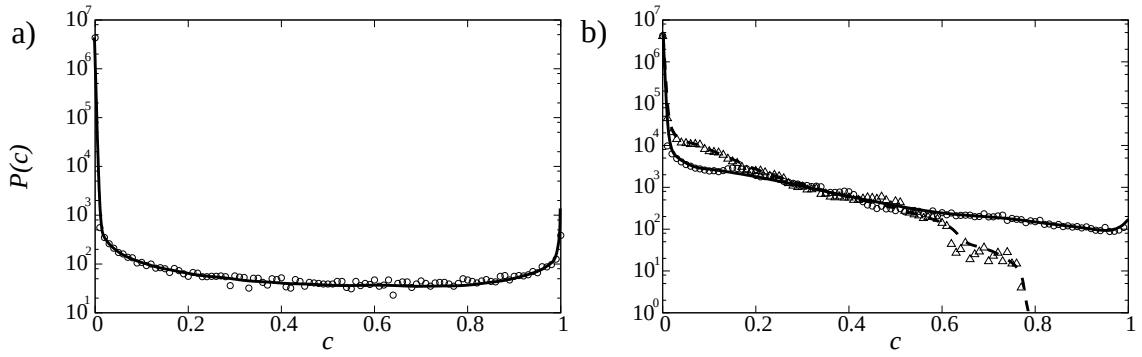

Figure 4.12: PDF of the numerical scalar distribution due to the oscillating flows in a dipolar magnetic field and disorder array of five magnets. a) t=0 s. b) t =20 s (1 cycles). PDF due to dipolar flow is denoted by circles and continuos line. PDF due to disordered flow is denoted by triangles and dashed line. The lines are spline fits to guide the eye.

4.13 shows the lenght of the strip as a function of time for different flows. As flow evolves, the strip is stretched and folded so that its length tends to grow exponentially from 3 cm to 20 m in approximately 8 cycles (t=160 s) for the dipolar flow, and in only 1 cycle (t=20 s) for the disordered flow. The exponential growth in time of S_L by stretching and folding is an indicative of chaotic mixing in the flows (Ottino 1989).

4.5 Discussion

In this Chapter, we have analyzed experimentally and theoretically the mixing in laminar time-periodic vortex flows in a shallow electrolytic layer. The flow patterns were generated by the interaction of multipolar magnetic field distributions produced by arrays of magnets and a uniform alternate current. First, using the flow fields calculated numerically through the Q2D model, the Lagrangian particle tracking of different flows was compared with experimental visualization using dye. It was found that the mixing produced by electromagnetically driven flows is strongly influenced by the magnetic field distributions used. With a single magnet or ordered arrays of two and four magnets, clear symmetry lines appear in the flow patterns. The displayed flow symmetries, acting as mixing inhibitors, are originated by symmetric Lorentz forces that, in turn, appear as a consequence of inherent symmetries in the magnetic field distribution. In fact, the magnetic

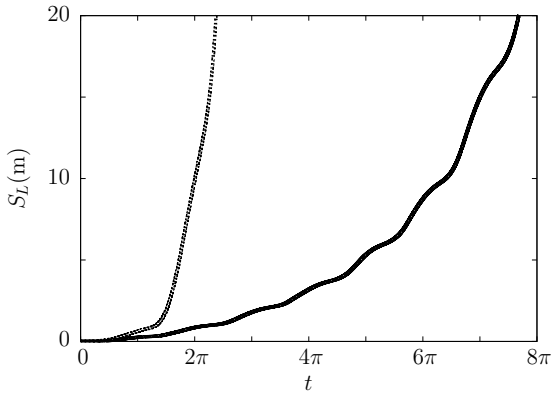

Figure 4.13: Numerically calculated total strip length S_L as a function of time t. Continuous line, dipole flow; dotted line, disordered vortex flow.

field generated by a permanent dipole magnet has a symmetric 3D Gaussian-like distribution. When ordered arrays of magnets are used, the total magnetic field distribution is symmetric too. If a one directional current is present, only a non-symmetric magnetic distribution (as the one given by a disordered array of magnets) is able to break the flow symmetries. On the other hand, in an ordered array of magnets, the driving force generated by one electrical current is not able to break these symmetries. However, an additional current in an orthogonal direction breaks the symmetry and enhances the fluid mixing. In general, a good qualitative agreement between the numerical Lagrangian particle tracking results and the visualization experiments was found. Although this numerical procedure does not consider diffusion effects, it clearly shows the convective mixing mechanism based on stretching and folding. It is important to notice that the Q2D model that introduces a linear friction with the bottom wall leads to satisfactory results not only with a single electrical current is present but also when two orthogonal currents are considered.

On the other hand, the convection-diffusion transport of a scalar was addressed by implementing the Diffusive Strip Method (Meunier $\&$ Villermaux 2010). In this new model, the position of an advected material strip is computed kinematically, and the associated convection-diffusion problem is solved by using the computed local stretching rate along the strip, assuming that the diffusing strip thickness is smaller than its local radius of curvature. This widely legitimate assumption reduces the numerical problem to the computation of a

single variable along the strip, thus making the method extremely fast and applicable to high Péclet numbers. This numerical method makes the link between the standard fluid dynamics simulation methods which are limited to small Péclet numbers and the Lagrangian tracking methods which do not model the diffusion of a scalar. The DSM model correctly captures the main physical features of the scalar mixing in electromagnetically driven flows in multipolar magnetic fields. In general, a good qualitative comparison is found between numerical results and experimental observations. Also, the model predicts correctly the U-shape of the PDFs for the initial condition and the inverted S-shape at intermediate times. Further, as the strip is stretched and folded, the method allows to calculate the total length of the strip which was found to grow exponentially, indicating that chaotic mixing is inherent in this kind of flows.

Concluding remarks

In this thesis, the experimental study of laminar vortex flows continuously driven by electromagnetic forces in shallow (4 mm) electrolytic layers, has been complemented with numerical simulations with the aim at contributing to the understanding of the dynamic and mixing properties of these flows. In contrast with high-Hartmann number electrolytic (Andreev *et al.* 2001) or liquid metal (Messadek & Moreau 2002) flows, the very small values of Ha in the present experiments ($\mathcal{O}(10^{-1})$) lead to negligible induced effects and to the predominance of viscous and imposed non-uniform Lorentz forces. Although several experimental studies have addressed the decay properties of vortical shallow flows of electrolytes initially generated by electromagnetic forcing, the detailed exploration and modelling of flows in shallow layers continuously stirred by localized electromagnetic forces have been poorly explored previously.

Several configurations of localized Lorentz forces generated by injected (steady or alternate) electric currents interacting with magnetic fields produced by arrays of permanent magnets, were studied through PIV measurements, dyed water visualization, and Lagrangian particle tracking. Steady and time-dependent flows were explored in flow planes parallel to the bottom wall at different depths as well as in flow planes normal to this wall, so that an approximate three-dimensional picture of the flow structure was reconstructed. In particular, by looking at these planes close to the bottom wall, the damping of velocity due to bottom friction was measured acurately. It appears that the experimental measurement of velocity profiles in the vertical direction in electromagnetically driven shallow flows have been overlooked in the past. In spite of the weakness of the applied magnetic field distributions, this information reveals velocity profiles with a shape that depends on the location within the non-uniform magnetic field region and, consequently, on the varying forcing intensity. Our results show a clear effect of the magnetic field inhomogeneity in the vertical direction. In fact, the decay of the field influences the form of the vertical velocity profiles since the driving

force diminishes with the increase in the vertical distance from the magnet, as it is clearly shown in the flattened Poiseuille-like and Stokes-like profiles measured for steady and oscillatory forcing, respectively. In turn, the inhomogeneity of the field in horizontal planes is more pronounced around the edge of the magnet and creates a vertical force that promotes a slight three-dimensionality in the flows. However, under the explored conditions of layer thickness, current amplitude, and magnetic field strength, no recirculations were observed in planes normal to the bottom wall, indicating that the transport of momentum in the normal direction is mainly diffusive. Three-dimensional numerical results reveal that vertical velocities do exist in the flow but are too small to be detected experimentally. Although experimental results corroborate the presumption of quasi-two-dimensionality of these flows, a word of caution should be mentioned since variation of the experimental conditions, particularly on the layer thickness and current amplitude that are more easily varied, may lead to important 3D effects.

Numerical modeling included development of Q2D and 3D models from which numerical simulations were carried out and compared quantitatively with available experimental results. It is interesting to mention that the simple Q2D model correctly captures the main physical features of the basic flows in both steady and time-periodic forcing cases and avoids difficulties of a full 3D approach. Moreover, good quantitative comparisons were found not only with flows generated under the magnetic field of a single magnet but also under multipolar magnetic fields. The Q2D model includes convective effects and involves the integration (averaging) of governing equations in the vertical direction, including a linear term that accounts for the friction with the bottom wall. Since the depth of the electrolyte layer is much smaller than its horizontal extension, the local magnetic field originated by a permanent dipole magnet can be realistically approximated by considering only its component in the vertical direction. The vertical field component was modeled analytically and fitted accurately to reproduce the experimental field, so that the decay of the field in the vertical direction was considered. The results reported in the present study show that a Q2D description of electromagnetically forced laminar steady and time-dependent flows at low-Hartmann numbers in shallow layers of electrolytes, is suitable. Although some previous Q2D models have been reported for steady flows, to the best of our knowledge, a Q2D model for continuously driven oscillating flows has not been presented before.

The analysis of the mixing properties of laminar flows produced by time-periodic electromagnetic forces under magnetic field distributions created by one

or several magnets, revealed interesting behaviors that may deserve further studies for chaotic mixing applications. Although some previous works have addressed experimentally the mixing of electroyltes with time-periodic forces (Voth *et al.* 2003), to our knowledge no previous theoretical modeling of such flows has been reported. Numerical tools developed for the convective Lagrangian particle tracking in electromagnetically driven flows clearly showed the stretching and folding mechanism and allowed a good comparison with visualization experiments, which demonstrated that mixing is inhibited when symmetric magnetic field distributions and a single injected current are used. It was found that mixing is enhanced by using a disordered (non-symmetric) magnetic field distribution or by injecting an additional orthogonal current. Finally, the Diffusive Strip Method (Meunier & Villermaux 2010) implemented to analyze the convection-diffusion transport of a scalar, correctly captures the main physical features of the scalar mixing in electromagnetically driven flows in multipolar magnetic fields and set the basis for deeper studies and developing of specific applications.

Bibliography

- Akkermans, R. A. D., Kamp, L. P., Clercx, H. J. H. & van Heijst, G. J. F. 2008 Intrinsic three-dimensionalitly in electromagnetically driven shallow flow. *Europhys. Lett.*, **83**, 24001.

- Akkermans, R. A. D., Cieslik, A. R., Kamp, L. P., Trieling, R. R., Clercx, H. J. H. & van Heijst, G. J. F. 2008 The three-dimensional structure of an electromagnetically generated dipolar vortex in a shallow fluid layer. *Phys. Fluids*, **20**, 116601.

- Alboussière, T. 2004 A geostrophic-like model for large hartmann number flows *J. Fluid Mech.*, **521**, 125–154.

- Andreev, O., Heberstroh, Ch. & Thess, A. 2001 MHD flow in electrolytes at high Hartmann numbers. *Magnetohydrodynamics*, **37**(1-2), 151–160.

- Aref, H. 1984 Stirring by chaotic advection. *J. Fluid Mech.*, **143**, 1–21.

- Aref, H. & Balachandar, S. 1986 Chaotic advection in a Stokes flow. *Phys. Fluids.*, **29**, 3515–3521.

- Barba L. A. & Velasco O. U. 2008 Lagrangian Flow Geometry of Tripolar Vortex. *IUTAM Bookseries*, **6**, 247-256.

- Brown, C. A., Jackson, G. A. & Brooks D. A. 2000 Particle transport through a narrow tidal inlet due to tidal forcing and implications for larval transport. *J. Geophys. Res.,*, **105**, 24, 141–24,156.

- Cardoso, O., Marteau, D. & Tabeling, P. 1994 Quantitative experimental study of the free dacay of quasi-two-dimensional turbulence. *Phys. Rev. E*, **49**(1), 454–461.

- Chien, W. L., Rising, H. & Ottino, J. M. 1986 Laminar mixing and chaotic mixing in several cavity flows. *J. Fluid Mech.*, **170**, 355.

- Clercx, H. J. H. & van Heijst, G. J. F. 2002 Dissipation of kinetic energy in two-dimensional bounded flows *Phys. Rev. E*, **65**, 066305.

- Clercx, H. J. H., van Heijst, G. J. F. & Zoeteweij 2003 Quasi-two-dimensional turbulence in shllow fluid layers: The role of bottom friction and fluid layer depth *Phys. Rev. E*, **67**, 066303.

- Cuevas, S. & Ramos, E. 1997 Steady streaming in oscillatory viscous flow under a transverse magnetic field. *Phys. Fluids*, **9**, 1430–1432.

- Cuevas, S., Sierra, F. Z. & Avramenko, A. 2002 Magnetic damping of steady streaming vortices in an oscillatory viscous flow over a wavy wall. *Magnetohydrodynamics*, **38**, 35–358.

- Cuevas, S., Smolentsev, S. & Abdou, M. 2006 On the flow past a magnetic obstacle *J. Fluid Mech.* **553**, 227–252.

- Duplat, J., Innocenti, C. & Villermaux, E. 2009 A non-sequential turbulent mixing process. *Submitted*.

- Fereday, D. R., Haynes, P. H. & Vassilicos, J. C. 2002 Scalar variance decay in chaotic advection and Batchelor-regime turbulence. *Phys. Rev. E*, **65**, 035301.

- Ferrari, S. & Rossi, L. 2008 Particle tracking velocimetry and accelerometry (PTVA) measurements applied to quasi-two-dimensional multiscale flows. *Exp. Fluids*, **44**, 873.

- Figueroa, A., Cuevas, S. & Ramos, E. 2008 Mixing with a time-dependent MHD flow. *Proc. 7th Int. pamir Conf on Fundamental and Applied MHD*, Presqu'île de Giens, France, **1**, 421–426.

- Figueroa, A., Demiaux, F., Cuevas, S. & Ramos, E. 2009 Electrically driven vortices in a weak dipolar magnetic field in a shallow electrolytic layer. *J. Fluid Mech.*, **641**, 245–261.

- Figueroa, A., Cuevas, S. & Ramos, E. 2010 Stokes layer in electromagnetically driven oscillatory dipolar vortex. Submitted to *Phys. Fluids*.

- Fujiwara, T., Nakata, H. & Nakatsuji K. 1992 Tidal-jet and vortex-pair driving of the residual circulation in a tidal estuary. *Continental Shelf Research*, **14**, 1025–1038.

- Gleeson J. P. 2005 Transient micromixing: Examples of laminar and chaotic stirring. *Phys. Fluids*, **17**, 100614.

- Griebel, M., Dornseifer T. & Neunhoeffer T. 1998 *Numerical simulation in fluid dynamics.* SIAM.

- Hansen, Marteau, D. & Tabeling, P. 1998 Two-dimensional turbulence and dispersion in a freely decaying system. *Phys. Rev. E* **58**, 7261–7271.

- Hide, R. & Roberts, P. H. 1960 Hydromagnetic flow due to an oscillating plane. *Rev. Mod. Phys.*, **32** 758–769.

- Kunnen, R., Trieling, R. & van Heijst, G. J. 2010 Vortices in time-periodic shear flow. *Theor. Comput. Fluid Dyn.*, **24**, 315–322.

- Lavrent'ev, I. V., Molokov, S. Yu., Sidorenkov, S. I. & Shishko, A. R. 1990 Stokes flow in a rectangular magnetohydrodynamic channel with nonconducting walls within a nonuniform magnetic field at large Hartmann numbers. *Magnetohydrodynamics*, **26**(3), 328–338.

- Lardeau, S., Ferrari, S. & Rossi, L. 2008 Three-dimensional direct numerical simulation of electromagnetically driven multiscale shallow layer flows: Numerical modeling and physical properties. *Phys. Fluids*, **20**, (127101) 1–17.

- Leong, C. W. & Ottino, J. M. 1989 Experiments on mixing due to chaotic advection in a cavity. *J. Fluid Mech.*, **209**, 463499.

- Marteau, D., Cardoso, O. & Tabeling, P. 1995 Equilibrium states of two-dimensional turbulence: An experimental study *Phys. Rev. E* **51**, 5124–5127.

- McCaig, M. 1977 *Permanent magnets in theory and practice*. Wiley.

- Mc Williams, J. C. 2006 Fundamentals of geophysical fluid dynamics. Cambridge University Press.

- Messadek, K. & Moreau, R. 2002 An experimental investigation of MHD quasi-two-dimensional turbulent shear flows. *J. Fluid Mech.* **456**, 137–159.

- Meunier, P. & Villermaux, E. 2003 How vortices mix. *J. Fluid Mech.*, **476**, 213–222.

- Meunier, P. & Villermaux, E. 2010 The Diffusive Strip Method for scalar mixing in two-dimensions. *Submitted to J. Fluid Mech.*

- Moreau, R. 1990 *Magnetohydrodynamics*. Kluwer.

- Ottino J. M. 1989 The Kinematics of Mixing: Stretching, Chaos, and Transport. Cambridge University Press.

- Panton, R. L. 2005 Incompressible flow. *third edition Wiley, New Jersey*.

- Paret, J. & Tabeling, P. 1997 Experimental observation of the two-dimensional inverse energy cascade. *Phys. Rev. Lett.*, **79**(21), 4162–4165.

- Paret, J., Marteau, D., Paireau, O. & Tabeling, P. 1997 Are flows electromagnetically forced in stratified layers two-dimensional? *Phys. Fluids*, **7**(10), 3102–3104.

- Potherát, A., Sommeria, J. & Moreau, R. 2000 An effective two-dimensional model for MHD flows with transverse magnetic fields. *J. Fluid Mech.* **424**, 75–100.

- Rossi, L., Vassilicos, J. C. & Hardalupas, Y. 2006 Electromagnetically controlled multiple scale flows. *J. Fluid Mech.*, **558**, 207.

- Rothstein, D., Henry, E. & Gollub, J. P. 1999 Persistent patterns in transient chaotic fluid mixing. *Nature*, **401** (21 oct.) 770-772.

- Rossi, L., Vassilicos, J. C. & Hardalupas, Y. 2006a Electromagnetically controlled multi-scale flows *J. Fluid Mech.* **558**, 207–242.

- Rossi, L., Vassilicos, J. C. & Hardalupas, Y. 2006b Multiscale laminar flows with turbulentlike properties *Phys. Rev. Lett.* **97**, 144501.

- Satijn, M. P.,Cense, A. W., Verzicco, R., Clercx, H. J. H. & van Heijst, G. J. F. 2001 Three-dimensional structure and decay properties of vortices in shallow fluid layers. *Phys. Fluids*, **13**, 1932–1945.

- Smolentsev S. 1997 Averaged model in MHD duct flow calculations. *Magnetohydrodynamics*, **33**(1), 42–47.

- Solomon T., Winokur J., O'Malley G. and Paoletti M. 2008 Chaotic mixing and superdiffusion in a two-dimensional array of vortices. *Bulletin of the American Physical Society*, 61st Annual Meeting of the APS Division of Fluid Dynamics, **53**(15), 5:19PM LV.00009.

- Sommeria, J. and Moreau, R. 1982 Why, how, and when, MHD turbulence becomes two-dimensional. *J. Fluid Mech.* **118**, 507–518.

- Sommeria, J. 1986 Experimental study of the two-dimensional inverse energy cascade in a square box. *J. Fluid Mech.* **170**, 139–168.

- Sommeria, J. 1988a Electrically driven vortices in a strong magnetic field. *J. Fluid Mech.* **189**, 553–569.

- Sommeria, J. 1988b Experimental characterization of steady two-dimensional vortex couples. *J. Fluid Mech.* **192**, 175–192.

- Srineevasan, B., Davidson, P. A. & Etay, J. 2005 On the control of surface waves by a vertical magnetic field. *Phys. Fluids*, **17**, 117101.

- Stokes, G. G. 1851 On the effect of the internal friction of fluids on the motion of pendulums. *Trans. Cambridge Philos. Soc.*, **9**, Pt II, 8–106.

- Tabeling, P. 2002 Two-dimensional turbulence: A physicist approach. *Phys. Reports* **362**, 1–62.

- Voth, G. A., Haller, G. & Gollub, J. P. 2002 Experimental measurements of stretching fields in fluid mixing. 2002 *Phys. Re. Lett.*, **88**(15) 254501.

- Voth, G. A., Saint, T. C., Dobler, G. & Gollub, J. P. 2003 Mixing rates and symmetry breaking in two-dimensional chaotic flow. 1999 *Phys. Fluids*, **15** 2560–2566.

- Williams, B. S., Marteau, D. & Gollub, J. P. 1997 Mixing of a passive scalar in magnetically forced two-dimensional turbulence. 1997 *Phys. Fluids*, **9** 2061–2079.

- Wells, M. G. & van Heijst, G. J. 2003 A model of tidal flushing in an estuary by dipole formation. *Dyn. Atmos. Ocean*, **37**, 223–244.

- Wolanski, E., Drew, E., Abel, K. M. & O'Brien J. 1988 Tidal jets, Nutrient Upwelling and Their Influence on the Productivity of the Alga Halimeda in the Ribbon Reefs, Great Barrier Reef. *Estuarine, Coastal and Shelf Science*, **26**, 169–201.

- Zavala Sansón, L., van Heijst, G. J. F. & Backx, N. A. 2001 Ekman decay of a dipolar vortex in a rotating fluid. *Phys. Fluids*, **13**, 440–451.